Kinetics of Phase Transformations in Lithium-Sulfur Batteries

by

Frank Yongzhen Fan

B.S., Stanford University (2010)
M.S., Stanford University (2011)

Submitted to the Department of Materials Science and Engineering
in partial fulfillment of the requirements for the degree of

Doctor of Philosophy in Materials Science and Engineering

at the

MASSACHUSETTS INSTITUTE OF TECHNOLOGY

June 2017

Author . . . .
Department of Materials Science and Engineering
May 18, 2017

Certified by . . . .
Yet-Ming Chiang
Kyocera Professor of Ceramics
Thesis Supervisor

Accepted by . . . .
Donald R. Sadoway
Chairman, Department Committee on Graduate Theses

Kinetics of Phase Transformations in Lithium-Sulfur Batteries

by

Frank Yongzhen Fan

Submitted to the Department of Materials Science and Engineering
on May 18, 2017, in partial fulfillment of the
requirements for the degree of
Doctor of Philosophy in Materials Science and Engineering

Abstract

Sulfur is a promising positive electrode for lithium batteries with the potential to create the step-change improvement in energy density and cost needed for the widespread adoption of electric vehicles and renewable energy. However, lithium-sulfur batteries suffer from a number of challenges, among them poor rate capability resulting in part from a complex dissolution-precipitation mechanism which produces electronically insulating end members S_8 and Li_2S. Few studies have heretofore been performed on rate-limiting mechanisms in Li-S batteries, which must be elucidated in order to inform rational design of electrodes with high capacity and rate capability.

Polysulfide solutions, intermediates in the electrochemical reduction of sulfur, are used for the first time to make an efficient, high energy density flow battery, enabled by a novel flow battery architecture using a percolating network of nanoscale conductive carbon. An extensive experimental study of exchange current density for redox of higher order polysulfide solutions and their ionic conductivity has been conducted. The type and amount of electrolyte solvent has been found to influence both of these.

The second portion of this thesis characterizes the kinetics of Li_2S electrodeposition, which is responsible for three-quarters of the theoretical capacity of the sulfur cathode. Kinetics are found to be highly dependent on solvent choice in a manner similar to exchange current density. Furthermore, electrodeposition kinetics are found to slow considerably at the low electrolyte/sulfur ratios which are needed for high energy density and low cost. Materials such as conductive oxides can serve as nucleation promoters and help solve this challenge. The morphology of precipitates is found to be dependent on discharge rate, with large, discrete particles forming at low rates. A model was for describing 3-D electrodeposition of Li_2S under the influence of a soluble redox mediator which enables efficient utilization of conductive surface area and prevents passivation of conductive carbon with insulating Li_2S.

Thesis Supervisor: Yet-Ming Chiang
Title: Kyocera Professor of Ceramics

Acknowledgments

I would like to thank my advisor, Professor Yet-Ming Chiang, for all of the guidance he has given me over the last five years. I am grateful to him for holding me to high scientific standards, while at the same time allowing me considerable latitude in determining the direction of my research. Thanks to my committee members, Professors Carl Thompson and Niels Holten-Andersen, for the helpful feedback and discussions on my thesis.

I would like to thank the other past and current members of the Chiang group for creating a fun and collegial research environment and for all of the things I've learned from them during this process: Ariel Jackson, Benjamin Delattre, Billy Woodford, Bohua Wen, Daniel Rettenwander, David Young, Dorthe Bomholdt Ravnsbæk, Giovanna Bucci, Gülin Vardar, Jesse Benck, Jiayan Luo, Jonathan Sander, Kai Xiang, Kyle Smith, Liang Su, Linsen Li, Nir Baram, Ping-Chun Tsai, Richard Park, Ruhul Amin, Sam Pan, Tushar Swamy, Wenting Xing, Xinwei Chen, Younes Ansari, and Zheng Li. I am especially indebted to Zheng Li and Kyle Smith, who showed me the ropes when I first joined the group.

I would like to acknowledge financial support from the Joint Center for Energy Storage Research (JCESR) and from an Eni-MIT Energy Initiative fellowship.

Thanks to JCESR for connecting me to researchers across the country, many of whom I've had the pleasure of working with on interesting and innovative projects. These collaborators include Ahmed Helal and Prof. Gareth McKinley (MIT); Sean Wei and Prof. Jennifer Lewis (Harvard); Changyi Li, Laura Gerber, Longjun Li, Pete Frischmann, Sean Doris, and Brett Helms (Lawrence Berkeley National Laboratory); Kah Chun Lau, Rajeev Assary, and Larry Curtiss (Argonne National Laboratory); and Kevin Zavadil (Sandia National Laboratories)

Finally, I would like to thank my parents and grandparents for supporting me in my educational and professional endeavors for my entire life, and for instilling in me a love of math and science at an early age.

Contents

List of Figures

List of Tables

Chapter 1

Introduction

Low-cost batteries with high energy density are essential for the electrification of vehicles, which presently account for a significant fraction of global fossil fuel consumption. They are also necessary for the increased penetration of renewable energy sources such as wind and solar power, which suffer from intermittency and nondispatchability and must presently be backed up by other power sources that can be easily ramped, such as natural gas [1, 2]. Battery packs for electric vehicles currently cost in excess of \$300/kWh, while system-level costs of less than \$100-\$150/kWh are considered necessary for electric vehicles to be competitive with those using conventional fuels [3, 4, 5]. Also, light weight is important for vehicles and other portable applications, and a specific energy of 400Wh/kg is desired (compared to $<$150Wh/kg for state-of-the-art electric vehicle batteries today)[3].

Currently, lithium-ion batteries dominate the market for high-performance energy storage. Lithium batteries consist of a negative electrode (frequently referred to as an "anode"), positive electrode (frequently referred to as a "cathode"), and an organic liquid electrolyte, which must not react with the anode or cathode (schematic shown in Fig. 1-1)[1]. Both electrodes consist of composites of small particles of active material, conductive carbon additive, and binder which are coated onto metal foil (aluminum

---

[1] Strictly speaking, "cathode" refers to a species being reduced, and "anode" refers to the species being oxidized. When a battery is being charged, the positive electrode is being oxidized, and should by this convention be referred to the "anode." However, battery literature almost always refers to the positive electrode as the cathode, regardless of the electrochemical process it is undergoing.

for the positive electrode, copper for the negative). Electrodes are porous to allow electrolyte access to all of the active material. A porous polymer separator soaked with electrolyte is used to keep the positive and negative electrodes from touching while allowing ions to pass through. During the charge process, lithium ions are shuttled from the positive electrode to the negative one via the electrolyte, while electrons flow in the same direction through an external circuit.

Standard lithium-ion batteries have positive electrodes consisting of intercalation compounds, in which lithium ions are inserted into or removed from a host structure. These are transition metal compounds (oxides and polyanionic compounds) in which the transition metal ion acts as a redox center. Such compounds include layered oxides (e.g. $LiCoO_2$; $Li(Ni_xCo_yAl_{1-x-y})O_2$,"NCA"; $Li(Ni_xMn_yCo_{1-x-y})O_2$,"NMC"), spinels (e.g. $LiMn_2O_4$), and olivines (e.g. $LiFePO_4$). These materials either maintain their structure throughout the charge or discharge process (in the case of the layered oxides) or undergo solid-state first-order phase transitions (in the case of the olivines and $LiMn_2O_4$). Negative electrode materials include graphite and silicon. Silicon has much higher specific capacity (2006 mAh/g $Li_{22}Si_5$) than graphite(339 mAh/g LiC_6), but poses significant challenges due to its volume expansion during lithiation[6]. Lithium metal has a greater specific capacity (3860 mAh/g) than both of these, but is not currently viable because it reacts with the electrolyte and because repeated plating and stripping thereof results in the growth of "dendrites" which can short-circuit the cell and cause fires[7]. In general, "lithium-ion" refers to batteries containing intercalation electrode materials and excludes other types of lithium-containing batteries.

A number of so-called "beyond lithium-ion" battery chemistries have been proposed which have the potential to offer step changes in energy density and cost. These include sodium-ion[8, 9], magnesium[10], lithium-oxygen, and lithium-sulfur. Sodium-ion and magnesium batteries are similar to lithium-ion ones and operate via an intercalation mechanism but have the potential to be lower cost. Magnesium in particular is of interest due to the fact that the working ion has double the charge of a lithium or sodium ion, and because of the relative ease of using magnesium metal

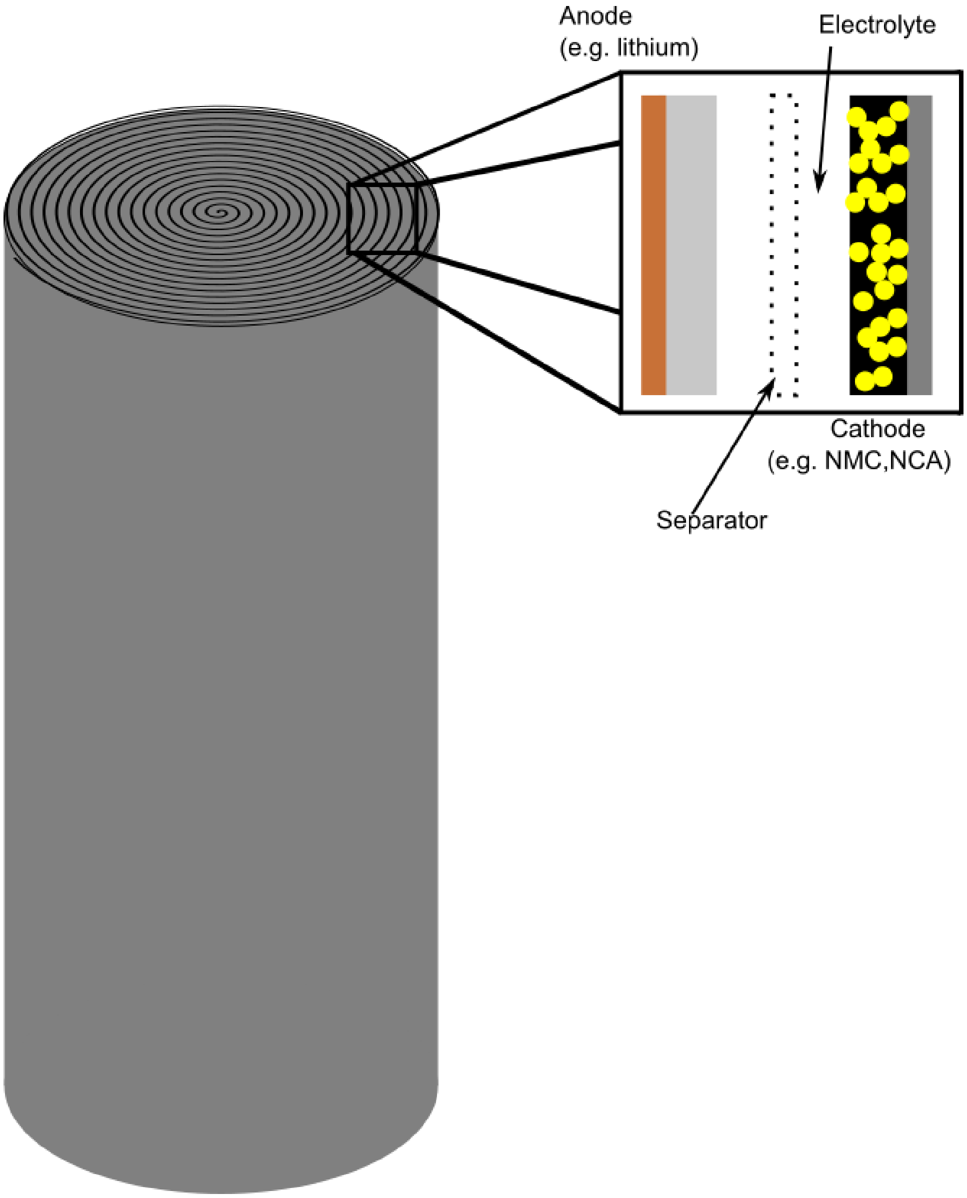

Figure 1-1: Schematic of a cylindrical battery cell

as a negative electrode. Lithium-oxygen and lithium-sulfur batteries are different and undergo precipitation-dissolution reactions at the cathode, rather than intercalation reactions. Lithium-sulfur, in particular, is considered the "beyond lithium-ion" chemistry closest to commercial viability.

1.1 Overview of lithium-sulfur batteries

Sulfur is of interest as a positive electrode for lithium batteries because of its low cost and high theoretical specific capacity of 1675 mAh/g. This is approximately an order of magnitude higher than that of standard intercalation compounds used in Li-ion batteries and is due to the fact that each relatively light sulfur atom can undergo a 2-electron transfer, compared to less than one electron for a transition metal ion in an intercalation cathode (Fig. 1-2) [11, 12, 13]. Although the voltage of a Li-S cell is lower than that of a Li-ion one (2.2V vs 3.8V), the much higher capacity of sulfur enables higher energy density. Furthermore, sulfur is a very inexpensive material that is produced in large quantities as a by-product of the oil and gas industry. Prices fluctuate but are typically less than \$0.10/kg, compared to \$25/kg and \$9/kg for cobalt and nickel which are used in state-of-the-art Li-ion batteries[14].

Li-S batteries consist of a lithium metal negative electrode, sulfur-carbon composite positive electrode, and an ether-based electrolyte. Graphite and silicon have been successfully used as negative electrode materials [15], but lithium metal is almost always used because of its much higher capacity. Carbon (typically carbon black) must be added to the positive electrode because of the very low electronic conductivity of both sulfur and lithium sulfide, although other conductive materials such as metal oxides have been considered [16, 17, 18, 19]. A typical electrolyte for Li-S batteries is a 1:1 (by volume) mixture of 1,3 dimethoxyethane (DME) and 1,2 dioxolane (DOL), with bis(trifluoromethane) sulfonimide lithium (LiTFSI, $CF_3SO_2NLiSO_2CF_3$) as an electrolyte salt. Other ethers, in particular other members of the glyme family (e.g. diglyme, triglyme, tetraglyme), have also been used as electrolyte solvents. Alkyl carbonates used in lithium-ion battery electrolytes are not used in lithium-sulfur bat-

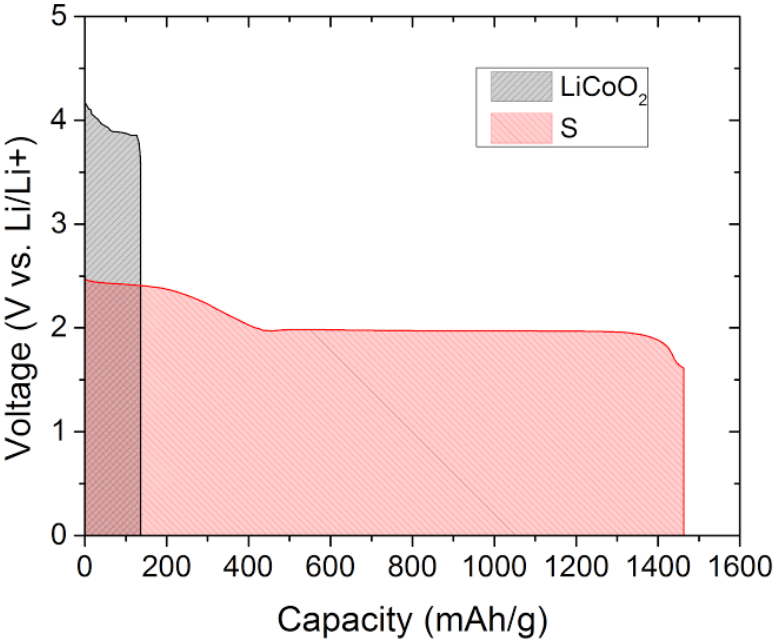

Figure 1-2: Discharge curves for a typical lithium-sulfur cell and a lithium-$LiCoO_2$ cell. Sulfur has a lower cell potential but a significantly higher gravimetric capacity. The integral of the discharge curve is the amount of electrical energy delivered by the cell.

teries due to nucleophilic attack by the sulfur species[20].

Li-S batteries have a solution-mediated charge/discharge mechanism that is fundamentally different from that of standard Li-ion batteries, as described in Equations 1.1-1.4. Solid elemental sulfur (S_8) is first reduced to lithium polysulfide (Li_2S_8), which is highly soluble in the electrolyte, to a concentration of approximately 8 mol S/l. This polysulfide is then reduced to lower order polysulfide species Li_2S_6 and Li_2S_4, which are also soluble, in the "solution regime." Finally, lower order polysulfides are reduced to insoluble lithium sulfide, Li_2S, which is electrodeposited onto the carbon network. The solution regime is a single-phase regime, while precipitation and dissolution of the insoluble end members are two-phase reactions. In a galvanostatic (constant current) discharge curve (Fig. 1-3), these appear respectively as a sloping region and two flat ones, since the Gibbs phase rule requires that two-phase regions with two components have constant chemical potential regardless of composition. Li_2S_2 has been proposed as a possible insoluble intermediate; however, *in situ* speciation analysis of Li-S batteries has suggested that Li_2S_2 is not present[21].

$$S_8 + 2Li^+ + 2e^- \rightarrow Li_2S_8 \tag{1.1}$$

$$3Li_2S_8 + 2Li^+ + 2e^- \rightarrow 4Li_2S_6 \tag{1.2}$$

$$2Li_2S_6 + 2Li^+ + 2e^- \rightarrow 3Li_2S_4 \tag{1.3}$$

$$Li_2S_4 + 6Li^+ + 6e^- \rightarrow 4Li_2S \tag{1.4}$$

Several technical barriers have limited the advancement of lithium-sulfur batteries. These include rapid capacity fade, low rate capability, the need for high volumes of electrolyte, formation of lithium metal dendrites, and low materials utilization. Most of these issues arise either from the unusual charge-discharge mechanism of Li-S batteries, which involves multiple phase changes, or the poor electronic conductivity of the insoluble species precipitated at both ends.

Because polysulfides are highly soluble in the electrolyte and are present throughout the charge and discharge processes, they easily diffuse from the positive to the

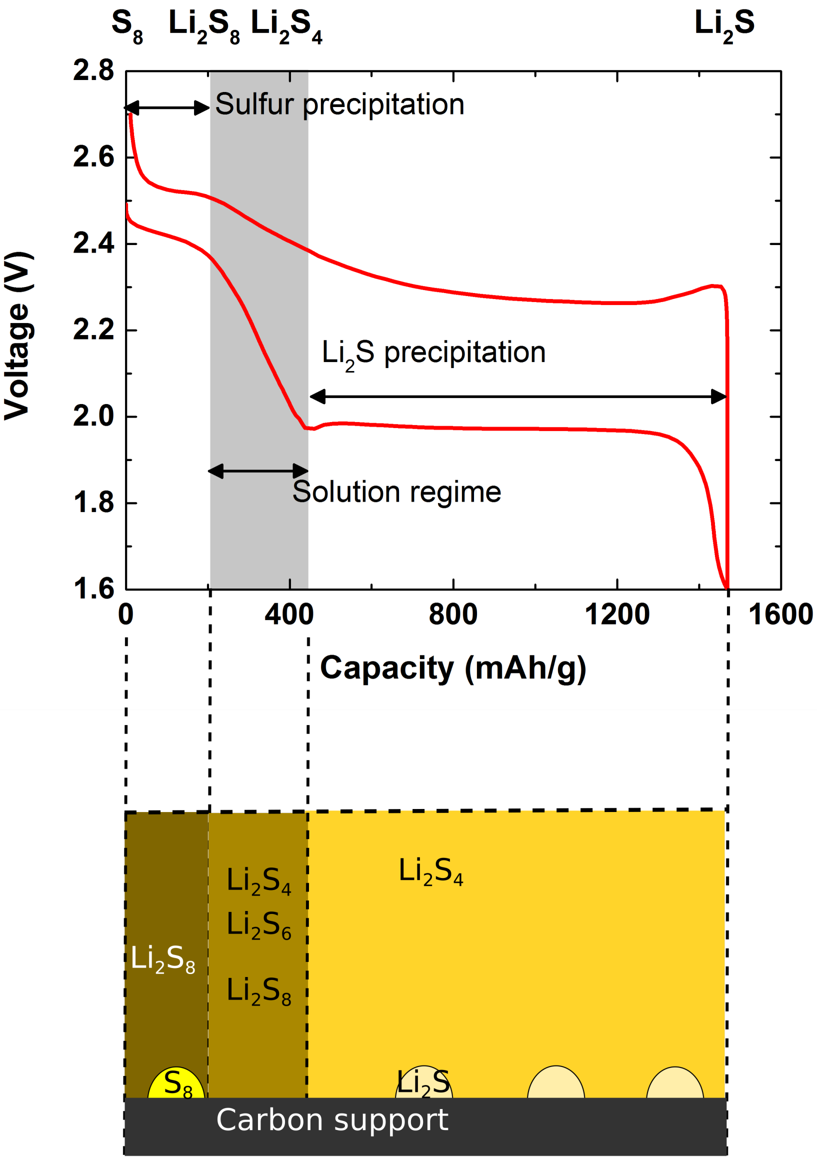

Figure 1-3: Discharge-charge curve for a typical lithium-sulfur battery (top), with schematic showing species and phases present during each step of the charge-discharge process. The central segment is a one-phase region which corresponds to a sloping equilibrium potential; the others involve phase transformations and have flat discharge curves.

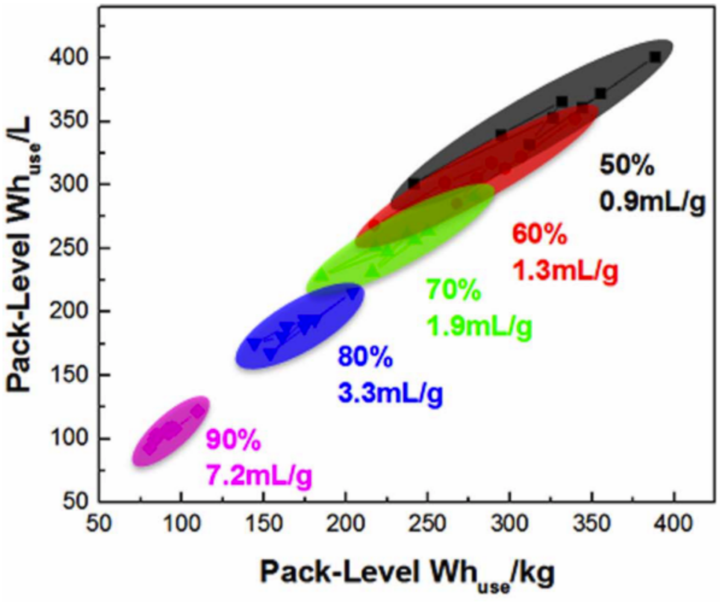

Figure 1-4: Calculated ranges of pack-level energy density and specific energy for lithium-sulfur batteries with different E/S ratios. From Ref. [3].

negative electrode and react chemically with the lithium metal. This "shuttle effect" creates an internal chemical short which reduces Coulombic efficiency and depletes the sulfur by stranding it at the negative electrode. Reduction of shuttling via immobilization of polysulfides has recently been a highly active area of research. Most approaches involve encapsulating the sulfur in various porous carbon materials that inhibit the diffusion of polysulfides[22, 23, 24, 25]. Replacement of the porous separator with an ion-selective membrane has also been somewhat successful at reducing shuttling[26, 27]. Lithium nitrate has been found to be a passivating agent for the lithium metal electrode that increase cycle life and coulombic efficiency and is almost universally used as an electrolyte additive. However, lithium nitrate is consumed during the cycling process and cannot provide permanent protection from shuttling[28].

In order to maximize the energy density and minimize the cost of a battery, the electrolyte/sulfur (E/S) ratio must be minimized. Few published studies on Li-S batteries include data on E/S ratio, but those that do usually have very high values (10 ml/g or higher)[29, 17, 30]. At these levels, the weight, volume, and cost of the excess electrolyte outweighs the cost and energy density benefits of sulfur. Therefore, reducing this ratio (as with limiting the amount of all inactive materials) is critical for commercializing the Li-S battery. An E/S ratio of around 1 ml/g is necessary to achieve 400Wh/l and 400 Wh/kg at the pack level (Fig. 1-4). However, low electrolyte-sulfur ratios have often been correlated with high polarization and poor cycle life.[3, 29].

A lithium metal negative electrode is required to achieve high energy density, but its high reactivity and poor morphological stability continue to be challenges. Lithium metal is highly reactive with polysulfides, and repeated plating and stripping of it causes dendrites to grow, which eventually leads to short-circuiting of the cell. The formation of dendrites also increases the surface area of the negative electrode, accelerating reactions between it and the electrolyte and consuming the latter. Carbon and silicon have been successfully used as negative electrodes in the past[15]. However, because of the lower cell potential of the Li-S couple compared to Li-ion batteries (about 2.2V vs. 3.8V), a greater capacity is needed for both the cathode and anode to store the same amount of energy, and lower capacity anodes such as carbon and silicon would not result in sufficient energy density. Hence, the protection of lithium metal and the suppression of dendrite formation is an important and active area of research. Approaches include electrolyte additives as well as the use of solid electrolytes which mechanically block dendrites[31, 32].

Lithium-sulfur batteries also have poor rate capability, which is the result of a combination of poor electronic conductivity and sluggish redox kinetics. However, despite several decades of research on Li-S batteries, no systematic study on rate-limiting mechanisms in such batteries has previously been performed. Moreover, despite extensive research on electrodeposition of insoluble species in lithium-oxygen batteries, similar studies have not been published for the lithium-sulfur system. This thesis aims to fill this gap in knowledge to enable the design of Li-S batteries with both high energy density and good rate capability.

1.2 Rate-Limiting Mechanisms in Li-S Batteries

In addition to energy density, the rate capability of a battery is an important parameter. The ability to charge or discharge a battery quickly is necessary, for example, to enable timely recharging of an electric vehicle or to deliver power quickly for acceleration. Capacity and energetic efficiency decrease with increased cycling rate, which is usually expressed as a "C-rate," which is the number of charges or discharges to theoretical capacity in one hour (for example, 2C would be one full charge in 1/2 hour; C/2 would be a full charge in 2 hours).

The equilibrium potential E of any electrochemical cell is related to the Gibbs free energy ΔG of the overall cell reaction by Equation 1.5, where F is Faraday's constant and z is the number of electrons transferred. However, during the actual charge or discharge of a battery, the actual potential will be higher or lower, respectively, than the equilibrium potential. This deviation is known as the overpotential and is required to drive the reaction in one direction or another. The gap between the galvanostatic (constant current) charge and discharge curves is the energy that is input and not recovered, and hence wasted. For a given cell, a higher C-rate requires a higher overpotential.

$$\Delta G = -zFE \tag{1.5}$$

Charge transfer kinetics of general electrochemical reactions are described by the Butler-Volmer equation (1.6), which is the difference between the forward and backward reaction rates, both of which are exponential terms with respect to the overpotential η. In this equation, α_a and $\alpha_c = 1 - \alpha_a$ are respectively the anodic and cathodic charge transfer coefficients, which are dimensionless numbers between 0 and 1. At the equilibrium potential, the forward and backward reaction rates are equal and their absolute value corresponds to the exchange current udensity j_0, which characterizes the speed of the reaction. At low overpotentials, this equation is approximately linear, and at high overpotentials it is approximately exponential. Therefore, surface reaction kinetics result in a polarization term which is logarithmic with respect to the current density. The Butler-Volmer model only applies at a steady state and is not applicable to the electrodeposition of Li_2S.

$$j = j_0 \left[exp\left(\frac{\alpha_a z F \eta}{RT}\right) - exp\left(\frac{\alpha_c z F \eta}{RT}\right)\right] \tag{1.6}$$

Low conductivity of lithium ions in the electrolyte is another common source of polarization. The overpotential associated with ionic resistivity is an Ohmic (i.e. linear) function of current density which eventually dominates over the kinetic overpotential at high rates. The effective ionic conductivity is related both to the intrinsic conductivity of the electrolyte and the geometry of the porous electrode. Electrodes with high tortuosity haev lower effective conductivity because ions have to travel farther[33, 34].

Kinetics of Electrodeposition Processes

The full reduction of polysulfides to insoluble lithium sulfide accounts for the majority (75%) of the Li-S battery's theoretical capacity and involves a nucleation and growth process, as shown in Fig. 1-3. Electrodeposition is a mature area of research, but it is not commonly studied in the context of batteries, although some studies have recently been published on the deposition of insoluble oxides in lithium-oxygen batteries[35, 36, 37, 38].

Kinetics of nucleation and growth processes with constant driving force are described by the Johnson-Mehl-Avrami-Kolmogoroff equation (referred to in this thesis as simply the Avrami equation)[39, 40]. This is typically applied to constant-temperature phase transformations (e.g. solidification from a melt with a fixed amount of undercooling) but can also be applied to electrodeposition at a constant voltage; overpotential, like undercooling, provides a thermodynamic driving force. If a fixed areal density N_0 of nuclei form on a surface and they are constrained to grow only laterally and at a fixed rate k, then the fraction covered by the resulting crystallites is given by Equation 1.7 if there is no impingement (touching) of nuclei

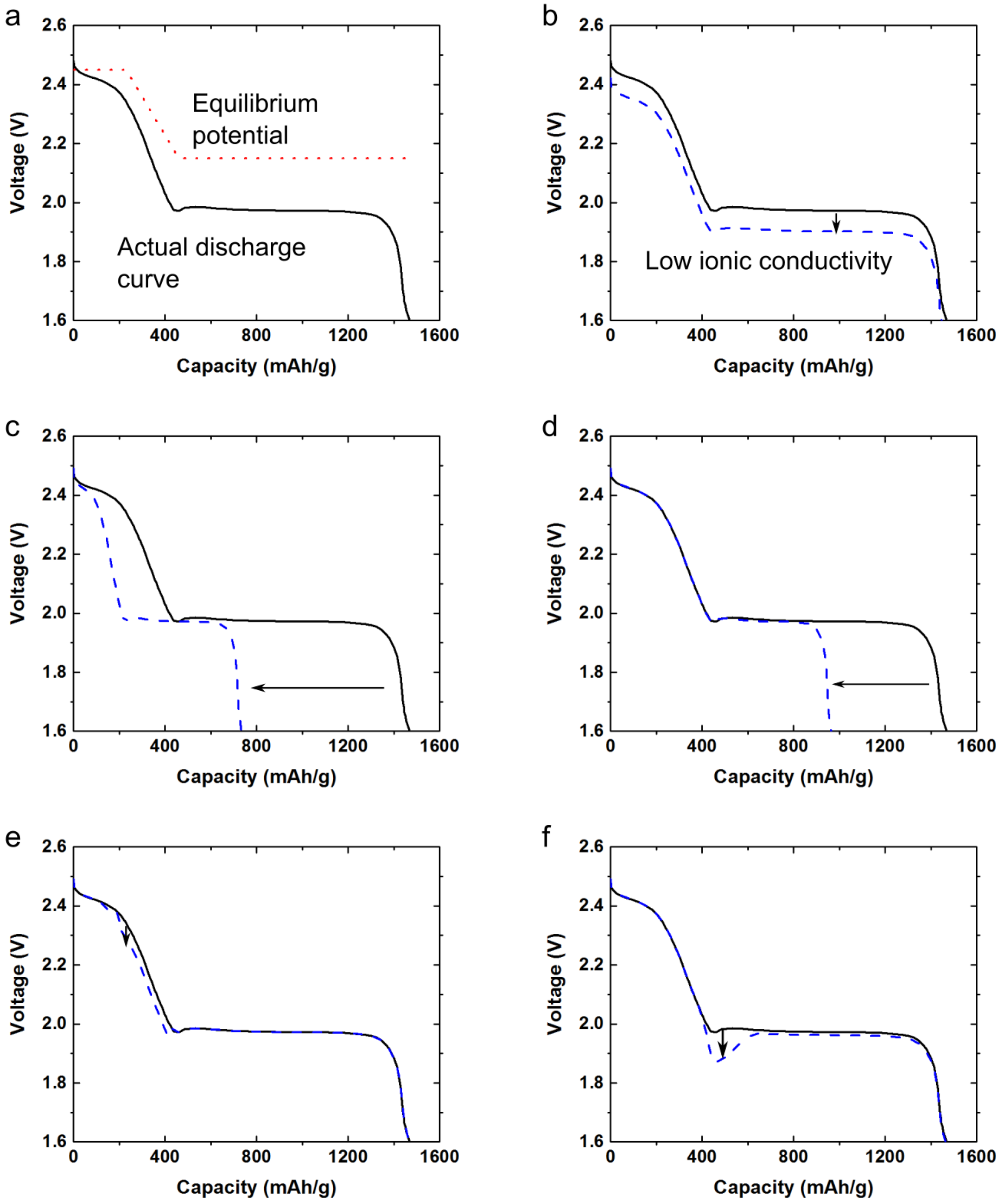

Figure 1-5: Effects of changes in various parameters on discharge performance of a lithium-sulfur cell: (a) A typical discharge curve (black), compared to the equilibrium potential. (b)Lower ionic conductivity, (c) Lower sulfur utilization, (d) Incomplete precipitation of Li$_2$S, (e) Lower exchange current density in the solution regime (f) Slower nucleation kinetics. (The original discharge curve is shown as a solid black curve.

$$Y_{ex}(t) = N_0\pi(kt)^2 \tag{1.7}$$

Although this is an accurate approximation at very short times, eventually this expression exceeds unity due to the fact that each crystallite is assumed to expand indefinitely regardless of the presence of other crystallites which may impinge on it. An adjustment must be made to account for impingement, Equation 1.8. At short times, this reduces to Equation 1.7, but at long times it converges to unity.

$$Y(t) = 1 - exp\left[-N_0\pi(kt)^2\right] \tag{1.8}$$

In most electrodeposition experiments, the deposited material (typically metal) is conductive and material continues to deposit on top of these islands. The surface reaction rate is fast, and deposition rates at long times are governed by diffusion limitation [41, 42, 43]. That is, near the working electrode, species become depleted, and the reaction rate is limited by diffusive transport along the resulting concentration gradient. This is described by the Scharifker-Hills model (Fig. 1-6a and Equation 1.9), in which t_m is the time at which the maximum current occurs, D is the diffusivity of the active species, c is its bulk concentration, and z is the number of electrons transferred. At long times current decreases and converges to the Cottrell equation (Equation 1.10).

$$J(t) = \frac{zFc\sqrt{D}}{\sqrt{\pi t}}\left[1 - exp\left[-1.2564(t/t_m)\right]\right] \tag{1.9}$$

$$J(t) = \frac{zFc\sqrt{D}}{\sqrt{\pi t}} \tag{1.10}$$

In the case of lithium sulfide (and the lithium peroxide found in Li-O_2 batteries), the electrodeposited material is a poor electronic conductor, and therefore additional material cannot readily deposit on top of existing material as is the case in more common metal electrodeposition. This situation, in which the deposited material forms a passivating film on the electrode, has been extensively studied by Thirsk

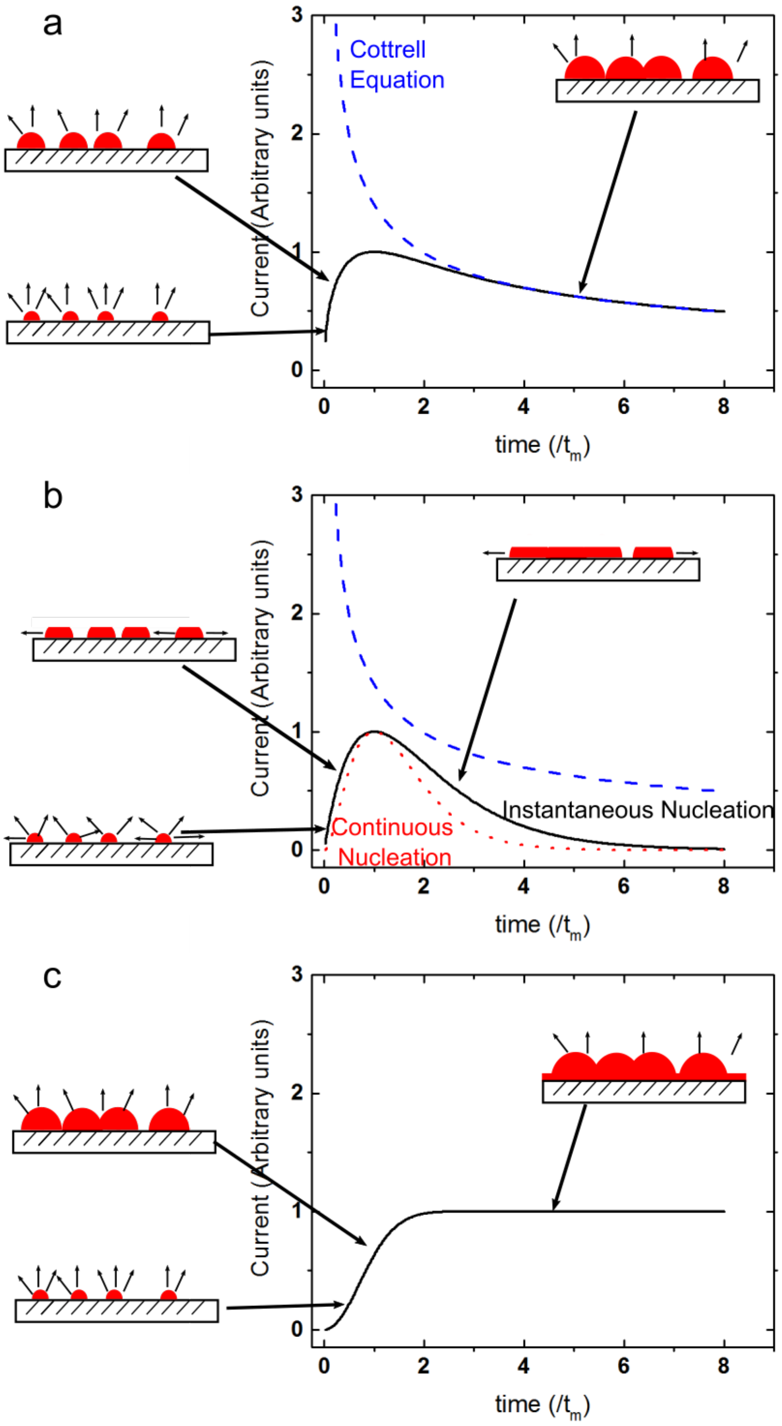

Figure 1-6: Schematic diagrams showing progression of electrochemically driven nucleation and growth processes under several conditions, with plots of current density vs. time. (a) Diffusion-limited 3D growth (b) Reaction-limited 2D growth, with both instantaneous and progressive nucleation shown in current-time plot. (c) Surface-limited 3D growth.

and co-workers [44, 45]. All current comes from the island growth process described in Equation 1.8, and the resulting current is simply proportional to its derivative (Equation 1.11). At long times charge transfer at the surface, rather than diffusive transport in the solution phase, becomes limiting, and the current vs. time curve cannot be fit to the Cottrell equation and converges quickly to zero, as illustrated in Fig. 1-6b and Equation 1.11.

$$J(t) = \frac{2\pi nFhN_0k_1t}{v}\left[1 - exp(-\pi N_0 {k_1}^2 t^2)\right] \tag{1.11}$$

In this equation, h is the height of the islands, and v is the molar volume of the deposited material. When electrodeposition is reaction-limited but there is a significant amount of vertical growth, the process at long times is simply uniform, one-dimensional growth in the vertical direction, and the current eventually tends to a constant, as shown in 1-6c and Equation 1.12, in which k_1 and k_2 are respectively the lateral and vertical growth rates of the islands (in velocity units).

$$J(t) = \frac{nFk_2}{v}\left[1 - exp(-\pi N_0 {k_1}^2 t^2)\right] \tag{1.12}$$

1.3 Overview of the Thesis

This thesis experimentally investigates rate limiting mechanisms in lithium-sulfur batteries using solutions of lithium polysulfides. The remainder of the thesis is organized as follows:

Chapter 2 demonstrates for the first time the successful operation of a high energy density lithium polysulfide flow battery which can be cycled well into the Li_2S precipitation regime. This is enabled by a percolating network of nanoscale carbon black with provides significantly higher surface area and hence better kinetics than a conventional flow battery architecture using a stationary carbon fiber current collector. Insights gained from the use of polysulfide solutions as an active material in this device were applied to experiments performed in Chapters 3-6.

Chapter 3 is a systematic study of ionic conductivity and redox kinetics of polysulfides in the solution regime. Both parameters are highly dependent on both polysulfide concentration and on solvent choice, with faster kinetics and higher conductivity in shorter chain glyme solvents and at lower polysulfide concentrations. Ionic conductivity is found to be highly correlated to solution viscosity.

Chapter 4 characterizes the mechanism and kinetics of lithium sulfide electrodeposition from polysulfide solutions, as well as the dependence of Li_2S morphology on discharge rate. Electrodeposition of Li_2S is found to proceed by a nucleation and 2-D growth process first described by Bewick, Fleischmann, and Thirsk[45]. As in Chapter 3, kinetics are found to be highly dependent on solvent choice and may result from a similar effect. The morphology of deposits during galvanostatic cycling are dependent on discharge rate, with film-like morphology at high rates and larger, discrete grains at low rates.

Chapter 5 introduces a model for 3-D electrodeposition under the influence of a redox mediator, an additive that provides a parallel path for polysulfide reduction away from the current collector surface and allows growth of Li_2S on top of existing deposits. This delays the onset of island impingement on the carbon surface and increases the amount of Li_2S that may be deposited on a given surface area.

Chapter 6 describes the effects of polysulfide concentration and deposition surface on electrodeposition kinetics. Low electrolyte/sulfur ratios increase the concentration of polysulfide intermediates in the electrolyte during cycling, and high polysulfide concentrations are found to result in sluggish nucleation and growth of Li_2S. The use of conductive oxides such as indium tin oxide (ITO) and aluminum-doped zinc oxide (AZO) in place of carbon is shown to ameliorate this effect and reduce polarization at low E/S ratios.

The kinetics of these processes have hitherto been largely unexplored, and this thesis provides new insights into these processes. This information enables the rational design of electrolytes and sulfur cathodes with high energy density and rate performance.

Chapter 2

Lithium Polysulfide Flow Batteries Enabled by Nanoscale Conductor Networks

The contents of this chapter were first published in Ref. [46]. Frank Fan and Zheng Li developed the electrode compositions and conducted the electrochemical cell tests. William Woodford conducted the electron microscopy, carried out exchange current density measurements, and interpreted the rate-limiting mechanisms. Kyle Smith and W. Craig Carter modeled and interpreted the flow cell data. Nir Baram measured suspension and cell electrical properties. Ahmed Helal and Gareth H. McKinley measured and interpreted flow electrode rheology.

2.1 Introduction

Renewable energy generation technologies such as wind and solar suffer from intermittency, while existing baseload nuclear and fossil fuel generation plants are most efficient and long-lived when operated at constant output. There exists an unmet need for low-cost, efficient energy storage at gigawatt-hour scale capacity, either as large centralized plants or smaller units co-located with distributed generation, to facilitate the growth and integration of renewable energy.

Flow batteries are a promising form of large-scale electrochemical energy storage[47, 1]. A flow battery differs from a regular battery (for example, lithium-ion) in that the active materials are in the form of liquids (sometimes known as the anolyte and catholyte for the negative and positive electrodes, respectively) stored in tanks and flowed through an electrochemical stack (comprising current collectors and a separator) as needed, to charge or discharge. In contrast, a standard battery has a static, solid layer of active material sandwiched between layers of current collector and separator (Fig. 1-1). In this way, a flow battery is similar to a fuel cell, except the active materials are stored in tanks and recharged after use, rather than simply rejected as in a fuel cell. This architecture (schematic in Fig. 2-1a) is well suited to long-duration grid storage due to the ability to decouple stored energy (the tanks) from power (the stack), inherent scalability, and potentially low cost. Lowering the cost of stored energy below ∼\$100/kWh at system level remains a challenge, however[5].

The most mature flow battery chemistry is the all-vanadium redox flow battery(VRFB), which uses vanadium redox reactions on both the positive and negative sides[48, 49, 47]. The VRFB has a number of limitations that reduce its energy density and increase its cost. For example, the VRFB is an aqueous battery, so its cell voltage is limited by the electrochemical stability window of water, which is only 1.23V. Moreover, vanadium only has a solubility of around 2 mol/l in the electrolyte (sulfuric acid)[47]. These two factors limit the energy density of the active materials to only about 30 Wh/L. Although flow batteries are intended for stationary applications not constrained by weight or volume, low energy density increases the overall system size, thereby increasing overall cost. Finally, vanadium is a relatively expensive material, approximately \$30/kg as V_2O_5, which translates to approximately \$90/KWh for the vanadium alone. Many aqueous solution-based flow battery chemistries are known, all of which have historically been used in some variant of the same basic flow cell architecture and have similarly low energy density, operating at $<$ 1.2 V cell voltage with ∼1-2 M solution concentrations[47].

Lower-cost, higher energy density (Wh/l) flow chemistries that decrease system size and associated hardware costs, and approaches that minimize or avoid use of

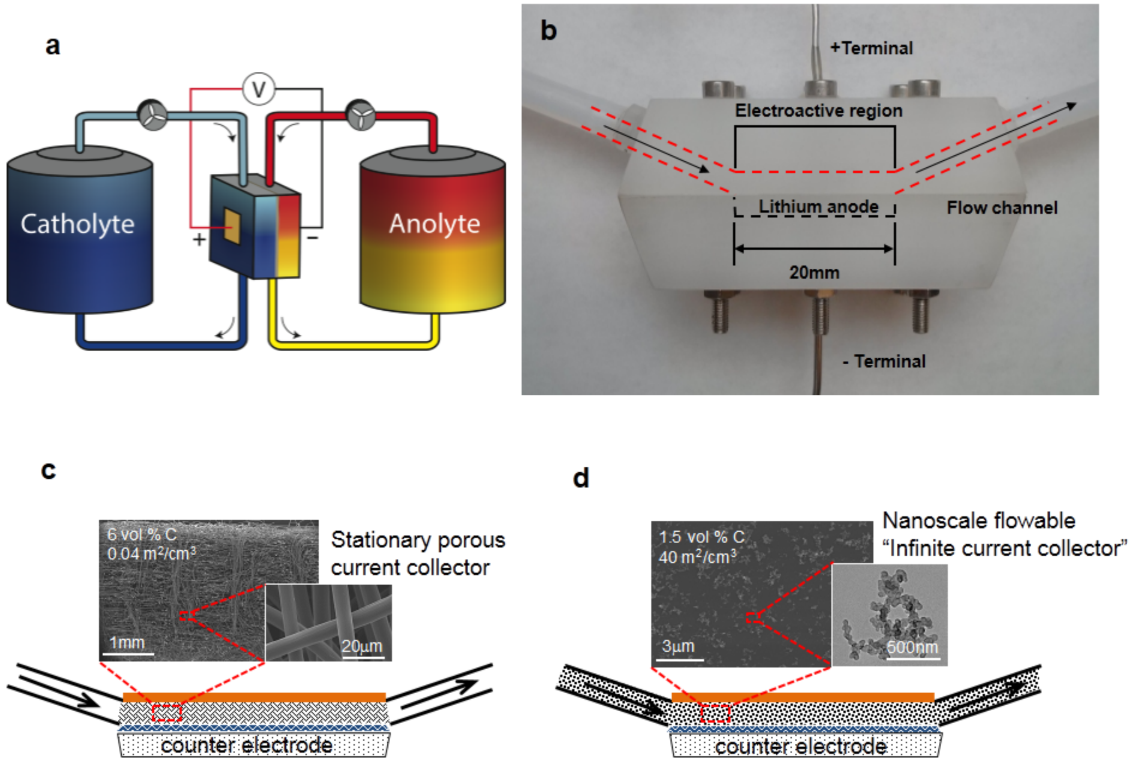

Figure 2-1: Conventional flow battery versus new scheme. (a) Flow batteries combine a current-extracting stack, through which redox active solutions flow, with storage tanks and pumps. In conventional flow batteries, the electrodes are electronically insulating fluids that react only upon charge transfer to porous current collectors typically based on carbon or metals. (b) Laboratory half-flow cell used in current work to compare (c) conventional flow cell architecture using stationary carbon fiber current collector with (d) new scheme providing electronically conductive flowing redox electrodes based on nanoscale percolating networks of conductor particles forming an embedded, self-healing current collector. The mixed-conducting fluid allows charge transfer reactions throughout the volume of the flow electrode.

high cost components such as ion-selective membranes, are desirable. Promising new approaches include semi-solid flow batteries using suspensions of solid storage compounds as flow electrodes[50, 51, 52], and several new classes of solution reactants including lithium polysulfide solutions[53, 54], all-organic redox couples[55], and ionic liquid based complexes[56]. However, as energy density increases, several barriers to efficient extraction of electrochemical energy are inevitable. Increases in solution molarity, especially for large molecules facilitating high solubility, are accompanied by higher viscosities leading to higher driving pressures and greater flow resistance. Reaction rates will typically decrease, due to sluggish bulk diffusion or less facile interfacial reaction rates (i.e., Butler-Volmer exchange current density). These sources of polarization are further compounded by the higher absolute current densities that are necessary to utilize higher volumetric energy at equivalent rate. All of the above tend to lower cell-level coulombic and energetic efficiency.

Here we demonstrate a new approach, broadly applicable to flowable redox chemistries, including those which undergo precipitation-dissolution reactions, whereby percolating networks of nanoscale conductor particles are incorporated within fluid electrodes forming an embedded, self-healing current collector enabling highly distributed electrochemical reactivity throughout the electroactive zone of flow batteries. In contrast to conventional flow battery designs wherein the electronically-insulating redox fluids undergo charge-transfer reactions only upon contact with the stationary porous current collector (Fig. 2-1c), the new scheme produces an electronically conductive fluid (i.e., a "liquid wire", Fig. 2-1d) that acts as its own current collector, providing for charge transfer to the external circuit. The continuous nanoconductor network vastly increases the available charge-transfer area while also reducing the molecular diffusion length between electroactive sites. As we show, in the high ionic strength environment of liquid electrolytes, nanoscale carbon conductor particles undergo diffusion-limited aggregation leading to electronic percolation at remarkably low volume concentrations of <1%, and reach 5-20 mS/cm electronic conductivity for only 1-3 vol% solids in non-aqueous electrolytes, providing excellent mixed electronic-ionic conduction with negligible impact on energy density. We use lithium-polysulfide (Li-PS) as a test system, and show that the new electrode architecture allows electrochemical utilization that is increased fivefold over the same solutions used in a conventional flow cell architecture, reaching near-theoretical reversible capacities at practical current rates (e.g., corresponding to 4-15 h duration stationary storage). A lithium-polysulfide flow battery operating in both continuous-flow and intermittent-flow modes is demonstrated for the first time.

The last few years have seen renewed interest in lithium-sulfur (Li-S) batteries[11, 57, 13], long considered an attractive energy storage chemistry for its high theoretical energy density (2567 Wh/kg and 2199 Wh/l for elemental Li and S as reactants) and low active materials cost. However, only recently has the adaptation of Li-S chemistry to flow batteries been considered. The high solubility of polysulfides Li_2S_x in nonaqueous electrolytes has historically been detrimental in Li-S batteries as it provides a "shuttle" mechanism for internal self-discharge as well as capacity loss due to incidental Li_2S precipitation within electrochemical cells[58]. It has been suggested that the same attributes could be exploited in flow batteries[53, 54, 13], with analysis indicating low storage cost ($45/kWh for the raw materials[53]) even when electrochemical cycling is limited to the solution regime between Li_2S_8 and Li_2S_4 where no precipitation occurs (Fig. 2-7a). In contrast to the need to minimize polysulfide solubility in a conventional Li-S electrolyte to decrease self-discharge, a high polysulfide solubility is desirable to increase the energy density and reduce the system-level cost of flow batteries. Reversible cycling has recently been demonstrated for 2.5 M to 5 M (sulfur basis) Li-PS catholyte solutions infiltrated into carbon paper current collectors against self-passivated Li metal negatives electrodes in a non-flowing "membraneless" cell configuration[53]. In the present work, we used similar Li-PS solutions in a half-flow cell against Li metal negative electrodes, the catholyte solutions being composed of Li_2S_8 dissolved in tetraethylene glycol dimethyl ether (TEGDME) containing 0.5 M bis(trifluoromethane)sulfonimide lithium salt (LiTFSI) and 1 wt. % $LiNO_3$ as the lithium electrode passivation additive[28, 59]. By starting with Li_2S_8 the sulfur precipitation regime at high charge voltage (Fig. 2-7a) is excluded and the starting flow electrodes have Li-PS purely in solution form. Only a microporous separator film (Tonen Chemical Corporation) separates this catholyte and the Li metal negative electrode. The theoretical specific capacity of the solution upon discharging Li_2S_8 to the Li_2S_4 liquid solution limit is 210 mAh/g, while that for discharging to Li_2S precipitation is 1460 mAh/g (Fig. 2-7a); at 2.5 mol S/l concentration, as used in our flow experiments, the catholyte energy density (vs. Li^+/Li^0) is 34 Wh/l and 234 Wh/l for discharge to the solution and precipitation limits, respectively. Clearly, it is desirable to utilize storage capacity in the precipitation regime. (Herein, all specific capacities given in mAh/g refer to capacity per gram of sulfur.)

2.2 Methods

Preparation of flow electrodes

To prepare the lithium polysulfide solution, Li_2S, sulfur, LiTFSI, and $LiNO_3$ were dried under vacuum for 24 h at 100 °C and added to TEGDME and stirred for 24 h in an Ar-filled glovebox, at 60°C. To prepare the suspension, carbon black (KetjenblackEC-600JD, AkzoNobel) was added to the aforementioned solution, manually stirred, and then sonicated for 30 minutes. LiTFSI and $LiNO_3$ were obtained from Sigma-Aldrich, while the sulfur, Li_2S, and TEGDME were obtained from Alfa Aesar.

Microscopy Characterization

Scanning electron microscopy of the carbon felt was carried out using a FEI/Philips XL30 environmental SEM with secondary electron detector operating at 25 kV accelerating voltage. Suspensions were imaged in QuantomiX WETSEMő QX-102 capsules using the FEI/Philips XL30 with a backscattered electron detector and accelerating voltages of 20-30 kV. The dry Ketjenblack powder was imaged on a JEOL 2010F transmission electron microscope with an accelerating voltage of 200 kV. Samples were prepared by dispersing the carbon black on a Cu grid coated with an amorphous carbon film.

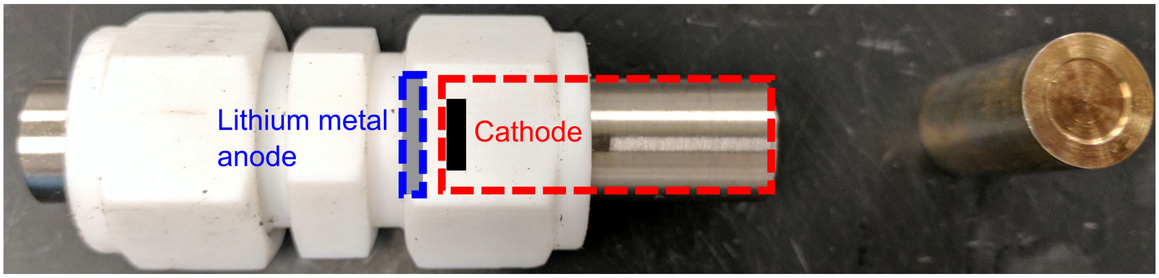

Figure 2-2: Swagelok® cell used for non-flowing electrochemical tests. Liquid and semi-liquid cathode solutions and suspensions are held in the gold-coated current collector(right) with a well 0.5mm or 2.8mm deep. The image on the left is an assembled cell, showing orientation and approximate positions of the anode (outlined in blue) and cathode (black, with current collector outlined in red.)

Exchange current density measurements

In the galvanostatic polarization experiment, the polysulfide solution was vigorously stirred to ensure no mass-transport limitation, while a specified current was drawn from the cell using a 3 mm glassy carbon working electrode (CH Instruments, Inc.) for 30 minutes. The corresponding potential was determined as the average potential during the 30 minute galvanostatic step. In the steady-state voltammetry experiments, an 11 μm carbon-fiber microelectrode (BASi, Inc.) was used as a working electrode and the potential was swept cathodically at 20 mV/s from 3.24 V vs. Li^+/Li to 1.24 V.

Cycling experiments in non-flowing half-cells

Swagelok® type cells with 0.5 mm and 2.8mm deep wells were used for cathode solutions and suspensions (Fig. 2-2). A Tonen separator soaked with electrolyte was used to separate the cathode current collector from the Li metal anode. All cell assembly was performed inside an Ar-filled glovebox.

Flow cell experiments

The lab-scale flow cell used for intermittent and continuous flow experiments was machined from polyvinylidene fluoride (PVDF), with an electroactive region machined from nickel and sputter-coated with gold. The electroactive region was 20 mm long, with square cross sections ranging from 1 mm to 2.8 mm width. For a 1 mm channel, the channel volume was 20 μl, with an active membrane area of 0.2 cm^2. The cell was connected with polytetrafluoroethylene (PTFE) tubing to gastight glass syringes (Hamilton Model 1005), which were driven using syringe pumps (neMESYS, Cetoni GmbH). Electrochemical testing was performed using a Bio-Logic VMP3 potentiostat.

EIS and IS measurements

Electrochemical impedance spectroscopy (EIS) measurements were made in Swagelok-type cells (Swagelok Co.) with a PTFE body, cathode well 6.35 mm in diameter and 2.8 mm deep, and with Li metal as a counter and reference electrode. The measurements were taken with Li_2S_8 solutions, 2.5 mol S/l in TEGDME with 0.5 M LiTFSI supporting electrolyte. The suspension has 1.5 vol% Ketjenblack. The well is Au coated Ni. When characterizing the solution electrode, 3 mm thick carbon felt was cut to fit the cathode well and compressed to 2.8 mm thickness upon assembly. When measuring the suspension electrodes, the suspensions were spatula-loaded into the well and covered with a circular piece of separator film. A circular film of lithium metal, attached to a stainless steel current collector, was applied against the well by light spring force.

Impedance spectroscopy(IS) electronic and ionic conductivity measurements were made in a similar two-electrode cells using gold-sputtered current collectors on both sides. Measurements were taken over the course of one to two hours.

The EIS measurements used the Solartron 1400 system with a Solartron 1455 frequency response analyzer. The experiments were performed in with cells in the fully charged (as-assembled) state. Sinusoidal voltage oscillations of 10 mV amplitude were applied about the cell's open circuit voltage between the two electrodesSinusoidal voltage oscillations of 10 mV amplitude were applied about the cell's open circuit voltage between the working and reference electrode, while the current response was monitored between the lithium counter electrode and working electrode. Oscillation frequencies were swept logarithmically from 0.01 Hz to 1MHz. The mea-

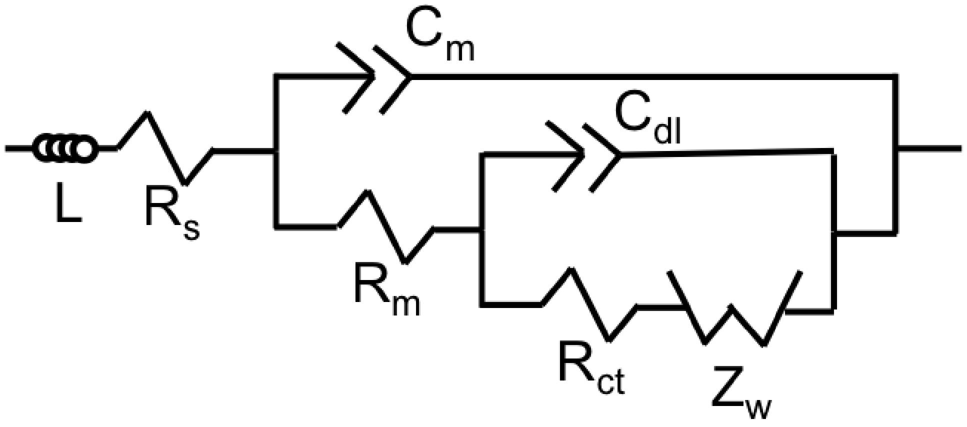

Figure 2-3: Equivalent circuit used to fit electrochemical impedance spectra of the suspension and fiber electrodes.

sured impedance data were fit to an equivalent circuit by a complex nonlinear least squares regression. For the IS measurements, a Solartron Analytical model 1470 potentiostat and model 1455 frequency response analyzer were used to apply either a ±50 mV AC or DC bias. The DC measurements were taken at a steady state value after a 15 minute hold. Resistances were converted to conductivities by dividing by the experimental cell factor, calibrated to be 1.2 cm^{-1} using a 15 mS/cm conductivity standard produced by Oakton Instruments.

Rheological characterization

The viscometric behavior of the different solutions and semi-solid suspensions was measured using a Malvern Kinexus Pro torsional rheometer enclosed in a glovebox with an Argon atmosphere (H_2O and O_2 levels < 0.1 ppm). Steady shear viscometry tests, as well as, small amplitude oscillatory frequency sweeps, were performed using a smooth parallel plate geometry (D = 40 mm; mean roughness R_q=0.36 μm). All tests were performed at T = 25°C and the temperature was regulated with a Peltier plate system. Steady shear tests were performed with decreasing applied shear rates as described by Ovarlez et al.[60] to insure the existence of a simple yield stress for the material and avoid possible transient shear banding. In addition, following the protocol proposed by Yoshimura and Prud'Homme[61], the same sample was tested at

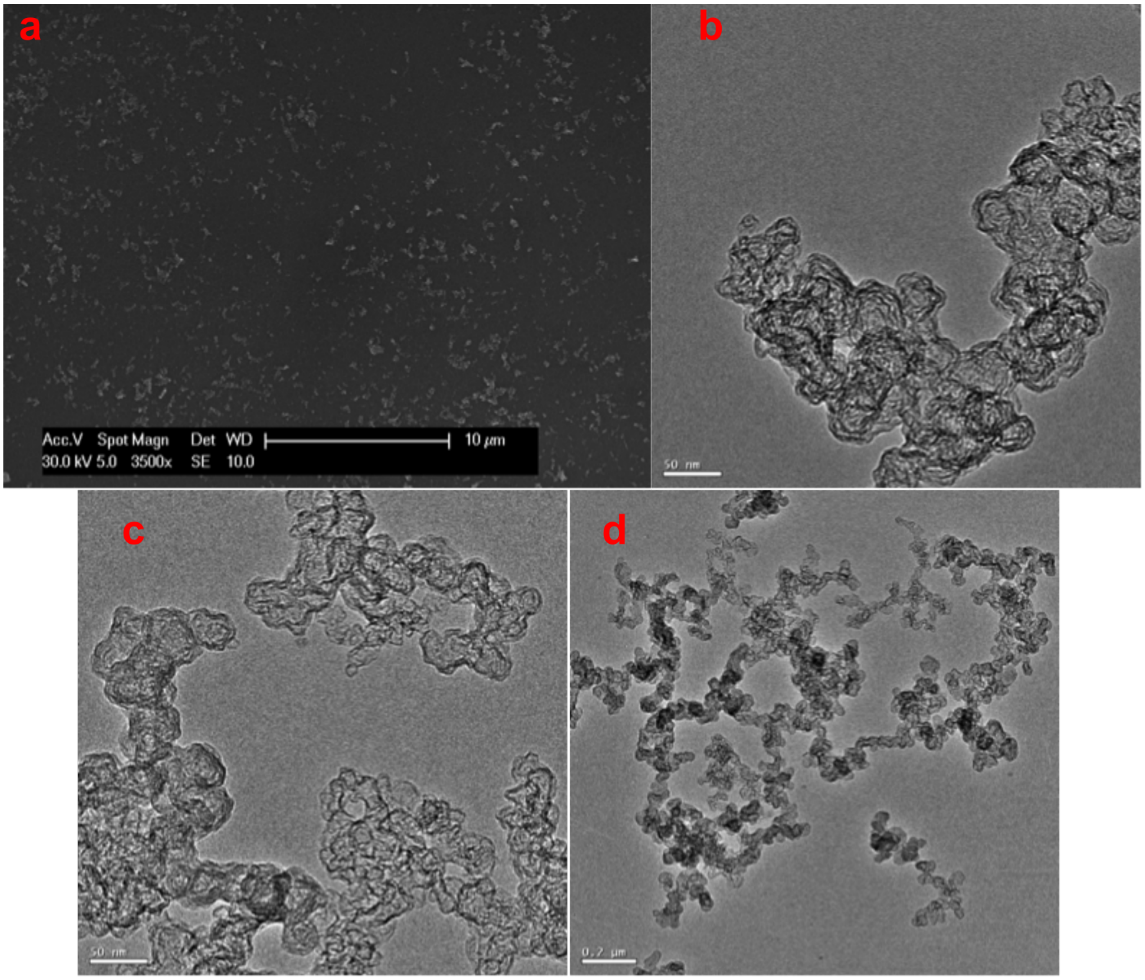

Figure 2-4: (Upper left) Microstructure of 1.5 vol% Ketjenblack suspension in polysulfide solution in TEGDME in a wet SEM cell, (upper right) microstructure of dry Ketjenblack primary aggregate, and (lower) several dry Ketjenblack aggregates.

three different gaps (H = 1 mm, 0.75 mm, 0.5 mm respectively) to probe and correct for slip effects. If the flow curves at different gaps superimpose, the material does not slip. If gap-dependent rheology is observed, a correction needs to be applied to extract the true shear rate applied on the sample at each value of the applied stress.

2.3 Results and Discussion

To implement the nanoconductor suspension approach, several nanoscale carbons including carbon blacks and single- and multi-wall carbon nanotubes (SWNTs and MWNTs) were dispersed in the Li-PS solution, and their conductivities and rheo-

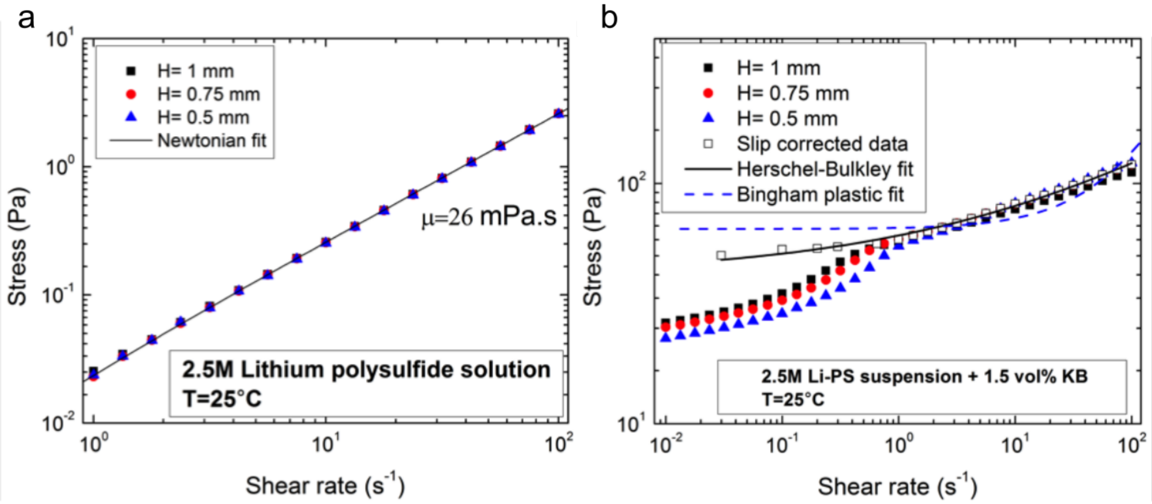

Figure 2-5: Flow curves for (a) polysulfide solution and (b) suspension with 1.5 vol% KB, measured at different gaps. The solution used in both tests is 2.5 mol S/l polysulfide, and testing is performed at 25°C. The polysulfide solution exhibits Newtonian (linear) liquid behavior. The suspension is fit to the Herschel-Bulkley model and the Bingham plastic model.

logical properties measured, following methodologies developed in previous work on semi-solid flow batteries[50]. For our purposes, the ideal nanoscale conductor provides the highest electronic conductivity at the lowest volume fraction and with the lowest yield stress and viscosity. Amongst the nano-carbons tested, one particular carbon black (Ketjenblack EC-600JD, AkzoNobel, hereafter referred to as KB) met these criteria best. KB is a 1400 m^2/g nanoscale carbon with ∼30nm primary particle size (TEM images in Fig. 2-1 and Fig. 2-4). Surprisingly, electrical percolation producing 2 mS/cm electronic conductivity is observed at as low as 1 vol% KB, increasing to 9 mS/cm by 1.5 vol% carbon and 18 mS/cm by 2 vol% KB (inset of Fig. 2-7b). Since the room temperature ionic conductivity of the Li-PS solution is 1.5 mS/cm, the suspensions have the unusual characteristic of being mixed electronic-ionic conductors in fluid form. Jamming behavior in suspensions of small particles has been studied theoretically and experimentally[62]; for instance small amplitude oscillatory shear rheometry detects mechanical percolation of micron-scale carbon particles in nonaqueous media at volume concentrations of ∼5 vol%[63]. This is already much lower than the ∼30 vol% percolation threshold for non-interacting like-sized spheres

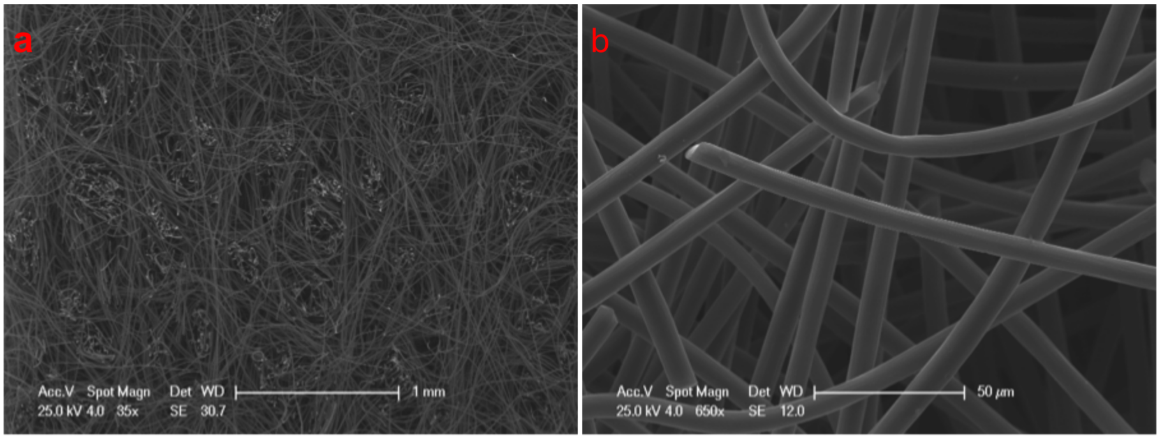

Figure 2-6: Microstructure of the carbon felt at low (left) and high (right) magnification.

in three dimensions, and has been attributed to diffusion limited aggregation (DLA) of strongly attracting particles into fractal networks (i.e., "hit and stick" behavior). The still-lower electrical percolation threshold observed here is attributed to the combination of nanoscale particle size and high ionic strength (true of any liquid electrolyte), which will further strengthen the attractive DLA interactions by quenching Debye-Huckel electrostatic double-layers that could produce interparticle repulsion. Limited tests of solutions with and without LiTFSI showed a factor of two higher DC conductivity when salt is used. Two-dimensional sections observed in wet-cell SEM (Fig. 2-1b) are consistent with a low-density three-dimensional solids network[64]. Viscometry showed that the 2.5 mol S/l solution has Newtonian rheology with 15 mPa s viscosity, whereas the nanoparticle suspension based on the same solvent with 1.5 vol% KB has Bingham plastic rheology with 64.6 Pa yield stress and 710 mPa-s plastic viscosity. The nanoparticle suspension has a rheological response at room temperature that is qualitatively similar to ketchup, and is readily pumped in the flow battery experiments described later.

Electrode Tests in Non-Flowing Cells

Electrochemical testing in half-cells of membraneless configuration (i.e., using only the separator film to prevent electrical contact of the two electrodes) showed that

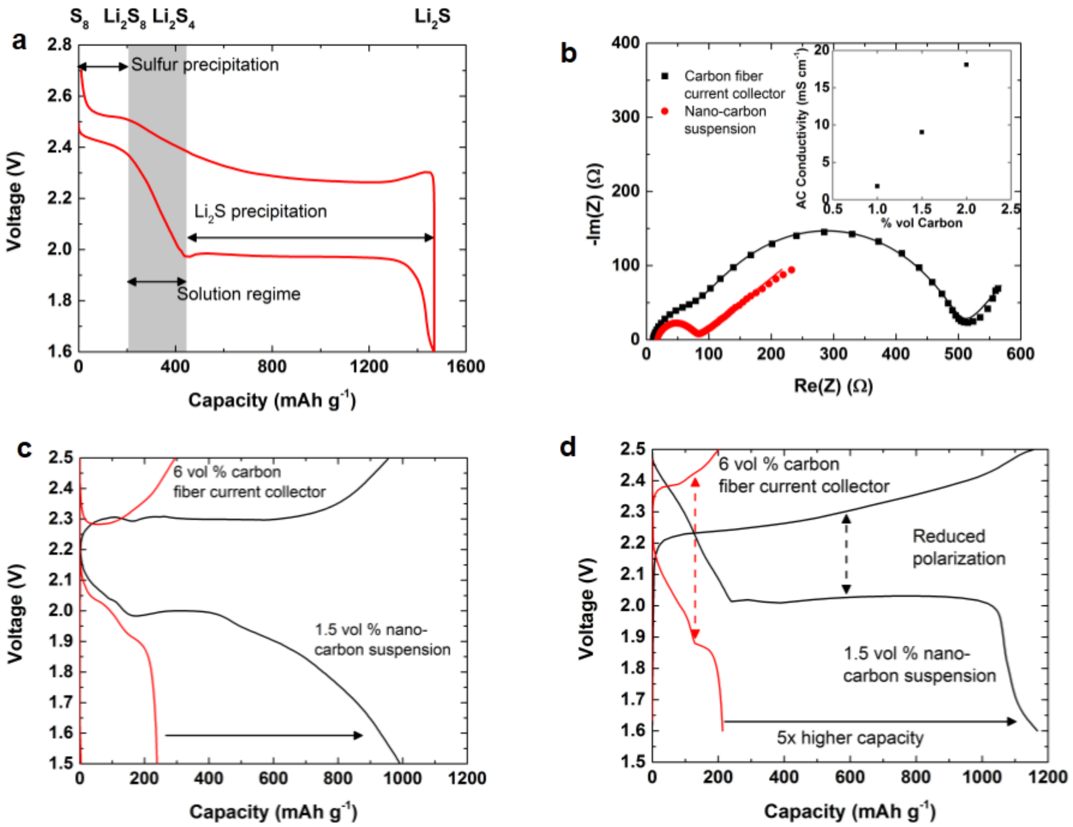

Figure 2-7: (a) The Li-sulfur reaction upon discharge proceeds by the lithiation of elemental S_8, followed by a regime of soluble polysulfides between compositions Li_2S_8 and Li_2S_4, then the precipitation of Li_2S. Attaining high specific capacity requires precipitation of Li_2S. In this work, starting solutions contain Li_2S_8 and were discharged within and beyond the solution regime, respectively. (b) Electrochemical impedance spectroscopy comparing cells with identical 2.5 mol S/l solutions (as Li_2S_8 in TEGDME with 1 wt% $LiNO_3$ with 0.5M LiTFSI) in the conventional architecture with carbon felt current collector and the nanoscale conductor suspension (1.5 vol% KB). A much smaller charge-transfer resistance (leftmost red arc) is seen for the latter. (c) and (d) Four- to fivefold higher reversible capacity is seen for the nanoscale conductor suspension over the conventional flow cell design when cycling over 2.5-1.6V to include the precipitation regime, in both 3.0 mm and 0.5 mm thick electrodes. Charge-discharge curves are the second galvanostatic cycle for each cell.

the *in situ* nanoparticle conductor network markedly enhances the electrochemical utilization of the polysulfide solution. Fig. 2-7c and 2-7d show direct comparisons of the same 2.5 mol S/l polysulfide solution in non-flowing half-cells with a carbon fiber current collector, and with a carbon nanoparticle suspension. The carbon fiber current collector used here and in the flow cells is a low-flow-resistance non-woven "felt" (SGL GFD3, Fig. 2-1c, Fig. 2-6) widely used in aqueous flow batteries. For 2.8 mm-thick electrodes tested at C/50 galvanostatic rate, the capacity of the nanoparticle suspension is a factor of 4 greater than that of the conventional configuration, reaching 1000 mAh/g specific capacity. For thinner 0.5mm electrodes tested at a higher C/4 rate, the capacity of the suspension electrode reaches 1200 mAh/g (vs. 1460 mAh/g theoretical capacity), about a factor of 5 greater than with the fiber current collector. Note that the discharge curve for the Li-S system has three distinct regions (Fig. 2-7a). There is a high voltage plateau (∼2.5 V) through which solid sulfur coexists with soluble lithium polysulfides. This is followed by a solution regime with sloping voltage (2.5-2.1 V) over which sulfur is fully dissolved as soluble polysulfides, then a lower voltage plateau (∼2.0 V) where the discharge reaction proceeds via precipitation of the insoluble Li_2S. Fig. 2-7c and 2-7d (showing the second cycle in all cases) show that the conventional cell architecture delivers capacity that is primarily in the solution regime. In contrast, the nanoscale suspension has both higher capacity and significantly improved reversibility when cells are cycled to include the precipitation regime. This electrode format provides correspondingly higher capacity and energy density in the same cell. It is also possible to limit cycling to the solution regime, as was done by Yang et al. using non-flowing cells with carbon paper current collectors[53]. As shown in Fig. 2-8, cycling of the nanoparticle suspension over the 2.55V-2.00 V solution regime gave 34% higher initial capacity than the same solution used with the carbon fiber current collector. For the suspension cycled over the solution regime, stable cycling with 56% capacity retention after 100 cycles and 50% retention after 500 cycles was seen. Cycling over the 1.90-2.50 V range to include capacity enhancement from Li_2S precipitation gave fourfold higher initial capacity of 1200 mAh/g (Fig. 2-8). The fade rate was also greater, yielding 610 mAh/g after 100 cycles, or about 50% retention, but this level of capacity retention is in fact superior to many published results for Li-S batteries using solid sulfur cathodes[11, 13, 65]. (Recent results for engineered nanostructures such as sulfur encapsulated in carbon spheres do show significantly better cycling stability[65, 66].) The coulombic efficiency exceeded 95% for cycling within both the solution and precipitation regimes.

Reaction Kinetics and Contributions to Impedance

Contributions to impedance, and the origin of the highly facile reaction in the suspension electrodes, were deconvolved using electrochemical impedance spectroscopy (EIS). The Nyquist plot in Figure 2-7b shows the large difference in cell impedance for the two approaches, which was systematically investigated as follows. We first measured the exchange current density at the interface between carbon and the present Li-PS solutions, using carbon fiber microelectrodes and glassy carbon macroelectrodes as model current collectors. Three types of measurements, each with three-electrode cells, were conducted: 1) steady-state cyclic voltammetry at a carbon fiber microelectrode, 2) galvanostatic polarization at a glassy carbon macroelectrode, and 3) electrochemical impedance spectroscopy using a glassy carbon macroelectrode. For the present Li_2S_8-TEGDME solutions, the three methods give exchange current densities in the range 0.011-0.030 mA/cm^2. Measurements of otherwise identical Li_2S_6 solutions (i.e., chemically prepared in a partially discharged state) showed $\sim$40% higher exchange current densities, while the solution conductivity was essentially unchanged. This shows that as Li-S cells are discharged within the solution regime, the exchange current density increases. To our knowledge these are the first exchange current density measurements for lithium polysulfides on carbon electrodes. Also, these measurements are applicable not only to polysulfide flow batteries, but to standard non-flowing Li-S cells, because the same solution-phase reactions occur in both types of cells. A systematic study of exchange current density in solutions of different concentrations and in different solvents will be presented in Chapter 3.

Next, the EIS results in Fig. 2-7b were separated into three major impedance contributions with the help of independent measurements, using impedance spec-

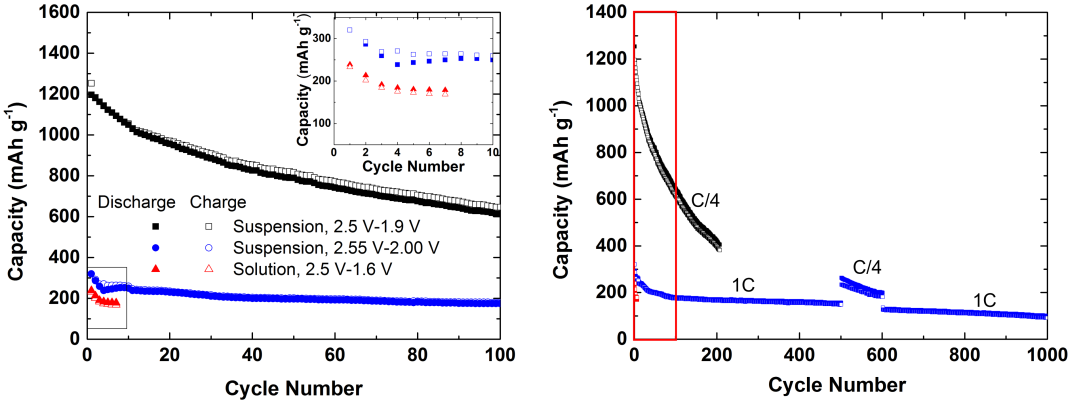

Figure 2-8: Charge and discharge capacity vs. cycle number, at C/4 rate, for non-flowing half-cells containing as cathode the nanoscale suspension flow cathode and the solution alone with carbon fiber current collector. The 2.50-2.00V range permits only polysulfide solutions, while the 2.50-1.90V window incorporates Li_2S precipitation. All cells use the same 2.5 mol S/L starting solution. The nanoscale suspension cycled over solution + precipitation regimes exhibits 1200 mAh/g initial capacity (1460 mAh/g theoretical value) with capacity retention comparable to the state-of-art conventional Li-S cells. When cycled over the polysulfide solution regime, the nanoscale suspension flow electrode shows ∼34% higher initial capacity than the conventional architecture. The plot on the left side shows the first 100 cycles; cycling is continued to 200 cycles in the full 2.50-1.90V window and 1000 cycles in the limited window.

troscopy in the absence of electrochemistry with ion-blocking (gold) electrodes, of the ionic conductivity of the Li-PS solution and the electronic conductivity of the nanoscale suspensions (inset in Fig. 2-7b). As shown in Table 2.1, the solution resistance (obtained from the high frequency intercept with the Re(Z)-axis) and interfacial resistance (the left-most arc) have similar values in the two types of cells, as expected. The difference in cell impedance is dominated by the charge transfer resistance (right-most arc), which in this case includes impedance from the finite electronic conductivity of the carbon network (whether fiber or suspension), as well as the exchange current density (Butler-Volmer kinetics) at the carbon surface. Based on the exchange current density of $\sim$0.01 mA cm^{-2}, the actual current densities and overpotentials can be estimated as follows. The theoretically available carbon-electrolyte interfacial area of the carbon fiber current collector (Fig. 2-1 and 2-6) is $\sim$0.33 m^2 /g based on the $\sim$6 μm fiber diameter. The fiber current collector occupies 6 vol% of the cell, giving a collector surface area per cell volume of $\sim 40\times10^{-3}$ m^2 ml^{-1}. Fig. 2-1c shows the microstructure of the 1.5 vol% KB suspension, viewed in an SEM using a "wet cell" with an electron-transparent window, and a representative primary aggregate in the dry state. The carbon nanoparticles comprise a BET area of $\sim$1400 m^2 g^{-1}, which at 1.5 vol % provides carbon area per unit volume of $\sim$42 m^2 ml^{-1}. Thus the available interfacial area for charge transfer is more than 10^3 greater for the suspension than for the carbon fiber collector, even though there is only one-fourth as much carbon. Assuming all of the carbon-electrolyte interfacial area to be active, and taking the exchange current density to be 0.01 mA cm^{-2} as independently measured, discharging at a C/15 rate from composition Li_2S_8 to Li_2S corresponds to an average current density at the carbon surface of only 1.7×10^{-5} mA cm^{-2} for the nanoscale suspension, while the carbon fiber collector will need to draw 1.7×10^{-2} mA cm^{-2}. The corresponding Butler-Volmer overpotentials are 0.04 and 41.5 mV, respectively.

Further analysis of the charge transfer resistance for the nanoscale suspension suggests that at such low current densities, the surface reaction kinetics may not be rate-limiting at all. If Butler-Volmer kinetics were limiting, the charge transfer resistance is computed to be 0.22 Ω cm^2 for the suspension, which is much lower

sample	solution resistance (Ω cm^2)	interfacial resistance (Ω cm^2)	charge transfer resistance (Ω cm^2)
nanoconductor suspension	5.1	16	3.8
carbon fiber current collector	3.5	31	125

Table 2.1: Comparison of impedance contributions for nonflowing Li/polysulfide cells using the same Li-PS solution with a nanoscale conductor suspension and with a conventional carbon fiber current collector

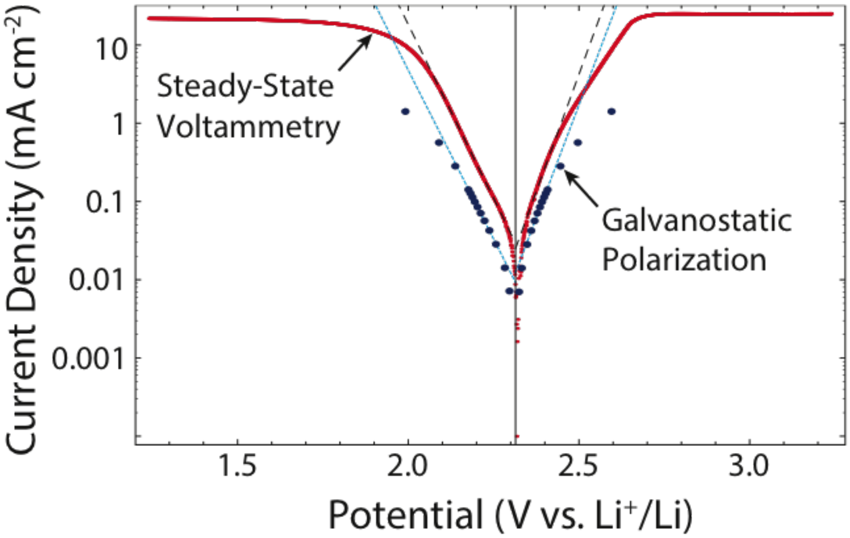

Figure 2-9: Tafel plot of voltammetric measurements of electrochemical kinetics in 2.5 mol S /l Li_2S_8 solutions in TEGDME with 0.5 M LiTFSI supporting electrolyte, measured with galvanostatic polarization(blue) and with steady-state voltammetry at an ultramicroelectrode(red). The linear extrapolations are shown as the dashed lines and the open-circuit voltage is indicated by the solid vertical line.

than the 3.8 Ω cm^2 observed in EIS (Table 2.1), suggesting that the charge-transfer resistance of the nanoscale suspension is dominated by the electronic conductivity of the network. The electronic conductivity of the nanoscale suspension is $\sim$10 mS cm^{-1} conductivity for the 1.5 vol% KB suspension (Fig. 2-7b), within a factor of two of that computed from the EIS charge transfer resistance assuming electronic conductivity to be the only contribution. This in turn implies that further improvements in the electronic conductivity of the nanoscale conductor suspensions could yield higher rate capability. Improvements in solution-phase ionic conductivity may also be expected to yield enhanced rate capability.

Within the precipitation regime, the poor reversibility of conventional Li-S batteries has been widely attributed to the highly insulating nature of Li_2S. Here, we note that if a conformal Li_2S layer of uniform thickness is assumed to form on the carbon surface during full discharge from Li_2S_8 to Li_2S, at 2.5 mol S/l concentration the layer thickness (based on a molar volume of 2.768×10^{-2} l/mol for Li_2S[67]) is 1.7 nm for the nanoscale suspension, compared to 1.7 μm for the carbon felt current collector. Thus the superior capacity and reversibility of the nanoscale suspension can be attributed to a combination of two effects: ultra-low current densities at the catholyte-carbon interface, and a much finer-scale precipitation of Li_2S. Topologically, the embedded, self-healing current collector is in some ways the inverse of the mesoporous carbon hosts for sulfur that have shown promise in conventional Li-S batteries[22]. The current conductive, flowable electrode approach may have benefits for non-flowing metal-sulfide batteries as well, as illustrated by the cell results in Figs. 2-7c and 2-7d.

Flow Cell Tests

Tests performed in a lab-scale half-flow cell (Fig. 2-1b) showed that the vastly improved charge transfer kinetics of the nanoscale suspensions are retained under two types of flowing conditions: 1) continuous flow, which is the typical operating mode of solution-based flow batteries; and 2) intermittent flow, where fluid is pumped in discrete volumes with complete charging or discharging of the electroactive region occurring in between. Intermittent flow has been shown to produce higher round-trip energy efficiency for significantly non-Newtonian redox fluids[50, 68, 69].

To demonstrate cycling under continuous flow, automated digitally-controlled syringe pumps were used with the cell in Fig. 2-1b. The ratio of cell volume to pumped volume was 1:4, and the total volume (80 μL) passes through the cell in 100 min. (i.e., for a flow battery with a single cathode tank, the entire tank volume would circulate once every 100 min.) Results for the nanoscale suspensions appear in Fig. 2-11. During the first 1.5 cycles, the cell was discharged and charged potentiostatically between 2.1 V and 2.5 V (Fig. 2-11) to stay in the solution regime, similar to Yang et al.'s experiments[53]. Since the Li-PS battery is assembled in the charged state, the first half-cycle discharges the cell, whereas the relevant coulombic and energy efficiency for a storage battery is that occurring upon charging and discharging. Efficiencies are therefore only reported for subsequent cycles where there is a full charge/discharge sequence. During the potentiostatic charge/discharge cycle in the solution regime, the discharge capacity is 181mAh/g, the coulombic efficiency is 101% (the higher-than-theoretical value is due to diffusive exchange of charged cathode at the edges of the electroactive zone), and the round-trip energy efficiency is 84.7%. Operating in this regime, the energy density of the flow cathode alone is 30.4 Wh/l (specific energy 380 Wh/kg). To evaluate the energy density of the electrochemical couple, a reasonable excess of Li metal must be assumed. Herein we will assume 100% excess of Li relative to the actual capacity of the cell, in which case the active-materials-only energy density in the solution regime is 26.7 Wh/l (specific energy 334 Wh/kg).

The flow cell results in Figs. 2-11 and 2-12 represent the limit where the flow electrode undergoes a large change in state-of-charge (SOC) per pass. In conventional flow batteries, this is known to result in reaction limitations that reduce power and energy. Conventionally, the power density of flow cells and stacks is measured using linear sweep voltammetry, which represents operation under shallow SOC (many continuous passes to extract energy) and short duration power (e.g., for pulse duty cycles. In Fig 2-10, we have measured polarization curves during continuous flow from 10 nL/s to 10μL/s at a linear sweep rate of 20 mV/s. Note firstly that the peak power reaches ∼37 mW/cm^2 in these unoptimized cells, compared to ∼100 mW/cm^2

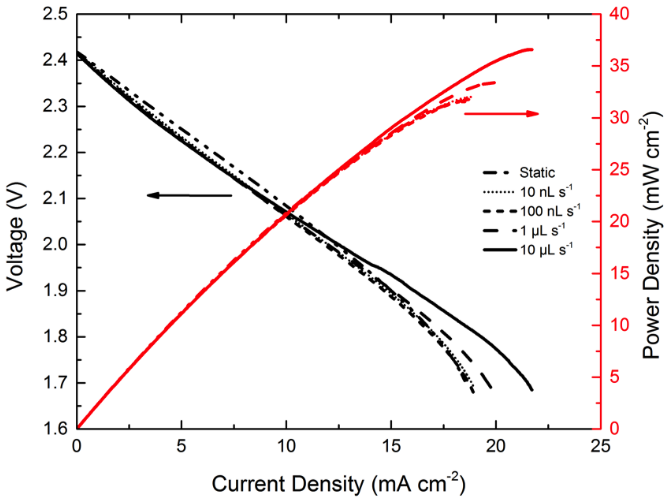

Figure 2-10: Polarization curves measured using linear sweep voltammetry at 20 mV/s for continuous flow rates from 10 nl/s to 10μl/s. Flow cell geometry is as used for results in Fig. 2-11.

for typical aqueous flow battery stacks. Secondly, the power is only weakly dependent on flow rate, suggesting that cell design rather than the flow electrode properties are limiting power density, and that further improvements are possible.

A stepped potentiostatic protocol was then applied between voltage limits of 2.5 V-1.6 V, as shown for the intermediate cycles in Fig. 2-11. This cycles the flow cathode into the precipitation regime, more than doubling the capacity compared to the solution regime. The step sequence was selected to provide approximately constant overpotential relative to the equilibrium cell voltage; more sophisticated feedback-based control algorithms that control overpotential are clearly possible. For the third complete charge/discharge cycle, the discharge capacity is 393 mAh/g, and coulombic and energetic efficiencies are 95.6% and 75.7%, respectively. Under this potentiostatic protocol, the net cycling rate for the entire system is C/15 on charge and C/22 on discharge. The cathode discharge energy density is 61 Wh/l (760 Wh/kg), and the cathode plus lithium energy density is 46.7 Wh/l (584 Wh/kg). Finally, the cell was cycled potentiostatically between the same voltage limits, but without intermediate potential steps. This increases the system-level C-rate to C/10 for charge and C/15 for discharge, and correspondingly, the capacity is slightly lower at 376 mAh/g in

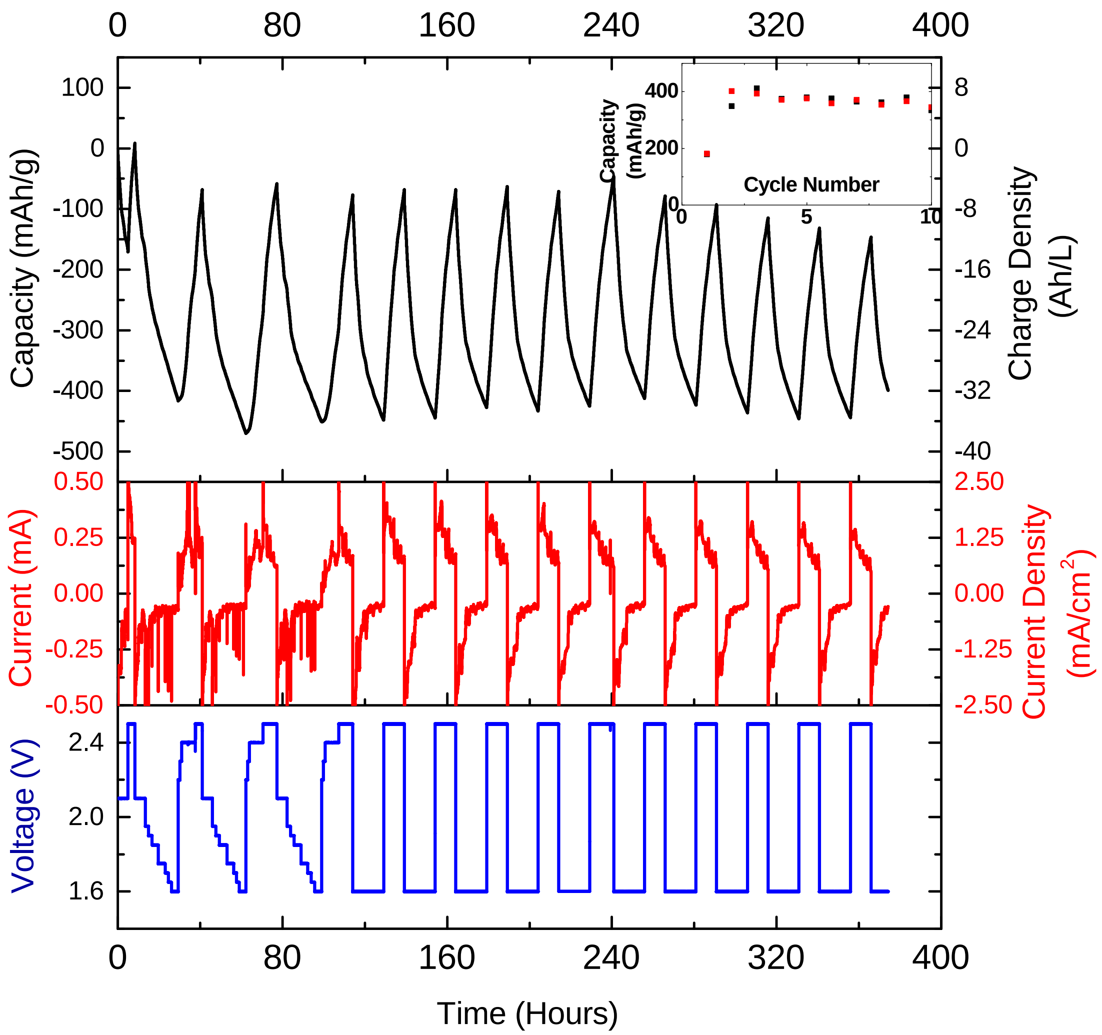

Figure 2-11: Continuous flow cell operation under potentiostatic cycling protocols, for nanoscale suspension electrode (2.5 mol S/L) in half-flow cell of Fig. 2-1b. Initial 1.5 cycles correspond to cycling over 2.5-2.1V, within polysulfide solution regime. Subsequent three cycles have stepped voltage protocol maintaining approximately constant overpotential over 2.5-1.6V, inducing Li_2S precipitation. Cycles 5-14 have potentiostatic holds at 2.5V upon charge and 1.6V upon discharge. Capacity vs. cycle number are shown in inset figure. Coulombic efficiencies averaged ∼99% throughout while energy efficiencies varied with protocol as discussed in text.

cycle 5, and energy efficiency decreases to 63%. The reduced energy efficiency is to be expected for this potentiostatic protocol due to the high overpotential relative to equilibrium cell voltage that is applied across most of the state of charge range. The active-materials-only discharge energy density is 44.1-48.1 Wh/l (552-602 Wh/kg). During cycles 5-14, despite some capacity fade as shown in the inset in Fig. 2-11, the coulombic efficiency remains above 99.5%. This suggests that impedance growth rather than loss of storage capacity in the flow cathode is responsible for the capacity fade. It would not be surprising for impedance growth to take place at the stationary Li metal negative electrode, given the large areal capacity that is reversibly plated throughout this experiment. Upon increasing charge time by ∼10% in cycle 15 (not shown), we found that the discharge capacity was restored, consistent with an impedance limitation.

Intermittent flow cycling was then demonstrated using the same cell geometry and nanocarbon suspension, with results appearing in Fig. 2-12. Optimization for efficiency in the intermittent flow protocol has been discussed in detail in recent work[52, 69]. A total of five cell volumes was flowed through the cell during a complete charge-discharge cycle, with each flow pulse having a volume that is one-half the cell volume (i.e., ten intermittent pumping pulses were used during each discharge and charge). Fluid-mechanical analysis suggests that the velocity profile in the flow cell is highly non-uniform, based on the suspension's rheology, pulse flow rate (30 μl/s), and channel design[69]. Accordingly, the volume of intermittent flow pulses was chosen to minimize the coulombic and energetic inefficiencies that are induced by flow non-uniformity. After each pumping step, the cell was galvanostatically discharged or charged, testing the solution and precipitation regimes with voltage limits of 2.55 V-1.95 V and 2.8 V-1.6 V, respectively. The capacity axis in Fig. 2-12 gives the specific capacity with respect to all sulfur in the system, assuming a uniform state-of-charge.

Fig. 2-12a shows the discharge-charge curve for the solution-only case, where the discharge and charge capacities are 162 mAh/g and 172 mAh/g, respectively, and the total discharge rate for the tank is C/5. The voltage-efficiency under these conditions (84 % at C/5) exceeds that of potentiostatic, continuous-flow cycling at lower effective

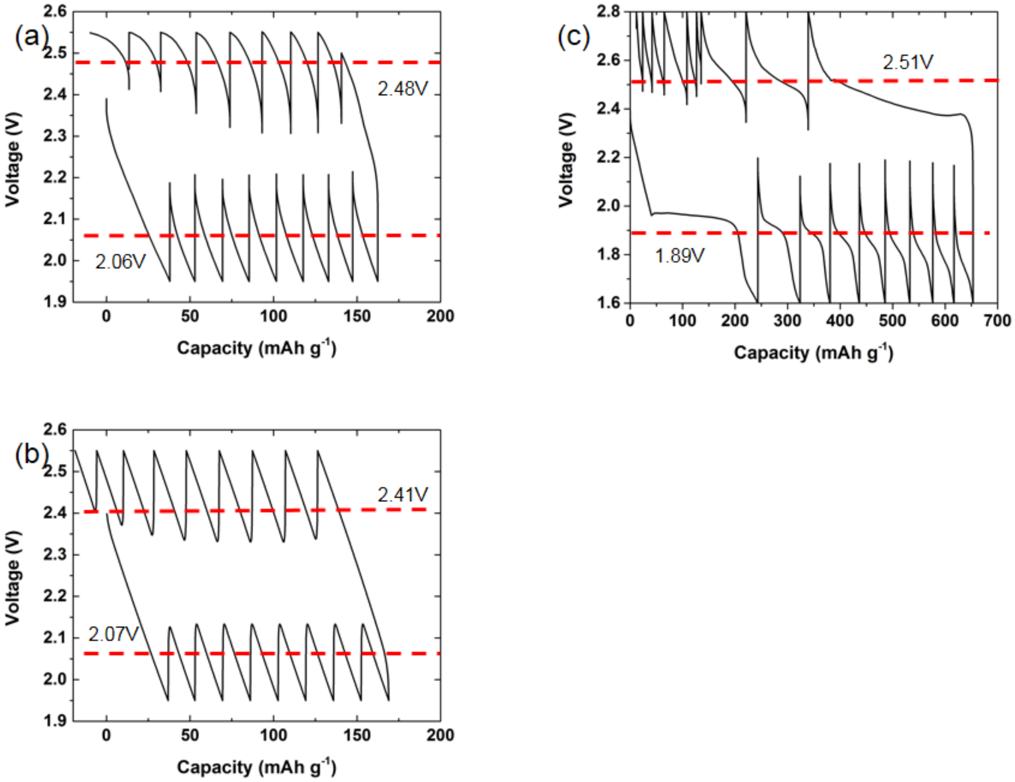

Figure 2-12: Intermittent flow cell operation with galvanostatic protocols, for nanoscale suspension electrode (2.5 mol S/l) in half-flow cell of Fig. 2-1b. Total volume pumped through cell is five times the cell internal volume (5:1 tank:stack ratio), and is pumped one-half of a cell volume per stroke. The capacity axis gives the specific capacity with respect to all sulfur in the system, assuming a uniform state-of-charge. (a) Galvanostatic discharge to 1.95V, and charge to 2.55V, to remain within polysulfide regime. Discharge rate is C/5 for total system. (b) Simulation of experiment in (a) using model described in Supplementary Information. (c) Galvanostatic discharge to 1.6V and charge to 2.55V, to include Li_2S precipitation with concommittent higher capacity. Net discharge rate is C/18. See text for discussion.

rate (78 % at ~C/10). This performance demonstrates the ability of the intermittent flow mode to cycle more efficiently than continuous flow. The simulated charge-discharge curve under these conditions is shown in Fig. 2-12b, following the model of Smith et al.[69]. The discharge voltage trends of the experiment and simulation agree well. An instantaneous jump in discharge voltage occurs after each intermittent flow pulse, because fresh suspension, rich in Li_2S_8, flows into the cell's electroactive region. The value of the voltage after the pulse (2.1-2.2 V) is substantially less than the open-circuit potential of the Li_2S_8 suspension (2.42 V). Voltage is reduced below this value because the electroactive region is incompletely replenished by the flow pulse[52, 69]. As a result, the solution phase of the suspension is more highly charged near the cell's inlet (nominally, Li_2S_8) than near the outlet (nominally, Li_2S_4). The average discharge voltage of the experiment (2.06 V) is in excellent agreement with the simulation (2.07 V), suggesting that Li-PS are locally in equilibrium during discharge, as assumed in the model. The experimental charge-voltage trends differ markedly from the idealized model, though, with a 70 mV deviation on average. While the simulation predicts linear variation of voltage with time after an intermittent pulse, the experiment exhibits sigmoidal variation of voltage. Recent *in operando* analyses of speciation in Li-S systems have suggested that charge and discharge processes in the Li-S system proceed through different reaction pathways[21]. The present deviation of experimental charge voltage from the simulation is consistent with these observations.

When the voltage window is widened to include precipitation, the discharge capacity is increased about four-fold to 653 mAh/g (Fig. 2-12c), with the discharge rate decreasing to C/18. These initial results demonstrate what we believe to be a higher efficiency alternative to continuous flow mode operation that reduces pumping losses, especially for higher energy density redox electrodes with substantial yield stresses and strongly shear-thinning rheology.

Cell performance at high polysulfide concentrations

To increase the energy density and reduce the cost of the system, the polysulfide concentration of the catholyte must be maximized. Non-flowing suspension cells with

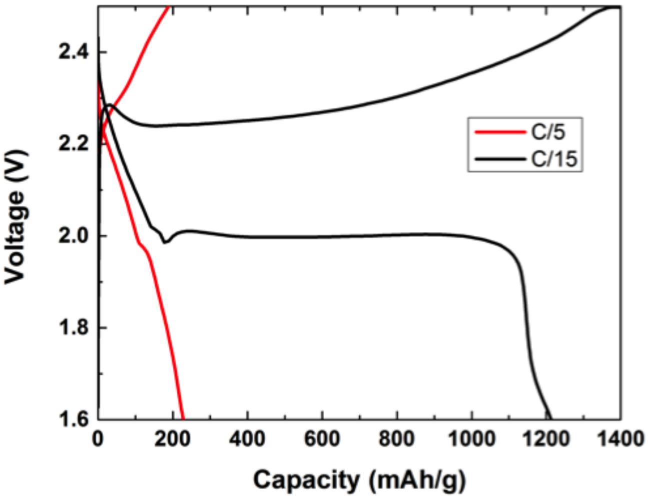

Figure 2-13: Charge-discharge curves for non-flowing suspension cells with 5M polysulfide concentration and 1.5 vol% KB.

5 mol S/l polysulfide solution were assembled and cycled at rates of C/5 and C/15, Fig. 2-13. At C/5, very little capacity (∼200 mAh/g) was observed, and the near-absence of a voltage plateau indicated that almost no Li_2S had precipitated. Also, polarization was high in the solution regime. However, at C/15, a high capacity (∼1200 mAh/g) was obtained, similar to that obtained using 2.5 mol S/l solution. Hence, the full capacity of the polysulfide is accessible at high concentrations, but rate capability is poor. The very low capacity in the precipitation regime in the C/5 case suggests that this process is especially slow. It is necessary to improve the kinetics of this process in order to achieve higher energy densities.

2.4 Conclusions

Thus we show that by using nanoscale conductor suspensions to form flowable electrically percolating networks, the electrochemical reactivity of solution-based redox electrodes can be greatly enhanced compared to that obtained with a conventional carbon fiber current collector. In addition, this novel flow electrode architecture allows redox solutions to be reversibly cycled into composition regimes where solid precipitation occurs. The nanoscale suspensions retain their electronic conductivity and enhanced reactivity under flow, and can be regarded as "self-healing." They may be used in flow cells that operate in continuous or intermittent flow modes. Just 1.5 vol% added nanoscale carbon allows Li-PS flow electrodes to operate in the precipitation regime where the specific energy and energy density increase by up to a factor of 5 compared to that obtained using only the solution regime. One of the great attractions of the Li-S system is the very low cost of the elemental reactants on an energy basis. For a reversible capacity of 600 mAh/g and average discharge voltage of 1.9V representing the present 2.5 mol S/l system, the raw materials cost of the flow cathode is $21/kWh, and that of the electrochemical couple (assuming 100% excess of Li metal) is only $37/kWh, leaving ample room for other component cost while meeting the $100/kWh target. We believe that with further development, higher capacity utilization in higher molarity solutions is achievable, which would further drive down the cost of storage. Such studies, which will be presented in later chapters, are applicable not only to flowing systems, but also non-flowing Li-S batteries. The nanoconductor suspension architecture can clearly also be used for anolytes, allowing a full flow battery as well as the half-flow system demonstrated here.

Chapter 3

Transport and Surface Kinetic Properties of Lithium Polysulfide Solutions

The contents of this chapter were published in Ref [70]. Exchange current density and ionic conductivity measurements were performed by Menghsuan Pan. Rheological characterization was performed by Ahmed Helal. Computational work was done by Kah Chun Lau and Rajeev Assary.

3.1 Introduction

A major obstacle for Li-S batteries is low rate capability, especially at low electrolyte/sulfur (E/S) ratios, which are required to realize the high energy density of the Li-S couple. While numerous computational models have been developed for lithium-sulfur batteries, such models require independent experimental measurements of the fundamental transport and kinetic properties [71, 72, 73]. In this chapter, we systematically investigate several potentially rate-limiting factors for lithium-sulfur batteries. In particular, we study the ionic conductivity of lithium polysulfide solutions of varying concentration and in different ether-based solvents and their exchange current density on glassy carbon working electrodes. This is the first such investigation of exchange current density for lithium polysulfide in solution of which we are aware. Exchange current densities are measured using both electrochemical impedance spectroscopy and steady-state galvanostatic polarization measurements. In the concentration range of interest (1-8 M [S]), the ionic conductivity monotonically decreases with increasing sulfur concentration while exchange current density shows a more complicated relationship to the total sulfur concentration. The electrolyte solvent is found to dramatically affect the solution ionic conductivity and exchange current density. The measured ionic conductivities and current densities are also used to interpret the overpotential and rate capability of polysulfide-nanocarbon suspensions; this analysis demonstrates that ionic conductivity is the rate-limiting property in the solution regime (i.e. between Li_2S_8 and Li_2S_4).

We elucidate the rate-limiting transport properties of Li-S cells cycling through the soluble regime and demonstrate that solvent selection largely determines the bulk ionic conductivity and exchange current density, thereby influencing the rate capability of the Li-S cell. We present a systematic experimental investigation of ionic conductivity and exchange current density of lithium polysulfide solutions in ether-based organic solvents commonly used in lithium-sulfur batteries. Exchange current density was measured using electrochemical impedance spectroscopy and galvanostatic polarization. The measured transport properties were used to perform a critical analysis to determine the rate limiting kinetic mechanisms for Li-S cells of different configurations.

Especially important are the measurements of the sulfur concentration dependence of the transport and kinetic properties of lithium polysulfides, because of the unique solution-mediated charge-discharge mechanism. The electrolyte/sulfur ratio of a Li-S battery has a significant effect on its cost and energy density[3]. As sulfur dissolves into the electrolyte during discharge, the sulfur concentration and thus the properties of the electrolyte change. The electrolyte/sulfur ratio effectively sets an upper bound on polysulfide dilution. A cell with 20 ml electrolyte/g S, for instance, would have an upper bound on polysulfide concentration of approximately 1.6 mol S/l. On the other hand, if there is only 2 ml electrolyte/g S, total dissolution of sul-

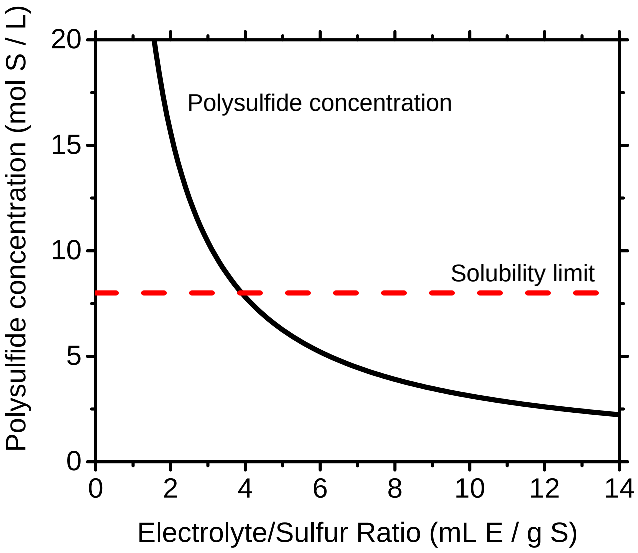

Figure 3-1: Polysulfide concentration in electrolyte if all sulfur is dissolved, vs electrolyte-sulfur ratio. Note that below a ratio of about 4 mL E/g S, the resulting polysulfide concentration exceeds the solubility limit. The concentration is calculated by dividing the molar mass of sulfur by the E/S ratio.

fur would result in approximately 16 mol S/l, which exceeds the polysulfide solubility limit (Fig. 3-1). Hence, we also investigated the effects of polysulfide concentration on exchange current density and ionic conductivity to understand the effects of high polysulfide concentrations that would occur in electrolyte-lean batteries. These concentration-dependent transport properties have remained poorly characterized to date; we anticipate that solution ionic conductivities will decrease with increasing sulfur concentration due to increased solution viscosity. Measurement and optimization of these transport properties is vital to the development of practical Li-S cells in the "lean" (low electrolyte/sulfur ratio) limit, where techno-economically viable cell designs are achievable.

Our experimental observations of solvent effects on exchange current density are in agreement with the results of first-principles simulations based on ab initio molecular dynamics (AIMD) simulations and static calculations.

3.2 Methods

Preparation of polysulfide solutions

Solutions are prepared as described in Chapter 2. To ensure the purity of lithium polysulfide solution, lithium sulfide (Alfa Aesar), sulfur (Alfa Aesar), and LiTFSI(Sigma-Aldrich) were dried under vacuum overnight at 100°C. Solvents (Sigma-Aldrich) were dried for at least one week using molecular sieves. Li_2S_6 solutions were prepared with various sulfur concentrations (1-8 M [S]) and different organic solvents by mixing lithium sulfide and sulfur into the solvent in a 1:5 mole ratio. 0.5 M of LiTFSI salt was also dissolved into the solution as the supporting electrolyte. The tested solvents are tetra (ethylene glycol) dimethyl ether (“tetraglyme”), tri (ethylene glycol) dimethyl ether (“triglyme”), di (ethylene glycol) dimethyl ether (“diglyme”), and 1,3-dioxolane:1,2 dimethoxyethane (DOL:DME 1:1). The resulting lithium polysulfide solutions were stirred overnight at 60°C to ensure homogeneity. Materials preparation, cell assembly, and exchange current density measurements were all performed in an Ar-filled glovebox with oxygen and moisture levels below 1ppm.

Exchange current density measurements

Exchange current density experiments were performed using a 3-electrode setup with a 3 mm glassy carbon working electrode 15 (BioAnalytic Systems, Inc) and separate lithium metal electrodes (Alfa Aesar) as reference and counter electrodes. Deactivation of the glassy carbon surface was found to be the main source of error, which was minimized through consistent cleaning and preparation of electrode surfaces. The glassy carbon electrodes were polished using 0.3 μm and 0.05 μm alumina powder and stored under Ar to prevent surface contamination and used within 24 h of polishing[74]. In EIS experiments, sinusoidal voltages of 5 mV, 10 mV, and 15 mV amplitude were swept logarithmically from 10 kHz to 0.1Hz between the working and counter electrodes. The three oscillation amplitudes were measured to verify linearity of the impedance response. The resulting impedance data (Fig. 3-2b) were fit to an

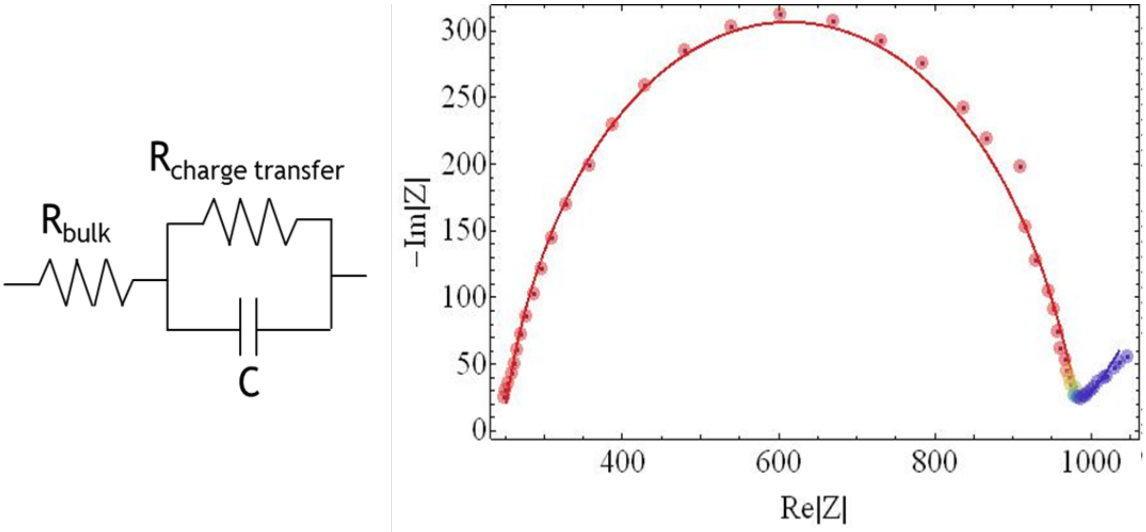

(a) (b)

Figure 3-2: (a) Equivalent circuit for modeling the three electrode cell. The bulk resistance accounts for the ionic resistance while the charge transfer resistance describes the rate of reaction on the current collector surface. (b) Impedance response for polysulfide redox in diglyme solution. The charge transfer resistance and the exchange current density are calculated from the width of the arc.

equivalent circuit with the bulk resistance in series with a parallel configuration of the charge-transfer resistance and a capacitor (Fig. 3-2a). Exchange current density j_0 is then calculated from the fitted charge-transfer resistance R_{ct} according to Equation 3.1.

$$j_0 = \frac{RT}{zR_{ct}FA} \tag{3.1}$$

In the galvanostatic polarization experiments, a selected constant current was applied for 15 minutes to ensure steady-state conditions were achieved. The average electrode potential over the 15 minutes steps determined the corresponding potential for the applied current. After the 15 minute polarization, the cell relaxed under open-circuit conditions and then the experiment was repeated at a new applied current. Both oxidative and reductive currents were applied. Throughout the experiments, the solution was vigorously stirred to avoid mass-transport limitation. The current density-potential pairs from Fig. 3-3a and b were used to construct the Tafel plot

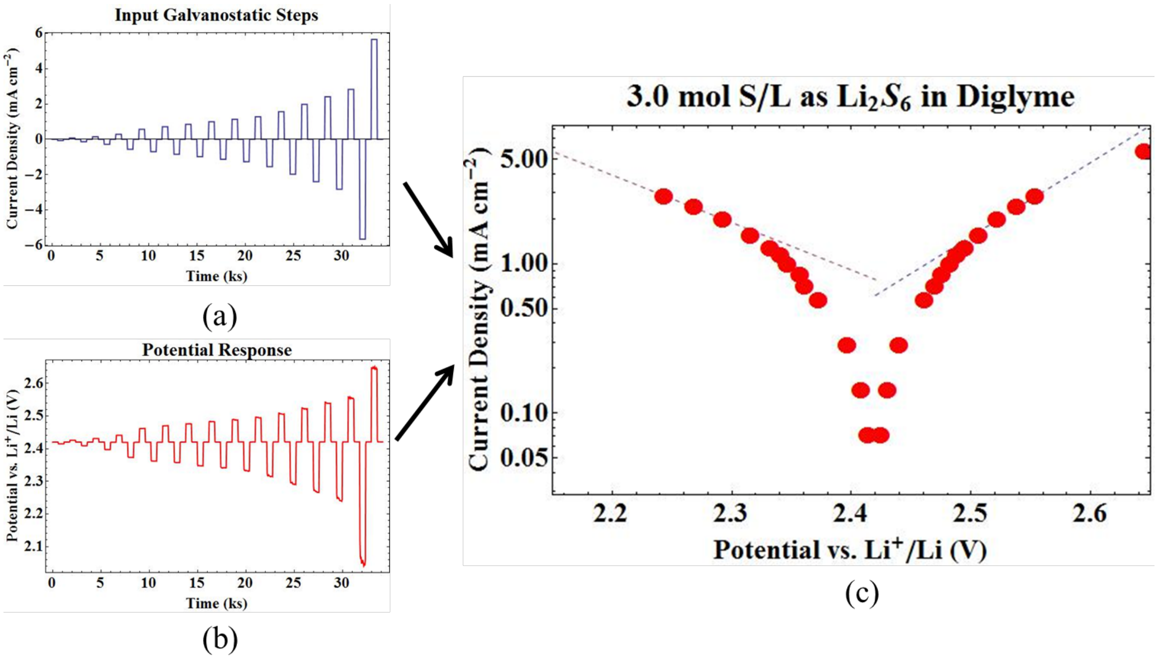

(a)

(b)

(c)

Figure 3-3: Galvanostatic polarization and resulting Tafel plot for 3.0 mol S/l Li_2S_6 in diglyme solution. The pairwise measured current step (a) and potential response (b) are used to obtain the Tafel plot (c). The semi-logarithmic linear regimes of the Tafel plots are extrapolated to the equilibrium potential to determine the exchange current density.

for a given formulation; an example Tafel Plot is shown in Fig. 3-3c. The semi-logarithmic linear region of the Tafel plot was manually fit and extrapolated back to zero overpotential to obtain the exchange current density according to the Butler-Volmer relation. All exchange current density measurements were performed using a Solartron 1470 potentiostat and 1455 Frequency Response Analyzer. The procedure for both EIS fitting and the Tafel extrapolation utilized Mathematica-based nonlinear least-square regression programs developed by our group.

Viscosity measurements

The viscometric behavior of the different solutions was measured using a Malvern Kinexus Pro torsional rheometer enclosed in an Argon glovebox with oxygen and moisture levels below 1 ppm. Steady shear viscometry tests were performed using a smooth stainless steel parallel plate geometry ($D = 40$ mm; mean roughness $R_a = 0.36$ μm). All tests were performed at $T = 25$°C and the temperature was regulated with a Peltier plate system. Steady shear tests were performed with decreasing applied shear rates. In addition, following the protocol proposed by Yoshimura and Prud'homme, the same sample was tested at three different gaps to probe and correct for slip effects[61]. The flow curves of solutions containing 2.5, 5 and 7 M sulfur as Li_2S_8 in TEGDME with 0.5 M LiTFSI supporting electrolyte exhibited Newtonian liquid behavior with constant viscosity and no slip at the wall.

Ionic conductivity measurements

Ionic conductivity of polysulfide solutions was measured using a Mettler Toledo FiveGo FG3 Portable Conductivity Meter calibrated with NIST-traceable aqueous solution standards. This measurement provides the total ionic conductivity of the solution.

Cell cycling

Suspension electrodes were prepared from polysulfide solution (with 0.15M $LiNO_3$ additive to reduce the effects of polysulfide shuttling) and carbon black (Ketjenblack EC-600JD), which were combined by manually stirring, followed by sonication for 1 h to form a percolating conductive network. This cathode architecture was used in order to access the solution regime directly without the need to undergo electrochemical sulfur dissolution. Cell cycling was performed in 2-electrode Swagelok cells controlled with a Bio-Logic VMP3 potentiostat. The suspension was placed inside a 0.5mm well in a stainless steel rod current collector sputter-coated with gold. A porous polymer separator (Tonen) wetted with polysulfide-free electrolyte was used to separate the polysulfide positive electrode from the lithium foil negative electrode.

Calculation

To compute the radial distribution function and coordination number of Li^+ for a solvated lithium polysulfide in various solvents, ab initio molecular dynamics calculations are performed using the VASP software[75, 76].18,19 All the calculations were spin-polarized and carried out using the gradient corrected exchange-correlation functional of PBE (Perdew, Burke, and Ernzerhof) under the projector augmented wave method, with plane wave basis set up to a kinetic energy cutoff of 300 eV[77, 78]. The van der Waals method of Grimme, DFT-D2 was used throughout AIMD calculations with the convergence criterion of the total energy set to be within 1 x 10^{-4} eV[79]. To compromise with high computational cost, we only focus on one particular salt concentration (i.e. 0.5 M LiTFSI) for these electrolytes (i.e. Diglyme, DOL:DME=1:1, TEGDME, DME) with 2.5 M S-concentration throughout this work. For the simulation of different electrolytes (i.e. Diglyme, DOL:DME=1:1, TEGDME, DME), the simulation box (17.76 x 17.76 x 17.76 Å^3) consisted of randomly populated about 20-40 solvent molecules and 1 salt molecules (i.e., LiTFSI) with a solvated Li_2S_8 molecule with presumed liquid density of 0.96 g cm^{-3}. To investigate the thermodynamic stability of the system at room temperature, all the system were thermally equilibrated at T = 300 K based on an Nose-Hoover thermostat within NVT thermodynamic ensemble with a time step of 1 fs, and the production run (∼3 ps) was obtained after thermal equilibration of ∼2.5 ps.

Static calculations using Gaussian 09 (Gaussian, Inc.) on model systems to are also performed to compute the free energy of binding of lithium polysulfides (Li_2S_6 and Li_2S_8) with solvent molecules, and vertical electron affinity. The B3LYP/6-31+G* level of theory was used to compute the structure, electronic energy, vibrational frequencies, and free energy corrections of all species.

3.3 Results

Exchange current density of polysulfide solutions

Both electrochemical impedance spectroscopy and galvanostatic polarization are used because in a high volatility solvent system, the shift in sulfur concentration due to solvent evaporation may cause the exchange current density to change during the more time-consuming galvanostatic polarization measurement. More specifically, we have observed precipation in high concentration diglyme solutions as well as noticeable evaporation in DOL:DME 1:1 solutions after overnight exposure to Ar-filled environment. Thus, for these solvent systems, the EIS-based measurements are the most reliable. For the less volatile solvents, the measurements can be compared with each other. In chapter 2, we demonstrated that there is good agreement between values obtained from these two methods, and both methods give similar results to steady-state voltammetry using an ultramicroelectrode[46].

The dependence of exchange current density on both sulfur concentration and choice of solvent is shown in Fig. 3-4. Exchange current density increases linearly with concentration in diglyme through most of the concentration range tested, but has negative concavity in triglyme and tetraglyme. Tetraglyme, in particular, has roughly constant exchange current density at concentrations above about 4M [S]. A positive correlation between concentration and exchange current density is to be

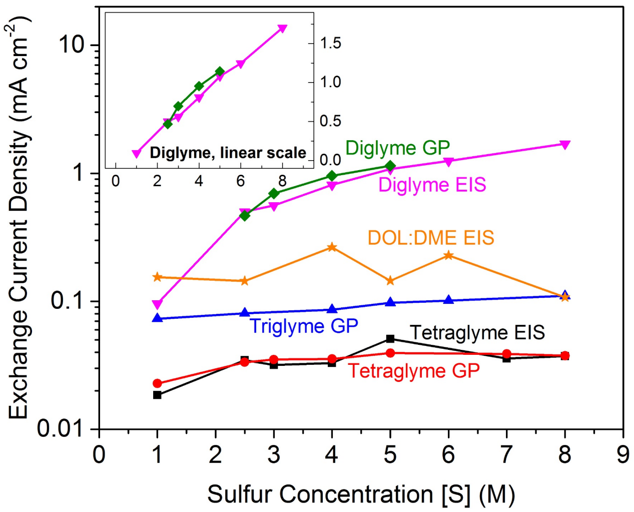

Figure 3-4: Exchange Current Density for Lithium Polysulfide (Li_2S_6) vs molar concentration of sulfur in difference ether-based solvent systems. Measurements for diglyme are also plotted in the inset to show the linear relationship between exchange current density and polysulfide concentration. Note: GP: Galvanostatic polarization, EIS: Electronic Impedance Spectroscopy

expected because of the higher concentration of species available for reaction at the interface. However, the observation that exchange current density does not increase linearly with concentration shows that the rate constant for redox reactions decreases with increasing concentration. We believe that this effect is due to ion pairing at the very high concentrations found in our solutions, especially in triglyme and tetraglyme which have fewer solvent molecules per unit volume. Also, exchange current density may be limited by the number of active sites on the carbon surfaces.

In the pure ether solvent (tetraglyme, triglyme, and diglyme) systems, exchange current density increases as solvent molecule size decreases across all the concentrations measured. On the other hand, the DOL:DME 1:1 system has exchange current densities lower than that of diglyme even though DME molecules are smaller than diglyme molecules. The presence of DOL causes deviation from the molecular size trend because of the different functional group, which is expected to influence solvation of the active ions and polysulfide species. The solvation mechanism is discussed in detail in the computation section. In the four solvent systems investigated, the exchange current density increases by more than 15-fold from tetraglyme to diglyme. Thus, solvent selection may be expected to play a large role in the rate capability of Li-S cells. Although this is a separate process from the nucleation and growth of Li_2S, we have also found (described in Chapter 4) an improvement in nucleation and growth rates when switching from tetraglyme to diglyme of a similar magnitude to the exchange current density improvement described here, suggesting that these processes may be limited by similar mechanisms[80].

Ionic conductivity of polysulfide solutions

In the sulfur concentration range of interest (1-8 M of sulfur), ionic conductivity decreases monotonically with increasing sulfur concentration in all of the presently measured solvent systems (Fig. 3-5). This is consistent with observations of ionic conductivity in other solvent systems such as tetrahydrofuran[81]. For any given solvent, there are two opposing trends in ionic conductivity associated with increasing solute concentration: the number of ions available in the solution and the mobility of individual ions. The former increases with polysulfide concentration, but the viscosity also increases significantly with polysulfide concentration. Ion mobility is expected to decrease with increasing viscosity (Stokes-Einstein relationship). Here, the decrease in mobility apparently outweighs the increase in charge carrier density resulting from a higher concentration of lithium and polysulfide ions, resulting in an overall decrease in ionic conductivity. Figure 3-5b shows that the ionic conductivity of tetraglyme solutions varies linearly with inverse viscosity for all solutions except the “0M” endmember which contains only salt and no polysulfide.

Note that the monotonic decrease of conductivity with polysulfide concentration may have significant implications for the performance of Li-S batteries with “lean” electrolyte/sulfur ratios. A low electrolyte/sulfur ratio increases polysulfide concentration in the electrolyte, and will reduce its ionic conductivity.

Comparing the ionic conductivity of the different solvent systems at any given sulfur concentration, the DOL:DME 1:1 system has the highest ionic conductivity, followed by diglyme, triglyme, and tetraglyme. All of the ethers used have the same

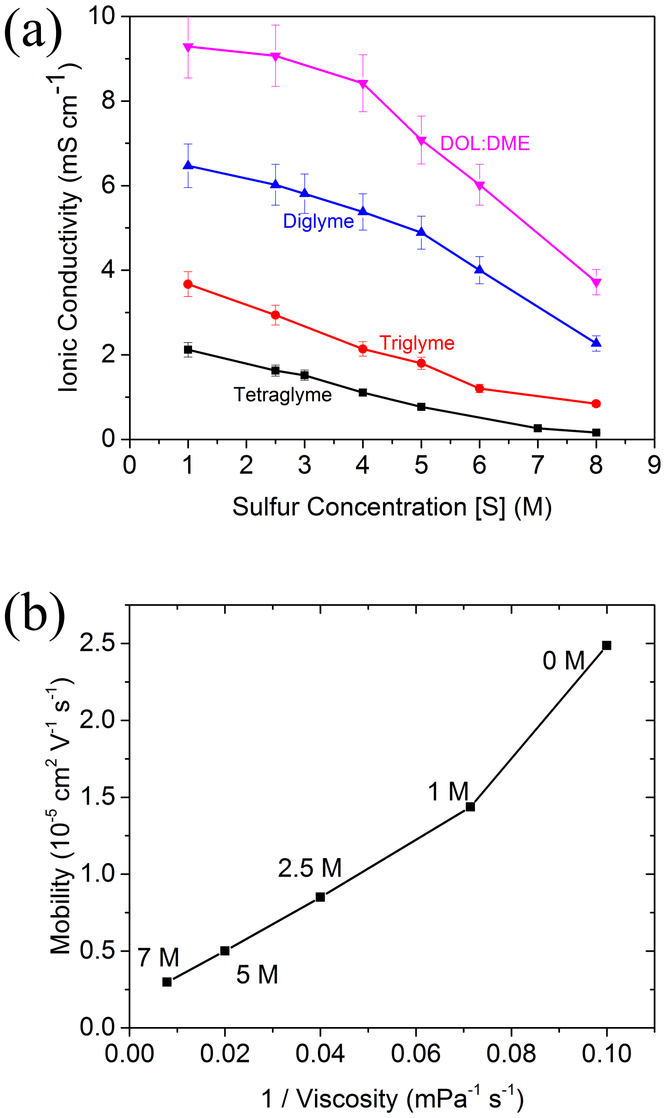

Figure 3-5: (a) Ionic conductivity of lithium polysulfide (Li_2S_6) vs. molar concentration of sulfur in different ether based solvent systems. All solutions contain 0.5M LiTFSI as supporting electrolyte contributing to the total ionic conductivity. (b) Mobility of various polysulfide solutions in tetraglyme vs. inverse of viscosity, showing linear slope consistent with the Stokes-Einstein relation except for the "0M" sample which contains supporting electrolyte salt and $LiNO_3$ additive, but no polysulfide.

functional group and differ only in the number of repeating units. The clear correlation is that ionic conductivity in the different solvents follows a trend of lower conductivity with longer solvent molecule. This finding is also consistent with the increasing viscosity with increasing ether chain length. At the higher polysulfide concentrations, the ionic conductivity is more than a factor of six higher for DOL:DME (1:1) than for tetraglyme. The ionic conductivity of Li_2S_8 measured earlier by our group also exhibits a similar trend with respect to sulfur concentration and solvent chain length as that of Li_2S_6 measured in this work[82]. We thus expect the ionic conductivity across different polysulfide species dissolved in non-aqueous solvents to follow the trend seen here. As with the exchange current density, the multifold variation in ionic conductivity across the solvent systems will impact rate capability, as shown next.

Cell capacity and rate capability

To determine the effects of solvent on rate capability, cells using lithium polysulfide suspension (2.5 mol S/l) electrodes were cycled at C-rates of C/2, C, and 2C (Fig. 3-6). Cells using tetraglyme had the worst rate capability and the most polarization, as expected from the fact that tetraglyme has both the lowest ionic conductivity and lowest exchange current density. At a rate of C/2, the diglyme cell had the least polarization in the solution regime. However, at a rate of 2C, DOL:DME had lower polarization, which we attribute to ionic conductivity becoming the limiting factor at higher C rates. The tetraglyme cells also had high polarization in the precipitation regime, which is due to the relatively sluggish Li_2S electrodeposition kinetics compared to other solvent systems. Despite the relatively low conductivity and exchange current density observed for longer chain solvents like triglyme and tetraglyme, their significantly lower vapor pressure may make them useful for some applications, such as high-temperature operation or flow batteries[46, 53, 83].

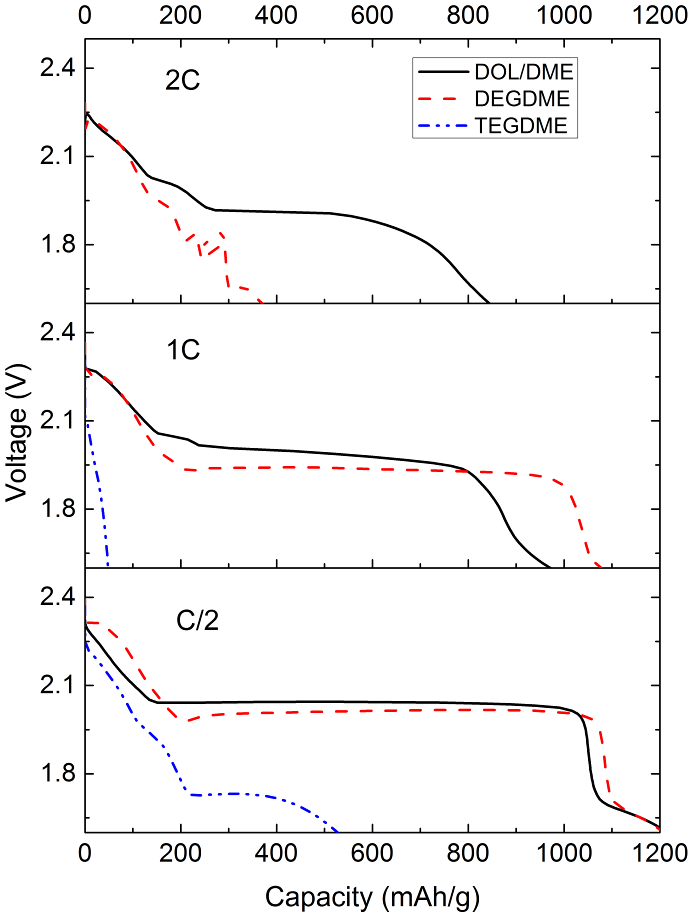

Figure 3-6: Voltage vs. capacity for first discharge of suspension-based Li polysulfide cells at various C-rates using tetraglyme, diglyme, and DOL:DME (1:1).

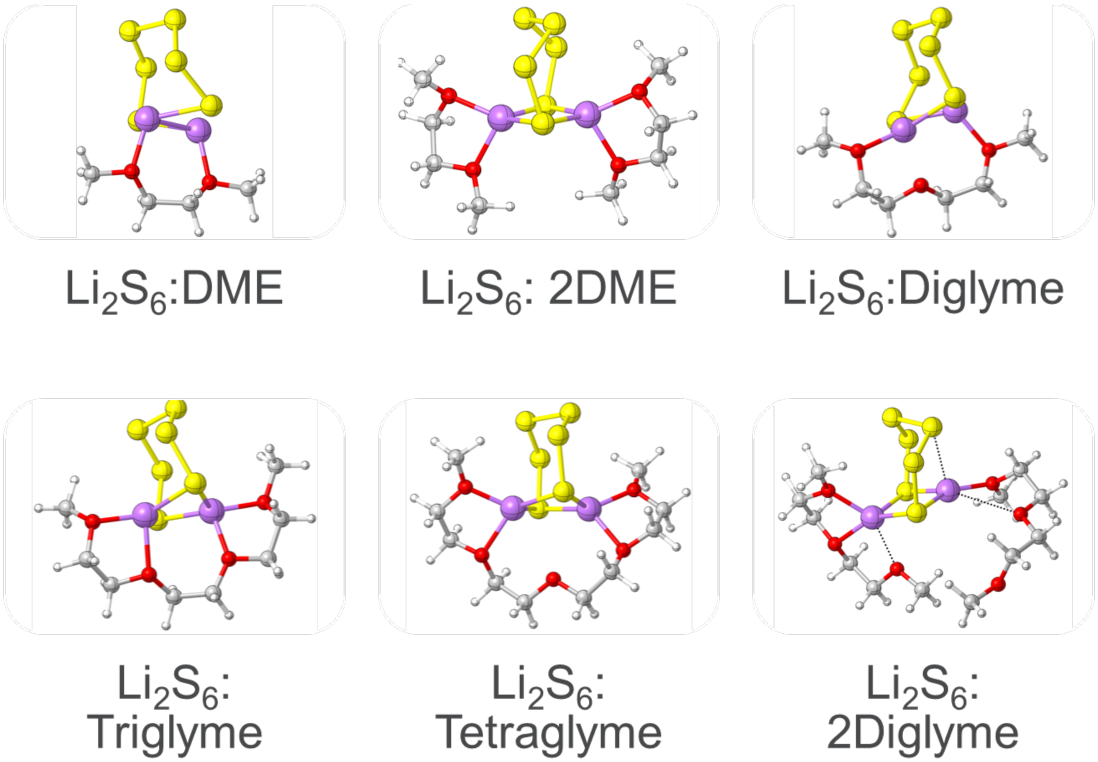

Figure 3-7: Optimized structures of selected Li_2S_6:Solvent complex computed at the B3LYP/6-31+G(d) level of theory.

Calculation

We found that diglyme binds to the lithium polysufide species (Li_2S_6 or Li_2S_8) relatively weakly compared to triglyme and tetraglyme (see fig. 3-7 for computed structures). A likely reason is that there are only three oxygen atoms available for coordination with cations compared to triglyme or tetraglyme, which have four and five respectively. AIMD simulations are performed to demonstrate this hypothesis and understand the solvation environment. Simulations are performed for Li_2S_8 in TEGDME, Diglyme, DME and DOL:DME (1:1) solvent environments. For instance, based on the computed radical distribution analysis (rdf) and coordination number shown in Fig. 3-8, a solvated Li_2S_8 species in diglyme has the lowest Li-O coordination number compared to DOL:DME (1:1) or TEGDME. The TEGDME solution has the highest Li-O coordination number in the first and second coordination shells. The assessment of radical distribution is confirmed by DFT calculations using cluster models. The computed Gibbs free energy of binding (298 K) of Li_2S_6 molecule with a clean glyme molecule in the gas phase is in the order: TEGDME (-23.7 kcal/mol)$>$ Triglyme (-22.2 kcal/mol)$>$ Diglyme (-12.2 kcal/mol). This trend is same for Li_2S_8 species (Table 3.1). Calculations are performed by including two diglyme molecules to provide an adequate number of oxygen atoms (four or more); however, the Gibbs free energy of binding (-12.5 kcal/mol) is similar, due to entropic contributions. Thus, computations suggest that the degrees of solvation of lithium polysulfides in various glymes are different. Relatively weaker binding of diglyme with the Li_2S_6 may allow the species to interact with other polysulfides that are in equilibrium or with the electrode surface. Since the exchange current densities reflect intrinsic rates of electron transfer between the lithium polysulfides (LiPS) and the electrode, we have computed the vertical electron affinity (EAe) of the Li_2S_6:glyme complex (Table 3.1) in the gas phase (B3LYP/6-31+G* level of theory) to provide a qualitative uunderstanding. They are in the order of: diglyme (+7.4 kcal/mol) $>$ triglyme (+4.9 kcal/mol) $>$ tetraglyme (+2.8 kcal/mol). This trend is consistent with the order observed in the measurement of exchange current density.

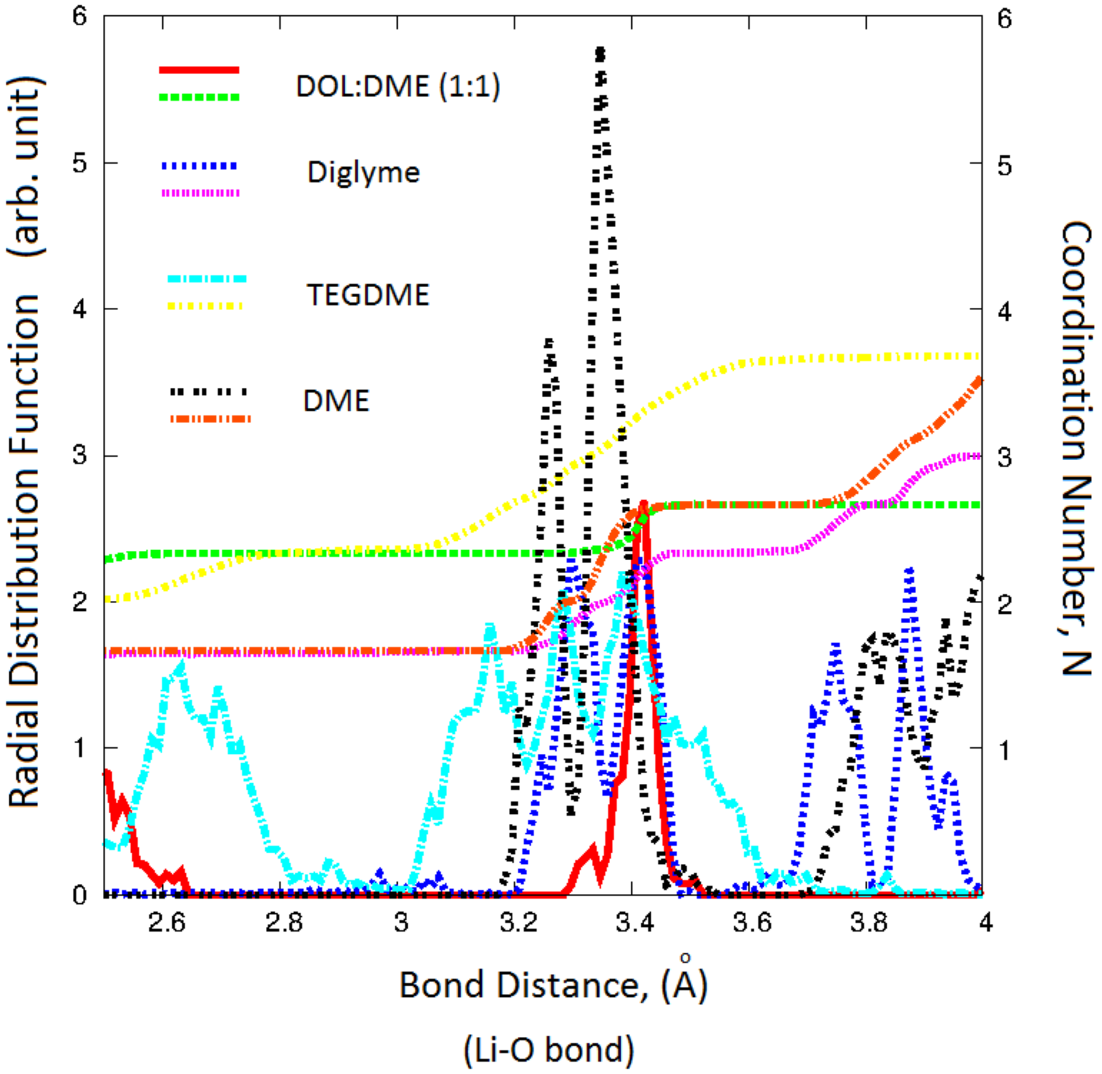

Figure 3-8: Computed radial distribution functions (RDF, top lines in legend) and coordination number (bottom lines) of solvated Li^+ from Li_2S_8 for bonds between Li^+ ions and O atoms in different solvent molecules from ab initio molecular dynamics (AIMD) simulations.

(Solvent)$_n$-Li_2S_6	ΔG(298K)	ΔH(298K)	EA of (Solvent)$_n$-Li_2S_6 (eV)
1-DME	-3.6	-16.2	-0.37
4-DOL	-4.2 (-4.7)	-47.5	
2-DOL:1-DME	-11.8	-45.2	-0.20
1-Diglyme	-12.2 (-13.6)	-26.5	-0.32
2-Diglyme	-12.5	-37.9	-0.18
2-DME	-17.3 (-18.4)	-38.9	-0.20
1-Triglyme	-22.2 (-22.6)	-38.6	-0.21
1-TEGDME	-23.7 (-21.3)	-41.9	-0.12

Table 3.1: Computed gas phase free energies and enthalpies for the binding of Li_2S_6 with solvent molecules at the B3LYP/6-31+G* level of theory. Also shown is the computed Electron Affinity (EA) of the Li_2S_6-Solvent complex. Values in parentheses are corresponding binding energies for Li_2S_8 molecule

3.4 Conclusions

A systematic study of the effects of solvent choice and polysulfide concentration on exchange current density and ionic conductivity in lithium polysulfide solutions was performed for the first time. In any given solvent system, reaction rate constant and ionic conductivity are highest at low polysulfide concentrations, i.e. at high electrolyte/sulfur ratios. The choice of solvent significantly affects the kinetics and the rate capability of lithium-sulfur batteries. Within the glyme family of solvents, a decrease in the molecular weight of the solvent was found to increase significantly both exchange current density and ionic conductivity at a given polysulfide concentration. Significantly higher exchange current density was observed in diglyme than in the most widely reported solvent system, DOL:DME. However, DOL:DME solutions had higher ionic conductivity than diglyme solutions. Although this resulted in lower polarization and higher rate capability for DOL:DME electrolytes in our test cells, other aspects of cell design, such as electrode thickness and the type and amount of conductive additive, will also play an important role in determining cycling performance. Diglyme may prove to be a superior choice under certain situations, such as when carbon surface area is limited and a higher exchange current density is beneficial, or where electrode thickness or tortuosity are low and ionic conductivity is less likely to be limiting. Tuning of kinetic parameters, ionic conductivity and exchange current density through careful electrolyte formulation design can significantly improve the rate capability of the lithium polysulfide solution, which is an important step toward realizing the potential low cost and high energy of the Li-S couple.

Chapter 4

Mechanism and Kinetics of Li_2S Electrodeposition in Li-S Batteries

4.1 Introduction

The overwhelming majority of the theoretical capacity of a Li-S cell results from the reduction of soluble Li_2S_4 to insoluble Li_2S via an electrodeposition process, a process that is often kinetically sluggish. The existence of Li_2S itself poses a challenge, due to the fact that it is an electronic insulator. It is therefore surprising that despite nearly 30 years of research and development, the fundamental mechanism and kinetics of Li_2S growth have not previously been elucidated. This stands in stark contrast to lithium peroxide formation at the cathode in Li-O_2 batteries, where the kinetics and morphology have been widely studied in recent years [35, 36].

In this chapter, we extend our analysis of rate limitations in Li-S batteries to the Li_2S precipitation regime and characterize the kinetics and morphology of Li_2S electrodeposited from nonaqueous (glyme-based) polysulfide solutions onto carbon fibers and multi-walled nanotubes (MWCNT). Deposition is studied under potentiostatic conditions as a function of overpotential, and galvanostatic conditions as a function of current rate. The deposition mechanism is determined from a combination of kinetic analyses and direct observations of Li_2S morphology at various stages of deposition by electron microscopy. It is shown that the morphology of electrodeposited Li_2S

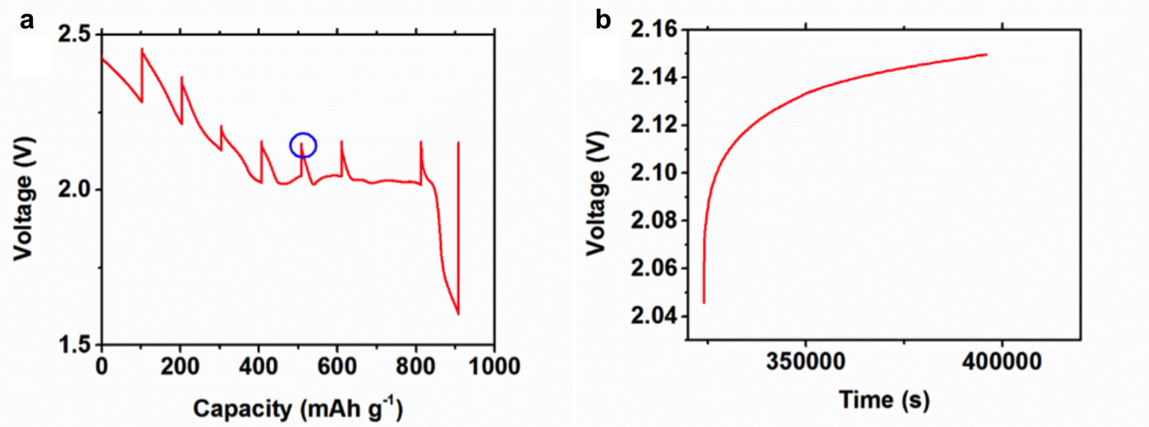

Figure 4-1: (a) Galvanostatic intermittent titration technique (GITT) curve for a dissolved polysulfide/MWCNT suspension electrode (3 vol% MWCNT in 2.5M S (as Li_2S_8) solution in tetraglyme). Current steps were performed at C/24 rate, followed by 20h relaxation steps, at which point dV/dt is approximately 1mV/h. The relaxation step at the beginning of the precipitation plateau (b), circled in blue in (a) was used to determine the equilibrium potential, which is 2.150V.

depends on the nucleation density and relative rates of nucleation vs. growth, each of which can be manipulated by controlling the overpotential, the characteristics of the substrate, and the choice of solvent. Guidelines for optimizing storage capacity through substrate choice and electrokinetic control are presented.

4.2 Methods

In potentiostatic experiments the potential is held below the equilibrium potential (determined to be 2.15V for the present cells, see Fig. 4-1) to provide a constant driving force (i.e. overpotential), and the time evolution of sulfur species reduction is monitored via current flow. Starting solutions consisted of Li_2S_8 as the sulfur source, dissolved in di-, tri- or tetraglyme solvent with 0.5M bis(trifluoromethane) sulfonimide lithium salt (LiTFSI) as a supporting salt, and 0.15M $LiNO_3$ as an additive to reduce the effect of the shuttle mechanism[28]. Ether solvents (usually glymes) are typically used in electrolytes in lithium sulfur batteries[65, 84]. Graphite fiber felt (SGL Group, Wiesbaden, Germany) with fiber diameter 9μm was used as a working electrode and lithium foil as the counter electrode, and the components were assembled in two-electrode Swagelok®-type cells (Fig. 2-2) with a porous polymer separator (Tonen Chemical Corporation, Tokyo, Japan) separating the working and counter electrodes. Several polysulfide species can simultaneously exist in equilibrium in the electrolyte and undergo reduction as a Li-S cell is discharged[21, 85]. In order to distinguish the electrodeposition of Li_2S from Li_2S_4 from the reduction of higher-order polysulfides (Li_2S_8 and Li_2S_6) in solution, each cell was first discharged galvanostatically to a potential of 2.05V at a rate of C/24. Subsequently, reduction was carried out at a fixed potential selected from the range between 1.95V and 2.06V (vs. Li/Li^+).

These potentiostatic experiments are analogous to phase transformations at constant temperature (in which the thermodynamic driving force is also fixed). Such transformations can be modeled by the Avrami equation (4.1), in which nucleation and growth rates are assumed to be constant with respect to time:

$$Y = 1 - e^{Bt^n} \tag{4.1}$$

where Y is the fraction of the material that has been transformed, B is a kinetic constant, and n is the Avrami exponent. Both B and n are related to the dimensionality of growth and whether nucleation is instantaneous (i.e. all nuclei form at the beginning of the process) or continuous (i.e. nuclei form at a constant rate throughout the process) [40, 86]. In general, n is equal to the dimensionality plus zero (for instantaneous growth) or one (for continuous growth). For example, for 2-D growth with progressive nucleation, $n = 3$ and

$$B = \left(\frac{\pi}{3}\right) A k^2 \tag{4.2}$$

where A is the nucleation rate (nuclei per unit area, per unit time) and k is the lateral growth rate of nuclei, in velocity units. Equation 4.1 can be rearranged as follows:

$$ln[-ln(1 - Y(t))] = lnB + nln(t) \tag{4.3}$$

To obtain the value of n, one need only plot $ln[-ln(1 - Y(t))]$ vs. $ln(t)$ and find the slope. The Avrami equation can be extended to electrochemically driven phase transformations, such as electrodeposition, effects first described by Thirsk and co-workers[45, 44]. Since the associated current represents the rate of change of the electrodeposited phase, it is proportional to the time derivative of the Avrami equation:

$$\dot{Y} = -exp(-Bt^n)(-nBt^{n-1}) \tag{4.4}$$

The current increases initially as nuclei form and grow quickly and peaks as the resulting islands start impinging. In the case of 2D growth and progressive nucleation, the time corresponding to peak current in the potentiostatic curves, t_m, can be obtained from Equations 4.4 and 4.2[45]:

$$t_m = \Big(\frac{2}{\pi A k^2}\Big)^{1/3} \tag{4.5}$$

Therefore, the combined nucleation and growth rate constant Ak^2 can be determined directly from the location of the potentiostatic current peak. Combining Equations 4.4 and 4.5 yields Equation 4.6, which is used to fit the current peaks, along with a background which is the sum of two exponential functions, and results from nonfaradaic double-layer charging and the reduction of higher order polysulfides.:

$$\frac{I}{I_m} = \frac{t}{t_m}^{2} exp\Big[-\frac{2}{3}\Big(\frac{t^3 - t_m^3}{t_m^3}\Big)\Big] \tag{4.6}$$

where I is the current and I_m is the maximum current. In cases of experiments, typically with small overpotentials, in which there is a long incubation period, we modify this equation with the parameter b (Equation 4.7) to indicate that the peak does not begin at time zero.

$$\frac{I}{I_m} = \Big(\frac{t - b^2}{t_m}\Big) exp\Big[-\frac{2}{3}\Big(\frac{(t-b)^3 - t_m^3}{t_m^3}\Big)\Big] \tag{4.7}$$

Electrodeposition experiments were performed in modified 2-electrode Swagelok® cells. A 1.95 mg disk of carbon fiber felt (GFD 3, SGL Group) with fiber surface area of 4.3 cm^2 was used as a working electrode and placed in a 0.5 mm-deep well in a Au-coated stainless steel rod current collector. Lithium foil (Alfa Aesar) was used as a counter/reference electrode, and a porous polymer separator (Tonen) soaked in electrolyte (without polysulfide) was used to separate the electrodes. Galvanostatic cycling of suspension electrodes was performed in the same type of Swagelok cell, the suspension placed in Au-coated stainless steel current collectors. Electrochemical experiments were performed using a Bio-Logic VMP3 potentiostat.

Polysulfide (Li_2S_8) solution was prepared by stirring stoichiometric amounts of lithium sulfide and sulfur (Alfa Aesar, Ward Hill, MA, USA) in tetraglyme (Alfa Aesar), triglyme, or diglyme (Sigma-Aldrich, St. Louis, MO, USA) at 60 °C for 24h, along with 0.5M LiTFSI supporting electrolyte and 0.15M $LiNO_3$ additive (both Sigma-Aldrich). Electrolyte for wetting separators was prepared by adding 0.5M LiTFSI and 0.15M $LiNO_3$ to the appropriate solvent and stirring until completely dissolved. All solvents were dried on molecular sieves for at least seven days. The water content of the solvents was determined using Karl Fischer titration to be less than 10 ppm. To make a suspension electrode for galvanostatic cycling tests, multiwall carbon nanotubes (Nanoscale & Amorphous Materials, Inc., Houston, TX, USA) were stirred into polysulfide solution, which was then sonicated to disperse the nanotubes. Preparation of solutions and cell assembly was performed in an Ar-filled glovebox (MBraun, Newburyport, MA, USA) with water and oxygen levels maintained below 1ppm. Solid precursors, cell parts, and carbon electrodes were dried by heating under vacuum at 100 °C.

Scanning electron microscopy was performed using a Zeiss Merlin high-resolution SEM with in-lens secondary electron detector. Transmission electron microscopy was performed using an FEI Tecnai G2 Spirit TWIN TEM.

4.3 Results and Discussion

The time-dependence of reduction current followed a characteristic curve for all experiments in which electrodeposition of Li_2S occurred, as shown in Fig. 4-2. An initial “incubation” period of monotonically decreasing current is observed, which we attribute to the reduction of remaining higher-order polysulfides in solution to Li_2S_4. This regime is followed by a current peak which, as we show, is due to nucleation of solid Li_2S followed by either growth to impingement, whereupon the reaction practically ceases[87]. We observed that a critical value of the overpotential is necessary to nucleate Li_2S onto carbon; this overpotential is 0.10V (i.e., absolute cell voltage of 2.05V or lower) for nucleation from all three glyme electrolytes. Fig. fig:filledfitsa shows the current- vs. time curve at 2.06V in tetraglyme, just 10 mV above the critical potential. The current decreases monotonically and can be fit as the superposition of two exponential functions, which we treat as the superposition of the reduction curves for Li_2S_8 and Li_2S_6 in solution. This interpretation is supported by the following analysis. At 2.05V and 2.04V in tetraglyme, where this incubation period can be clearly distinguished from the current peak, the capacity under the integrated curve plus that accumulated during the initial galvanostatic reduction sums to 200 mAh g^{-1} S, which is close to the theoretical capacity resulting from the complete reduction of Li_2S_8 to Li_2S_4.

Next, considering the current peak observed at cell voltages of 2.05 or lower, a kinetic analysis following phase transformation theory reveals behavior characteristic of a 2D island nucleation and growth process[87, 45]. The sum of two exponential functions was first used as a fit for the background for the current vs. time curve, subtraction of which isolates the peaks (Fig. 4-4). The current peak in Fig. 4-2a has a sigmoidal cumulative distribution function (Fig. 4-2b) that follows the Avrami form (Equation 4.1) [40].

The dimensionality and deposit morphology inferred from the kinetic analysis was confirmed by direct imaging using scanning electron microscopy. In Fig. 4-3a, the potentiostatic deposition curve measured at 2.02V (130 mV overpotential) is shown, along with an image of the pristine carbon fiber. The current-time data was fitted to Equation 4.6 (essentially the derivative of the Avrami equation, adapted to electrodepostion). Fig. 4-3b-d shows the Li_2S precipitate morphology at times of 2.5h, 4h, and 6h, respectively, as well as surface coverage predicted by integrating the fitted peak.

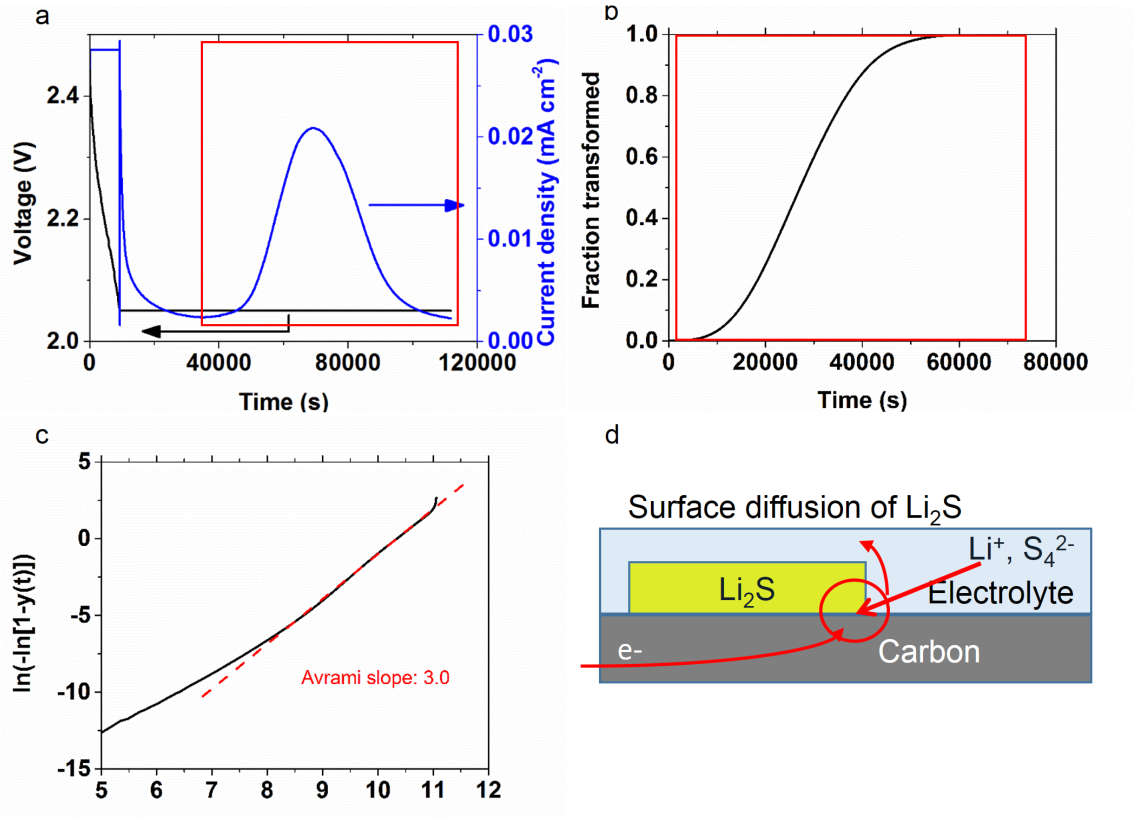

Figure 4-2: (a) Voltage and current vs. time for a polysulfide-porous carbon cell, which was first galvanostatically discharged to 2.05V, then potentiostatically discharged at 2.05V. (b) Transformation vs. time plot for potentiostatic current peak (enclosed in red in (a)). (c) Avrami plot resulting from the boxed portion of (b). (d) Proposed mechanism for the reduction of polysulfides at the 3-phase boundary between carbon, Li_2S, and electrolyte

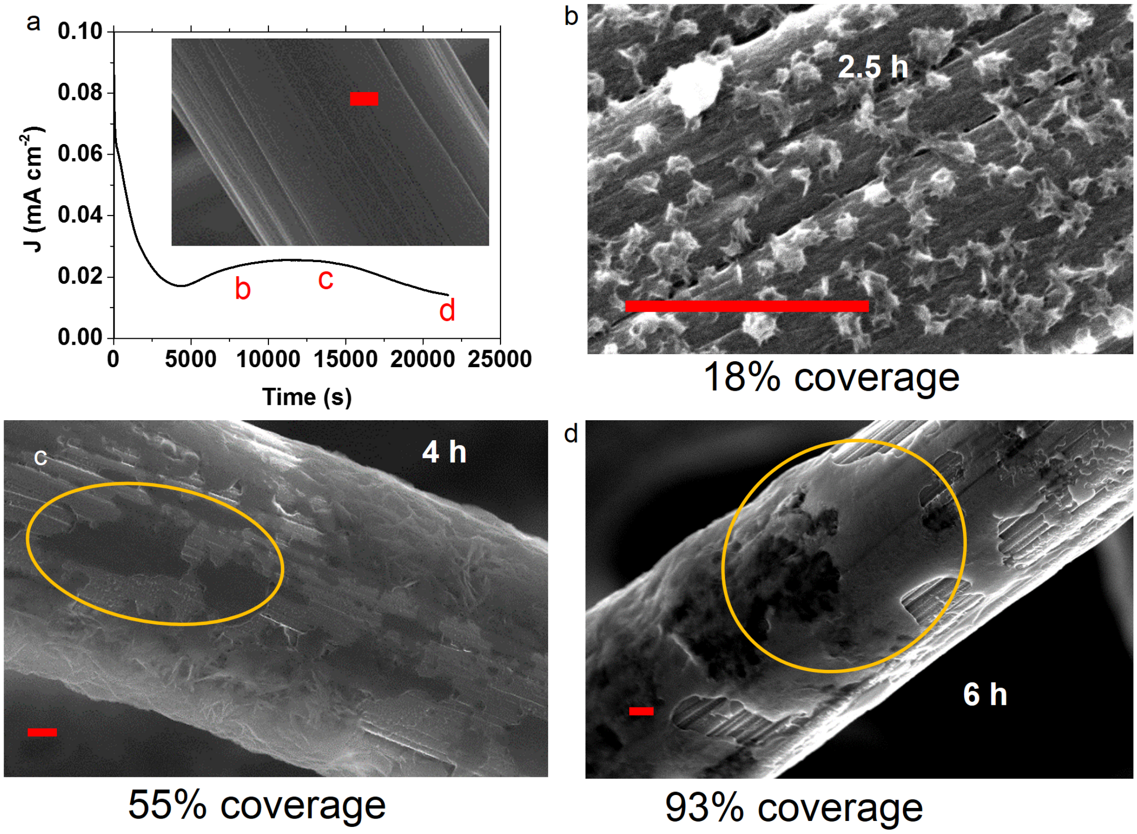

Figure 4-3: (a) Current vs. time for potentiostatic discharge at 2.02V. Positions of images for (b)-(d) are labeled on the plot. Inset: SEM image of pristine carbon fiber. (b)-(d) SEM images after (b) 2.5h, (c) 4h, and (d) 6h. All scale bars are 1μm.

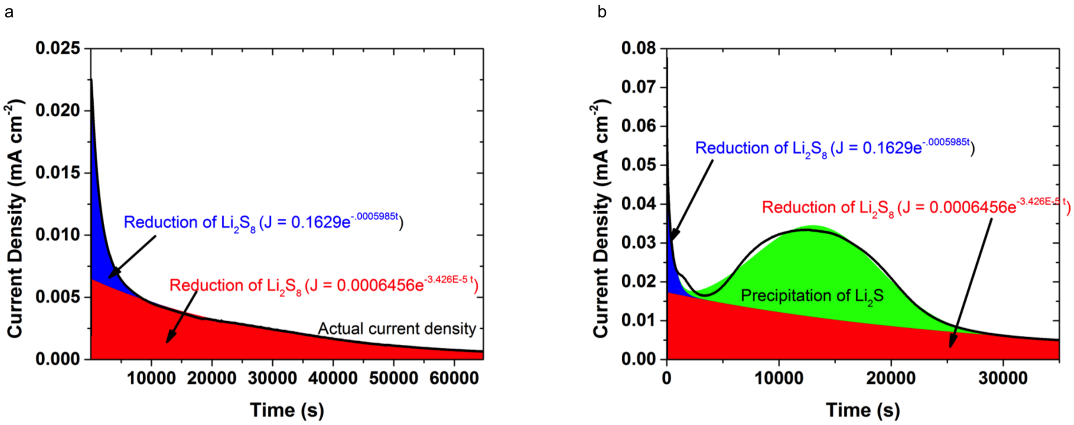

Figure 4-4: Fitting of chronoamperometric data for reduction of polysulfides at (a) 2.06V vs. Li^+/Li showing only current resulting from reduction of higher order polysulfides to lower order polysulfides and (b) at 2.02V, with a peak resulting from nucleation and growth of Li_2S.

At 2.5h, corresponding to a calculated 18% surface coverage according to the Avrami analysis, a relatively sparse covering by small islands is observed. At 4h, corresponding to calculated coverage of 55%, these islands have begun to coalesce, forming a thin 2D film on the fiber surface. The observed impingement of islands is consistent with the fact that at this time the current density has peaked; i.e., impingement has reduced the surface area available for continued lateral growth of the islands. At 6h, corresponding to calculated coverage of 93%, the film is indeed observed to have almost completely covered the surface of the electrode, and the current has decayed considerably. The average deposit thickness of the sample pictured in Fig. 4-3d, measured from SEM images, was found to be approximately 500nm when adjusted for areas of the fiber not covered by the deposit. This is less than, but close to, the average thickness of 710nm predicted by the 0.15mAh cm^{-2} of capacity related to Li_2S_4 reduction in the plot given in Fig. 4-3a. Additional potentiostatic curves under other overpotentials and for the three glymes tested appear in Fig. 4-5. It is clear that after growth to impingement, the current asymptotically approaches zero and deposition of Li_2S practically ceases.

Based on the above morphological and kinetic observations, we propose a mechanism for Li_2S growth, illustrated in Fig. 4-2d. We believe that the long-time limiting behavior of vanishing current is due to the electronically insulating nature of the Li_2S precipitate. Yang et al. estimated an electronic resistivity of over 10^{14} Ω cm for Li_2S,[88] according to which the peak current density of 0.02 mA cm^{-2} in the potentiostatic experiment at 2.05V would produce a polarization of 20kV in a 100 nm thick film. Clearly the electronic conductivity is not sufficient to permit growth at the outer surface of the Li_2S, given that growth occurs at $\sim$2V. Instead, we conclude that growth occurs by reduction of the polysulfide from solution at the three-phase boundary between the existing Li_2S precipitate, electronically conductive substrate, and solution phase. During nucleation and growth, the length of three-phase boundary reaches a maximum, and disappears when the precipitates have fully impinged. Growth in the thickness direction cannot occur via bulk chemical diffusion through the Li_2S layer, due to the conductivity limitation. We believe that thickness growth occurs

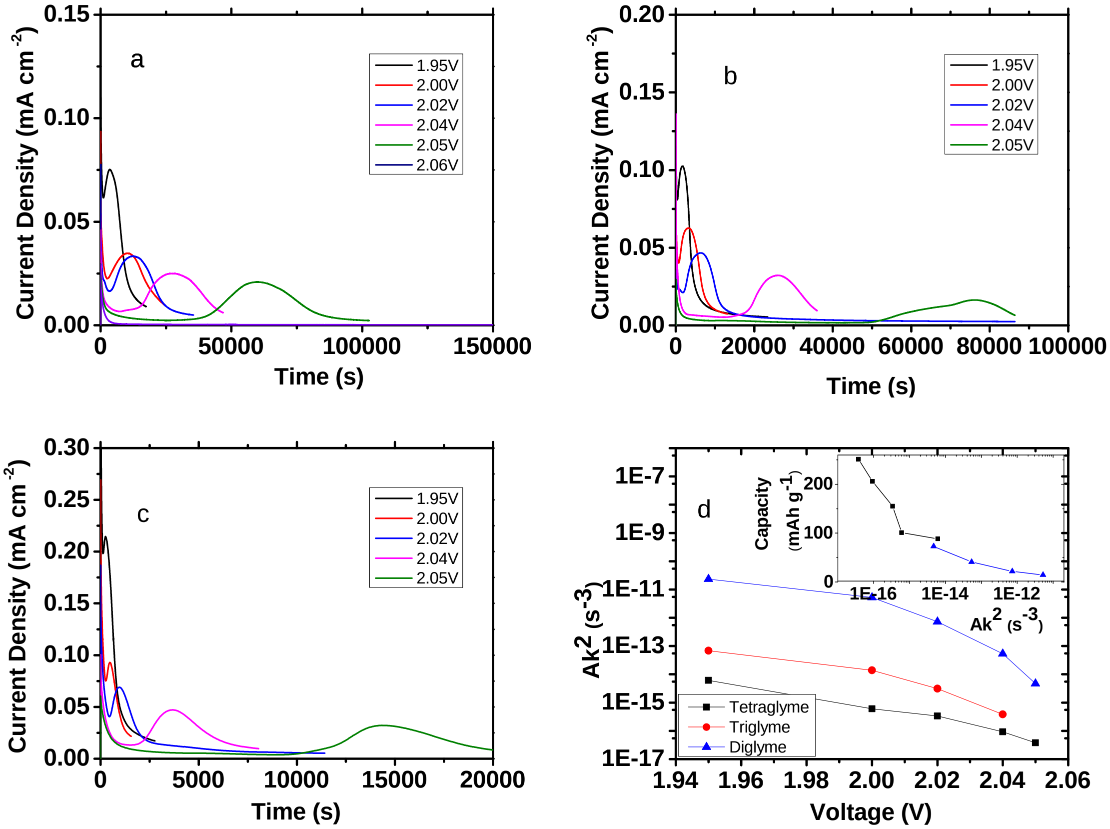

Figure 4-5: (a)-(c) Current-time plots for potentiostatic discharge in various solvents: (a) Tetraglyme, (b) Triglyme, (c) Diglyme. (d) Combined nucleation-growth rate constants resulting from fitting of current peaks. Inset: Deposition capacity vs. rate constant for diglyme and tetraglyme

via surface diffusion at the Li_2S-electrolyte interface; as shown later by galvanostatic experiments, the thickness of Li_2S is dependent on the total growth time available. Note that for electrodeposited materials that are not electronic conductivity limited, such as aluminum, the current instead increases monotonically and asymptotically approaches a maximum value, assuming no diffusion limitation[44, 41].

For the kinetic analysis to apply, the Li_2S chemical transformation must be limited by surface reaction kinetics and not by the supply of sulfur, or by mass transport to the growth interface. (Note that this need not be the case for a practical Li-S battery; the carbon fiber electrode in this experiment was deliberately chosen for its limited surface area.) The supply of sulfur in the experiment is not limiting, since the total potentiostatic capacity is a fraction of the theoretical sulfur capacity (e.g. in Fig. 4-2a it is approximately 300 mAh/g S, or one-fourth the theoretical capacity for reduction of Li_2S_4 to Li_2S). To test whether mass transport could be limiting, we conducted steady state voltammetry at a carbon fiber ultramicroelectrode (Fig. 2-9) and obtained an Li_2S_8 diffusivity of $2\text{x}10^{-7}\text{cm}^2\text{s}^{-1}$, corresponding to a diffusion length of over 1mm during the course of a 60,000s experiment. Given that the spacing between fibers in the electrode is 20μm (Fig. 2-6), mass transport of polysulfide to the deposition sites cannot be limiting.

For a nucleation and growth mechanism, whether the driving force is thermal or electrochemical (undercooling and overpotential being analogous driving forces), nucleation requires a higher driving force than does growth, since surface energy barriers must be overcome. A lower energy barrier for growth than for nucleation is expected in electrodeposition, and has been observed for the precipitation of Li_2O_2 in lithium-oxygen batteries[36]. Fig. 4-6 shows an experiment in which we demonstrate that nucleation and growth occur at different overpotentials. A cell was first galvanostatically discharged to 2.05V as above, then held at 2.06V for 18h, during which no nucleation occurred. The cell was then held at 2.02V for 2.5h to induce nucleation but little growth. When the potential was the raised again to 2.06V, significant current flow corresponding to growth of the pre-existing nuclei occurs, despite the absence of nucleation at that potential. This experiment clearly demonstrates the

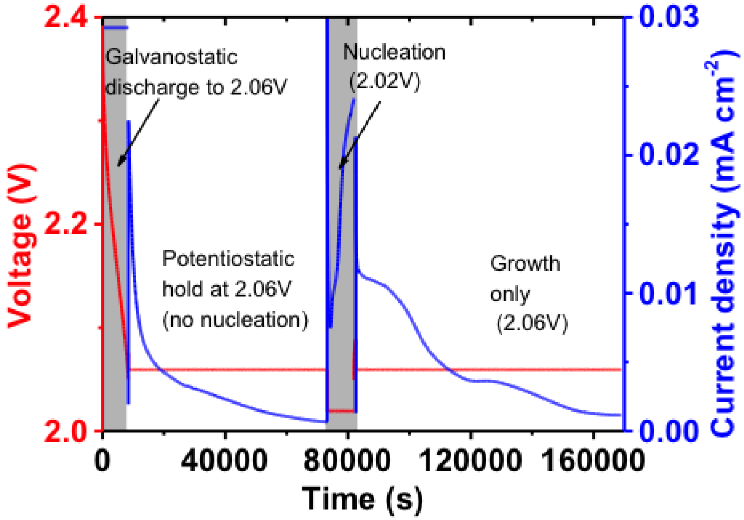

Figure 4-6: Current density and voltage vs. time. The cell was galvanostatically discharged to 2.05V and then kept at 2.06V for 18h, during which no nucleation or growth occurred, and almost all higher order polysulfides were depleted. The cell was then held at 2.02V for 2.5h, during which nuclei formed, then at 2.06V again for 24h, during which a significant amount of current passed, which is due to growth of nuclei formed during the previous period.

possibility for electrokinetic control of performance in batteries that utilize chemical transformations.

Fig. 4-5a-c shows the potentiostatic current vs. time curves measured at several potentials for each of the three glymes tested, and the corresponding Ak^2 values are shown in Fig 4-5d. We find an extremely high sensitivity of the electrodeposition rate to the solvent; at 2.00V potential, there is an 8000x difference in the Ak^2 rate constant between diglyme and tetraglyme solutions. Although the present measurements do not allow independent quantification of A and k, if it is assumed that both change by the same magnitude, then greater than a factor of 20 difference in each of the nucleation and growth rates is inferred. Although this result alone might suggest that diglyme is preferred over triglyme and tetraglyme for a Li-S battery, note that the total storage capacity, (i.e. the area under the potentiostatic curves in Fig. 4-5) scales inversely to the value of Ak^2. This corresponds to the highest lateral growth rate occurring for diglyme followed by triglyme, and tetraglyme. Therefore the thickest

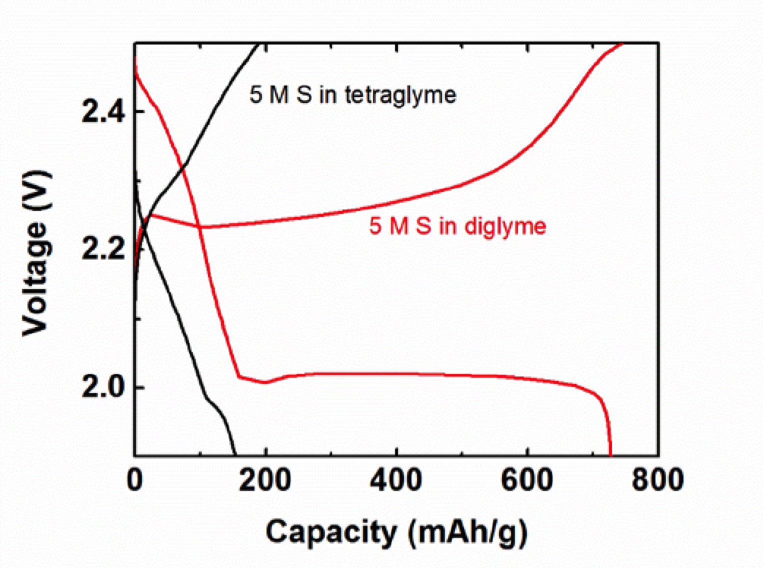

Figure 4-7: Galvanostatic charge-discharge curves for lithium polysulfide suspension cathodes using diglyme and tetraglyme solvents, cycled against Li metal anodes at C/5 between 1.9V and 2.5V vs. Li/Li$^+$ (c.f. Fig. 2-13). The suspension consists of 5M S (as Li_2S_8) in solvent, with 0.5M LiTFSI and 0.15M $LiNO_3$, and 1.5 vol% carbon black (Ketjenblack EC-600JD, Akzonobel, Amsterdam, Netherlands). Note the lack of Li_2S precipitation plateau in tetraglyme, due to the slow nucleation and growth kinetics.

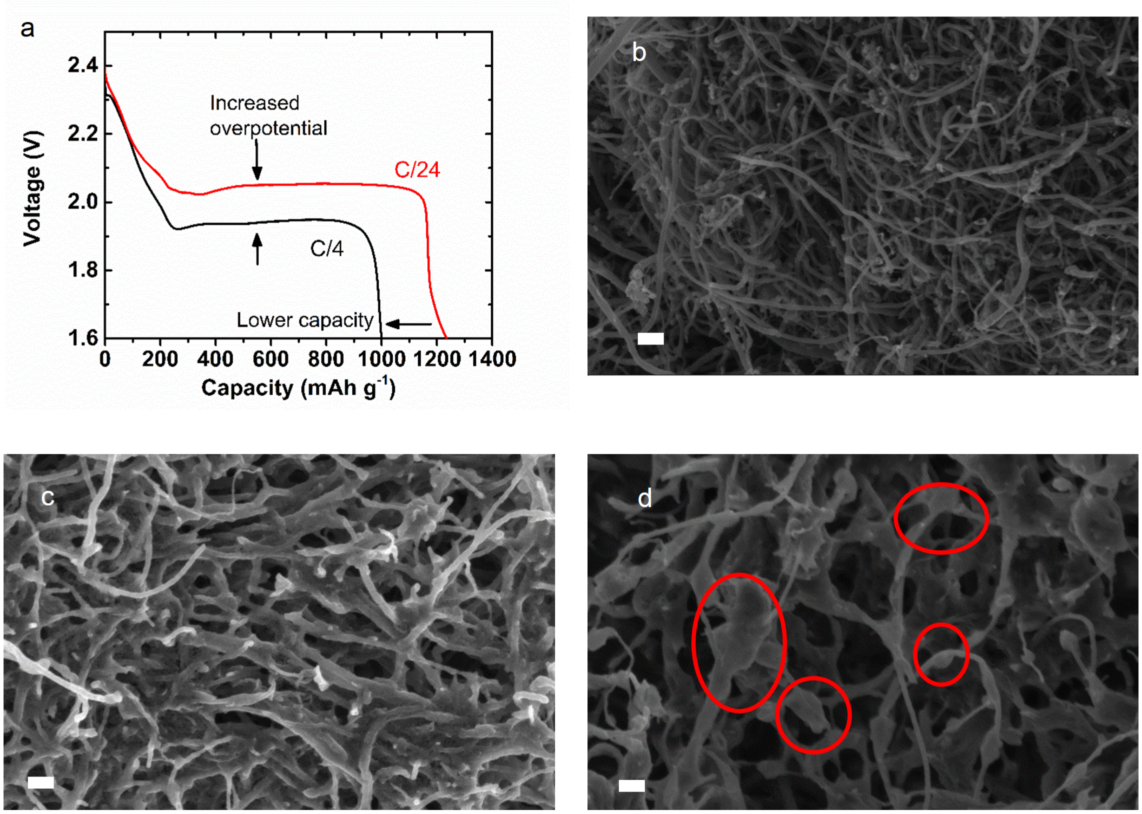

Figure 4-8: (a) Galvanostatic discharge curves for polysulfide solution-MWCNT cathodes discharged at C/4 and C/24 rate. The higher rate results in lower capacity and greater polarization. (b)-(d) SEM images of (b) bare MWCNT, (c) electrode discharged at C/4, and (d) electrode discharged at C/24. The sulfide precipitate appears as a continuous coating in (c) and as a small number of large particles in (d). All scale bars are 200nm.

films and highest capacities at impingement are obtained for tetraglyme. Under galvanostatic conditions in a more realistic battery with far greater surface area, however, the slower kinetics of the tetraglyme solution do result in lower discharge capacity, as shown in Fig. 4-7. The exchange current densities measured in Chapter 3 scale in the same order and by the same approximate magnitude as found here for the reaction rate constants, suggesting the same rate-limiting molecular process.

Although the potentiostatic experiments discussed above facilitate mechanistic studies, Li-S batteries generally use higher surface area current collectors than these carbon fibers, and practical use involves cycling under both galvanostatic and potentiostatic conditions. To investigate nucleation and growth behavior in an environment more representative of such conditions, we prepared cathodes consisting of 6 wt% multi-walled carbon nanotubes (MWCNT) in a 2.5M solution of sulfur (as Li_2S_8) in tetraglyme and cycled the cells under galvanostatic conditions. Similar cathodes were used in our previous work on flowable sulfur catholytes used in a flow cell. Carbon nanotubes were selected as a conductive additive because their simple morphology facilitates imaging of precipitates. Comparing cells discharged at C/4 and C/24 current rates (Fig. 4-8a) both voltage-capacity curves exhibit a voltage dip at the beginning of the Li_2S precipitation voltage plateau, which is a feature that is commonly seen in Li-S batteries [89]. This behavior is consistent with a higher overpotential being necessary to overcome the nucleation barrier; the local potential minima observed were 2.01V at C/24 rate and 1.89V at C/4 rate, both of which are well below the critical potential of 2.06V for nucleation determined by the potentiostatic experiments. The plateau voltages then reach maxima of 2.06V and 1.91V, respectively. At 2.06V in the C/24 experiment, no further nucleation should take place (cf. Fig. 4-6), but growth is possible.

The discharged cells were disassembled and the cathodes examined by SEM and TEM. Electron diffraction analysis of the cathode using TEM (Fig. 4-9) revealed the presence of crystalline Li_2S discharge products on the carbon. For the higher discharge rate (C/4), the cathode exhibited a uniform Li_2S deposit on the surfaces of the MWCNTs that increased the nanotube diameter to 100nm from its initial value of 50nm (Fig. 4-8). The uniform increase in diameter and participation of practically all of the nanotubes suggests a very high nucleation rate. The Li_2S morphology was completely different at the slower discharge rate (C/24), with most of the nanotubes appearing to be uncoated, having diameters similar to those of the starting nanotubes, except where large Li_2S particles (>200nm diameter) were attached. The number density of these precipitates is low compared to those in the C/4 case, consistent with a low nucleation rate, and their morphology was elongated along the axis of the host nanotube, which suggests preferred growth along the carbon surface. This is consistent with largely two-dimensional growth at the three-phase boundary between precipitate, substrate, and electrolyte, with thickening occurring as a result of sur-

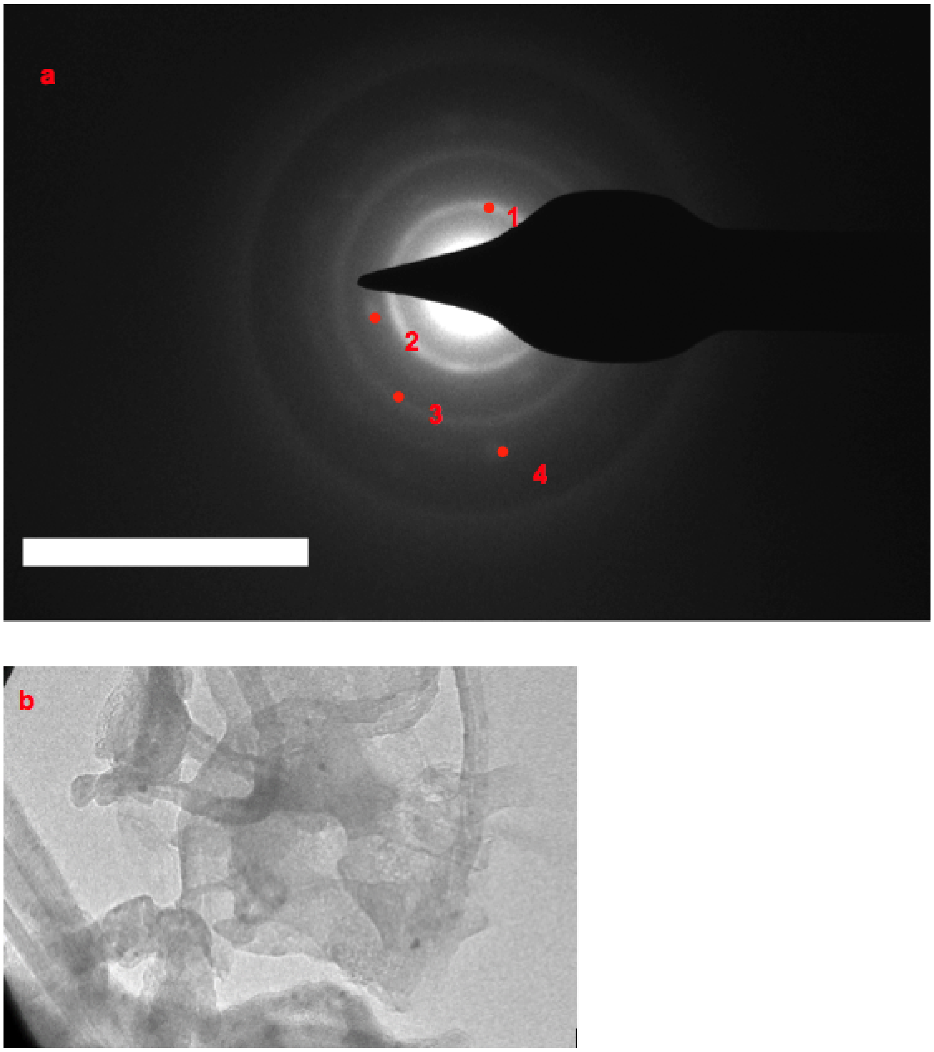

Figure 4-9: (a)Electron diffraction pattern from a MWCNT/polysulfide suspension electrode discharged at C/24. Scale bar: 10 nm^{-1}. (b) bright field TEM image of discharged electrode.

	d spacing (nm)	(h k l)
1	0.337	(1 1 1)
2	0.280	(2 0 0)
3	0.190	(2 2 0)
4	0.172	(3 1 1)

Table 4.1: Interplanar spacing associated with features 1-4 in Fig. 4-9a, indexed with respect to the crystal structure of Li_2S (PDF 00-026-1188)

face diffusion. Similar effects have been seen in lithium-oxygen batteries, which like lithium-sulfur batteries produce an insoluble and insulating product (lithium peroxide, Li_2O_2) during discharge[35]. Cathodes discharged at high rates are found to have conformal, film-like precipitates, while those discharged at slower rates have large, micron-sized particles. This effect has been attributed to the low nucleation rates at high absolute potentials (low overpotentials), resulting in deposition dominated by growth of particles at slow discharge rates and nucleation at higher rates.

Finally, we note that polar conductive substrates such as metal oxides and sulfides have recently been studied as sulfide deposition substrates, and have shown greater selectivity for Li_2S compared to carbon substrates[18, 17, 16, 90]. Surface modification of conductive carbon using amphiphilic polymers has also been used to increase the binding energy between precipitate and carbon[91]. In light of the present results, we can understand the effects of these materials. They provide an interface of lower interfacial energy with Li_2S which thereby acts as a preferred heterogeneous nucleation site. They allow controllable, spatially-selective nucleation, but probably do not change the limiting mechanism of nucleation and growth. We predict that these surfaces will exhibit nucleation of Li_2S at lower overpotential than less polar surfaces such as carbon. Electrodeposition behavior on these surfaces will be studied in Chapter 6.

4.4 Conclusions

In summary, we find that precipitation of Li_2S on conductive substrates proceeds via nucleation followed by 2D growth occurring at the three-phase boundary between precipitate, substrate, and electrolyte. The nucleation of new islands from glyme solvents onto carbon requires 100 mV overpotential. Growth occurs at lower overpotentials and is ultimately limited by the loss of three-phase boundaries upon precipitate impingement. Precipitation during galvanostatic cycling produces different Li_2S morphologies depending on the current rate, which in turn determines overpotential. At high C-rates, large overpotentials produce a high nuclei density and therefore a continuous morphology composed of many small crystallites. Lower C-rates produce fewer but larger precipitates. High storage capacities via Li_2S precipitation can be realized through control of conductive substrate's surface area, choice of solvent, and appropriate electrokinetic control of the nucleation and growth process. Similar behavior is expected for other metal sulfide systems, including low-temperature Na-S batteries.

Chapter 5

Li_2S Electrodeposition Under the Influence of a Redox Mediator

The contents of this chapter were first published in Ref. [92]. Design and synthesis of the redox mediator, along with imaging of Li_2S deposits, were performed by the Helms and Persson groups at Lawrence Berkeley National Laboratory.

5.1 Introduction

Promising next-generation battery chemistries, including lithium-sulfur (Li-S)[1, 93, 94, 12] and lithium-air (Li-O_2)[95, 96, 97, 98], rely on dissolution-precipitation as a mechanism to release and store charge in the cathode. In both cases, the discharge products are electronically insulating[99, 100, 101, 102, 103] (absent defects in the deposits[104, 105, 106]). The insulating nature of these deposits can contribute to poor rate capability, low active-material utilization, and high polarization, which reduce overall energy efficiency[107, 108, 109]. Charge-transport and charge-transfer bottlenecks in these electrochemical cells are eased through the use of electronically conductive, high surface-area electrodes[23, 110, 16, 24, 25]; many electrode architectures have been reported yielding high-performance Li-O_2 cells[111, 112, 113, 114] composite sulfur cathodes[22, 13, 88, 115] and flowable sulfur catholytes for redox flow batteries[46, 53, 116]. Despite these advances, challenges remain in controlling the electrodeposition of the electronically insulating solid phase (i.e., Li_2S for Li-S cells, and Li_2O_2 for Li-O_2 cells) to maintain an accessible electrode surface, which is critical to cell performance. Here we show that Li_2S electrodeposition on carbon current collectors can be redirected away from thin 2D layers and instead toward micron-sized, porous 3D deposits when benzo[ghi]peryleneimide (BPI) is present as a redox mediator (Fig. 5-1. Key to the design of the redox mediator is that the reduction potential of BPI is slightly less than the plateau voltage where the reduction of Li_2S_4 to Li_2S occurs. When BPI is reduced at the electrode surface and given time to diffuse away, it can reduce dissolved polysulfides to Li_2S remotely. With BPI present in the electrolyte, a 6-fold increase in Li_2S formation capacity was observed, leading to an impressive 220% increase in overall sulfur utilization. *Ex situ* analysis of Li_2S electrodeposition at different stages of discharge showed divergent trajectories for Li_2S nucleation and growth in the absence vs presence of BPI. Kinetic studies linked the increased sulfur utilization to BPI's ability to slow the impinging growth of Li_2S on the carbon electrode. By pairing conductive carbons with organic redox mediators, we gain access to hierarchical electrodes reminiscent of biological vasculature[117, 118], where conductive carbon "arteries" facilitate long-range electron transport, while BPI "capillaries" mediate short-range transport and electron transfer between the storage materials and the current collector.

While soluble redox mediators have been explored widely for metal-air batteries[119, 120, 121, 122, 123, 124, 125], their application in Li-S batteries is still nascent. The redox chemistry of sulfur in Li-S cells is observed as two electrochemically distinct steps, a low-potential event ~2.1 V vs Li/Li^+ attributed to the interconversion of Li_2S_4 and Li_2S and a high-potential event ~2.5 V vs Li/Li^+ attributed to the interconversion of S_8 and Li_2S_4[126, 85, 21, 127, 128]. Paramount to the design of any redox mediator for Li-S cells is the careful matching of the mediator's electrochemical potential to either of these interconversion events. With respect to the former, Aurbach et al. have shown that redox mediators can lower the overpotential required for the initial activation of solid-state Li_2S cathodes[129]. With respect to the latter, we have recently reported that perylene bisimides (PBI) serve as redox mediators for the

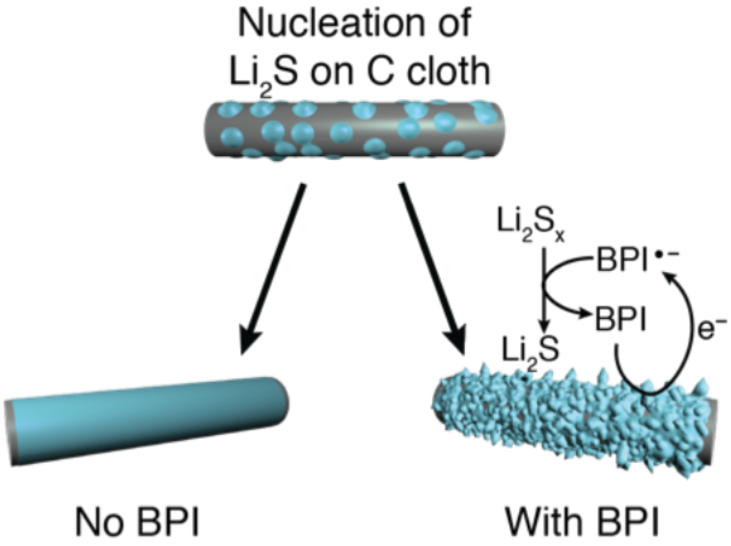

Figure 5-1: Schematic representation of the electrodeposition of Li_2S onto C cloth in the absence (left) and presence (right) of the redox mediator, BPI.

high-voltage plateau. While sulfur utilization was enhanced by 31%[118], this voltage window represents only 25% of the total theoretical capacity of sulfur. Therefore, in this work, our focus turned to identifying a redox mediator for the 2.1 V (vs Li/Li$^+$) reduction event, where Li_2S_4 reduction results in Li_2S precipitation onto the current collector. Although three-quarters of the theoretical capacity of sulfur is gained in this region, there are no reported redox mediators to facilitate Li_2S electrodeposition.

5.2 Methods

Our discovery of BPI as a redox mediator for Li_2S electrodeposition was informed by a robust computational platform known as the Electrolyte Genome that allowed us to screen the redox chemistry of polycyclic aromatic hydrocarbons (PAHs). PAHs are ideal redox mediators, owing to an exceptionally low reorganization energy required for their reduction and oxidation[130, 131, 132]. In our previous work, we screened the electron affinities (E_{ea}) and ionization potentials (E_i) of over 80 PAHs—including acenes, phenylenes, rylenes, coronenes, and benzoperylenes.45 This library helped us identify PAHs with imide substituents that could be further elaborated upon to tune the E_{ea} so these molecules can serve as redox mediators for Li_2S electrodeposition. To refine the library and understand how the number and placement of imide functional groups would impact E_{ea}, a focused library of 20 additional PAH molecules was screened to hone in on a structure with a reduction potential (E_{ea})of ~1.8-2.0 V vs Li/ Li^+. This reduction potential was targeted because it would provide sufficient driving force for Li_2S formation without sacrificing cell power.

Electrolyte and polysulfide preparation

Electrolyte refers to 0.50 M LiTFSI and 0.15 M $LiNO_3$ in diglyme unless otherwise specified. LiTFSI was dried for 16 h under vacuum at 150 °C. $LiNO_3$ was dried for 16 h under vacuum at 110 °C. Diglyme was tested for peroxides prior to use. Diglyme was dried with activated 3 Å molecular sieves until it measured < 20 ppm H_2O. Electrolyte was tested for water content and confirmed to contain < 30 ppm water before use. Solutions of Li_2S_8 (2.5 M sulfur in electrolyte) were prepared by mixing Li_2S (0.144 g, 3.13 mmol), sulfur (S_8, 0.701 g, 2.73 mmol), and 10 ml of electrolyte and heating at 60 °C until all solids were dissolved. Li_2S_8 solutions were kept at 60 °C in order to prevent precipitation of insoluble species and cooled to room temperature prior to use.

Electrochemistry

The electrochemical cell was configured with a glassy carbon working electrode and lithium metal reference and counter electrodes. Working solutions for cyclic voltammetry (CV) were separated from lithium counter and reference electrodes with a glass frit with an average pore size of ~7 nm and thickness of 5 mm obtained from Advanced Glass and Ceramics (St. James, NC, USA). In order to account for the potential drop across a highly resistive frit, all CV measurements were corrected for iR drop by measuring the impedance between the working and reference electrodes with an applied AC voltage with frequency of 100 MHz and correcting for 85% of the expected IR drop. The CV of BPI was conducted in electrolyte with 2.5 mM BPI at 1 mV/s. The CV of polysulfide was carried out in electrolyte at 12 mM sulfur of nominal composition Li_2S_8 at 1 mV/s.

Li-S Cell Testing

0.600 mL tetraglyme was added to BPI (19 mg) and the mixture was heated at 80 °C until the BPI dissolved. A circular piece of C cloth (5 cm diameter) was heated to 80 °C in a Petri dish. The BPI solution was dropcast evenly across the C cloth. The C cloth was then cooled to ambient temperature and dried under reduced pressure for 3 days.

Lithium disks (3/8 inch diameter) were punched from 1.5 mm thick Li foil and soaked in electrolyte for $>$ 1 h. One side of the Li disk was scraped with a spatula to expose a shiny Li surface. The scraped side was pressed onto a nickel or steel electrode, 6 μL electrolyte and a piece of Celgard (1/2 inch diameter) were placed on top. Two pieces of C cloth (with or without BPI) were placed in the well (0.5 mm deep, 1/4 inch diameter) of a gold-coated nickel electrode. About 18 μl catholyte (1.0 M sulfur as Li_2S_8 in electrolyte, d = 1.05 g/ml) was added to the well with the C cloth (16-22 mg weight of catholyte), the weight was recorded, and the cell assembled.

5.3 Results and Discussion

Guided by predictions from the Electrolyte Genome, we designed and synthesized gram-scale quantities of a new N-aryl-substituted benzo[ghi]peryleneimide bearing two tri(ethylene oxide) substituents. These substituents provided for BPI solubility in ether-based electrolytes commonly used in Li-S cells. Owing to the single imide substituent, BPI undergoes a single-electron reduction in the operating window of the Li-S battery (1.8-2.8 V vs Li/Li$^+$), leading to an open-shell radical anion (BPI$^{\bullet-}$). Using cyclic voltammetry in diglyme-based electrolyte, we determined the reduction potential ($E_{1/2}$) of BPI to be 1.980 V vs Li/Li$^+$ (Fig. 5-2B, orange trace), which agreed well with the calculated value of 1.99 V vs Li/Li$^+$ when a Li$^+$ counter-ion was included in the calculation. Thus, BPI provides ∼100 mV driving force for the reduction of sulfur species. This small overpotential ensures that BPI should be able

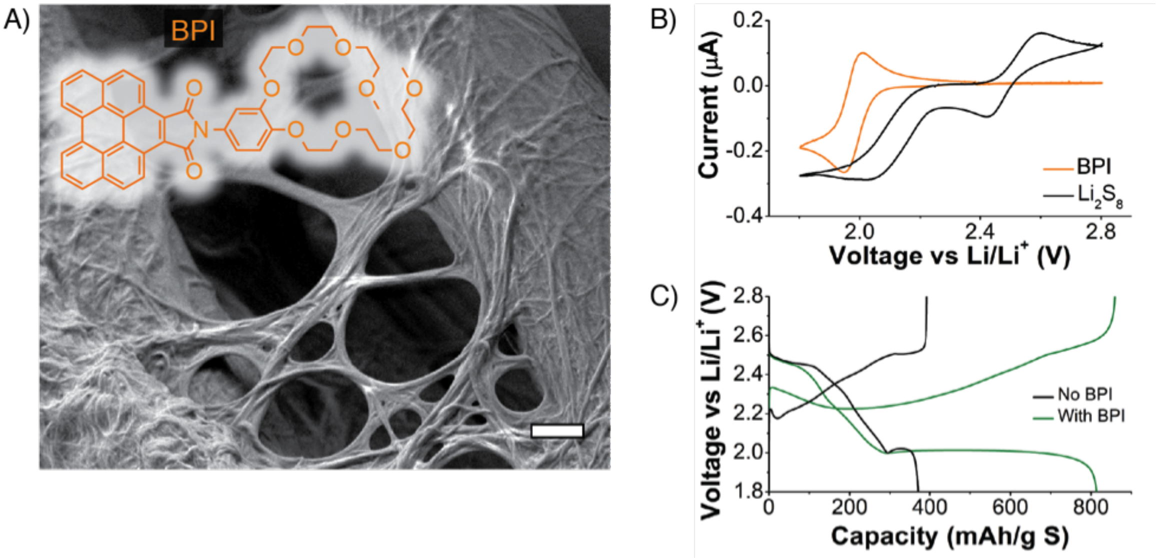

Figure 5-2: (A) Chemical structure of the redox mediator BPI (inset) and SEM micrograph of BPI dropcast onto C cloth and dried under vacuum. Scale bar = 2 μm. (B) Cyclic voltammograms of BPI (orange trace, 2.5 mM BPI) and Li_2S_8 (black trace, 12 mM sulfur) at 1 mV/s. The electrolyte is 0.50 M LiTFSI and 0.15 M $LiNO_3$ in diglyme, with a glassy C working electrode and lithium reference and counter electrodes. (C) Second cycle discharge and charge profiles of Li-S cells at a C/8 rate in the absence (black trace) or presence (green trace) of BPI redox mediator.

to reduce all sulfur species to Li_2S, but is not expected to significantly lower the operating voltage of the Li-S cell.

BPI can be introduced to Li-S cells by dissolution in the electrolyte or by dropcasting onto C cloths (3% w/w BPI with respect to the sulfur catholyte), with similar results. Our implementation of C cloth electrodes, which feature 8-μm-thick carbon fibers, was chosen because they allow for careful visualization of Li_2S electrodeposition throughout the battery's operation. A hierarchical morphology of the BPI-C cloth hybrid in the dry state was apparent in the scanning electron micrograph (Fig. 5-2A) where BPI assemblies, microns in length and formed through π-stacking of the aromatics, both covered and traversed the larger-diameter carbon fibers. Once polysulfide-containing electrolyte is added, these nanowire assemblies are expected to dissolve and circulate into the electrolyte volume, with the persistence length of the assemblies considerably shortened[133, 134].

To ascertain whether BPI has an effect on Li_2S electrodeposition, galvanostatic cycling was carried out on Li-S cells (Swagelok type) prepared with dissolved polysulfide cathodes alongside C cloth electrodes either with or without BPI. In the absence of BPI, the first complete discharge capacity was 316 ± 18 mAh/g S(N = 16). On the other hand, with BPI present (3% w/w with respect to catholyte), the capacity increased to 691 ± 18 mAh/g S(N = 16). This corresponds to an impressive 2.2-fold increase in discharge capacity (Fig. 5-2C). Notably, this increase in capacity was due to a greatly extended 2.0 V plateau, indicative of increased Li_2S formation as would be predicted for BPI were it serving as a redox mediator. No difference in cell performance was observed when BPI was introduced to the system by dissolution in the electrolyte as opposed to dropcasting on C cloth. Cells with dissolved BPI show a discharge capacity of 696 ± 41 mAh/g S(N = 7), indicating that BPI on the C surface is not simply serving as a nucleation point for Li_2S. Further experiments were conducted with the BPI dropcast onto C cloth for ease of cell assembly.

To quantify the respective gains in capacity between the high- and low-voltage regimes, we divided the discharge curve between the soluble regime ($S_8 + 4Li^+ + 4e^- \rightarrow 2Li_2S_4$) and the Li_2S precipitation plateau ($Li_2S_4 + 6Li^+ + 6e^- \rightarrow 4Li_2S$)

at the position of the dip in the discharge curves at ~2.0 V in Fig. 5-2C, which is attributed to the overpotential required for nucleation of Li_2S[80]. The average capacities for the soluble regime were essentially identical (within error): 242 ± 18 mAh/g S without BPI and 250 ± 18 mAh/g S with BPI. However, the average capacity for Li_2S electrodeposition was 446 ± 12 mAh/g S with BPI present, whereas it was only 74 ± 2 mAh/g S for cells lacking BPI. Thus, the presence of BPI redox mediator resulted in a 6-fold increase in Li_2S electrodeposition.

In order to better understand nucleation and growth of Li_2S on C cloth with BPI present, we carried out *ex situ* analysis of Li-S cells at different states-of-charge (SOC). At specified points along the discharge and recharge (Fig. 5-3A), we disassembled the cells, retrieved the C cloth from those cells, washed away the electrolyte containing salts, polysulfides and BPI, and then imaged the Li_2S discharge products using scanning electron microscopy (SEM); we also collected energy- dispersive X-ray (EDX) spectra of those samples to verify the chemical identity of the discharge products. Upon nucleation (Fig. 5-3A, Point 1), small islands of Li_2S were distributed over the C microfibers both when BPI was present (Fig. 5-3F) and absent (Fig. 5-3B) from the cell. The presence of a soluble redox mediator is not expected to change Li_2S nucleation, and does not appear to do so here. With BPI present, a globular Li_2S morphology started to form (Fig. 5-3G) midway though the 2.0 V plateau (Point 2), yet the underlying C cloth remained visible. On the other hand, without BPI present, islands of Li_2S began to impinge (Fig. 5-3C), leaving little of the C surface available for further redox chemistry with dissolved polysulfides. By the end of discharge (Point 3), the carbon cloth from the cells with BPI showed even larger, porous Li_2S deposits, up to 3.8 μm, growing outward until the underlying carbon cloth current collector was no longer visible (Fig. 5-3H).

The growth trajectory of these 3D deposits involves reduction of BPI at the C cloth surface, followed by diffusion and circulation of $BPI^{\bullet-}$ into the catholyte solution where it reduces polysulfides to Li_2S which can deposit onto either Li_2S or C surfaces resulting in the observed 3D morphologies. This process is competitive with the direct reduction of polysulfides at the electrode surface, which instead coats the C surface in

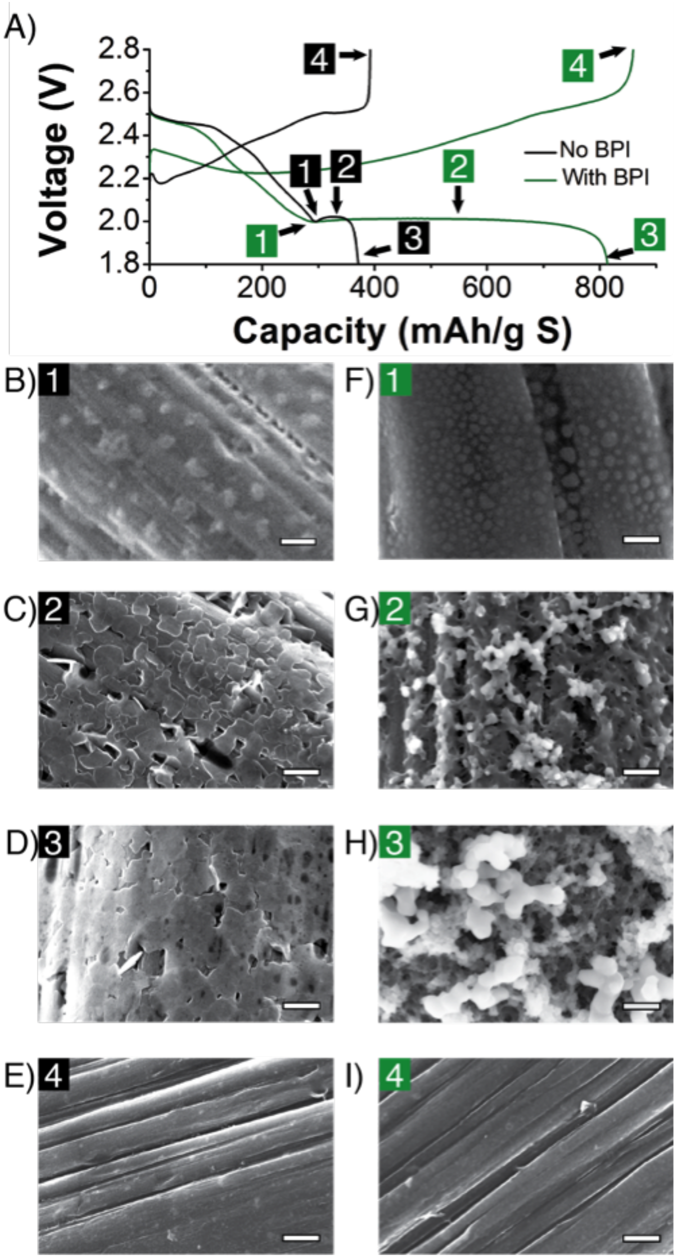

Figure 5-3: Progressive electrodeposition of Li_2S on C cloth, imaged at different states-of-charge in Li-S cells with BPI absent (left) and BPI present (right) (A) The first discharge/charge cycle at C/8 rate. States-of-charge are indicated as Points 1-4 where separate cells were stopped to image the Li_2S deposits on the C cloth. SEM images of Li_2S electrodeposition on C cloth from a cell without BPI are shown: (B) at nucleation (Point 1); (C) during the Li_2S voltage plateau (Point 2); (D) at the end of discharge (Point 3); and E) after recharge (Point 4). SEM images of Li_2S electrodeposition on C cloth from a cell with BPI: (F) at nucleation (Point 1); (G) during the Li_2S voltage plateau (Point 2); (H) at the end of discharge (Point 3); and (I) after recharge (Point 4). Scale bars = 500 nm.

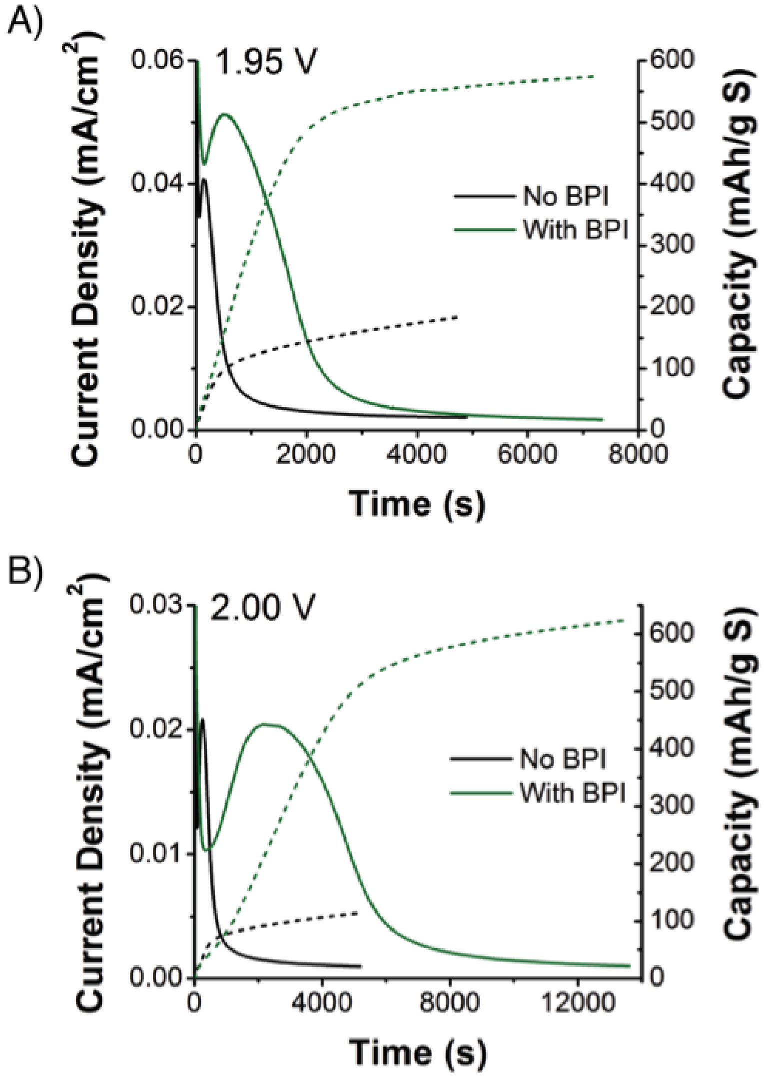

Figure 5-4: Current transients during the potentiostatic deposition of Li_2S on C cloth. Cells were first discharged to 2.09 V, and the time plot starts upon lowering the voltage to 1.95 V (A) or 2.00 V (B). Solid lines indicate cells containing BPI and dashed lines indicate cells without BPI. Current densities are shown in black, and capacities are shown in blue.

thin conformal layers. To understand the relative rates of these competitive processes, we further studied these Li-S cells under potentiostatic discharge. To do so, the cells were initially discharged potentiostatically to 2.09 V to reduce all S_8 and higher order polysulfides to Li_2S_4 (nominally), in order to study only the electrodeposition of Li_2S. The current was then monitored over time upon lowering the potential to either 2.00 or 1.95 V to provide a driving force for Li_2S nucleation and growth (Fig. 5-4). In both cases, the current trended toward 0 whether or not BPI was present, which indicated that sulfur utilization is ultimately limited by impingement of insulating Li_2S blocking the carbon surface. If Li_2S were to continue to be reduced after the electronically conductive C cloth surface were covered, a horizontal asymptote would instead be expected at a current density >0 mA/cm^2. At 1.95 V, the current density peaked at a higher value and at a later time when BPI is included, leading to a 3.1-fold increase in capacity due to Li_2S deposition (Fig. 5-4A). At 2.00 V, while the cell with BPI did not obtain a higher current density than without BPI, this current density was maintained for much longer when BPI is present, leading to a 5.5-fold increase in capacity due to Li_2S deposition (Fig. 5-4B).

The potentiostatic electrodeposition of Li_2S in the presence of a redox mediator can be modeled as a superposition of two processes: the direct formation and growth of Li_2S islands at the carbon surface (which is described in Chapter 4 and which occurs whether the mediator is present or not) and the reduction of the mediator at the carbon surface, which later reacts with polysulfides resulting in the remote deposition of Li_2S. The potentiostatic current density vs. time relation is the sum of their respective contributions, J_{BFT} and J_{med}:

$$J(t) = J_{BFT}(t) + J_{med}(t) \tag{5.1}$$

J_{BFT} is simply the current from the BFT model described in Chapter 4 (here, the version with instantaneous nucleation and 2-D growth is used, as it produces a better fit in this set of experiments than does the model with progressive nucleation):

$$\frac{J_{BFT}(t)}{J_m} = \frac{t}{t_m} exp\Big[-\frac{1}{2}\Big(\frac{t^2}{t_m^2}-1\Big)\Big] \tag{5.2}$$

J_m and t_m are the maximum current density and the time at which the maximum current density occurs, respectively[45, 135]. To model J_{med}, we assume that the reaction is gated by the reduction of BPI to $\text{BPI}^{\bullet-}$ (i.e. at the carbon surface) and that the concentration of BPI in solution remains constant. It follows that this current is proportional to the amount of carbon surface area available (i.e. not covered by Li_2S deposits):

$$J_{med}(t) = c(1-Y) \tag{5.3}$$

Where c is the current density on an unpassivated surface, and Y is the fraction of the surface covered by Li_2S. 1-Y is simply the exponential factor in Equation 5.2. Combining these results in:

$$J_{med}(t) = cexp\Big[-\frac{1}{2}\Big(\frac{t^2}{t_m^2}-1\Big)\Big] \tag{5.4}$$

$$\frac{J(t)}{J_m} = \Big(\frac{t}{t_m}+c\Big) exp\Big[-\frac{1}{2}\Big(\frac{t^2}{t_m^2}-1\Big)\Big] \tag{5.5}$$

The term c accounts for additional current due to the redox mediator; when no redox mediator is present c = 0, but this term is required when BPI is present (c = 1.24 at 1.95 V and c = 0.14 at 2.00 V). This model fits the data both with and without redox mediator, indicating that in both cases the current is proportional to the remaining free surface of carbon (Fig. 5-5). This implies that both with and without redox mediator, impingement of insulating Li_2S deposits covering the carbon surface ended discharge prior to reaching the theoretical limit; however, the addition of BPI redox mediator dramatically enhanced sulfur utilization prior to impingement. The width of the peak fit by Equation 5.5 can be used to determine the density of nuclei N_0 and rate constant of lateral growth of Li_2S k, using equation 5.6.

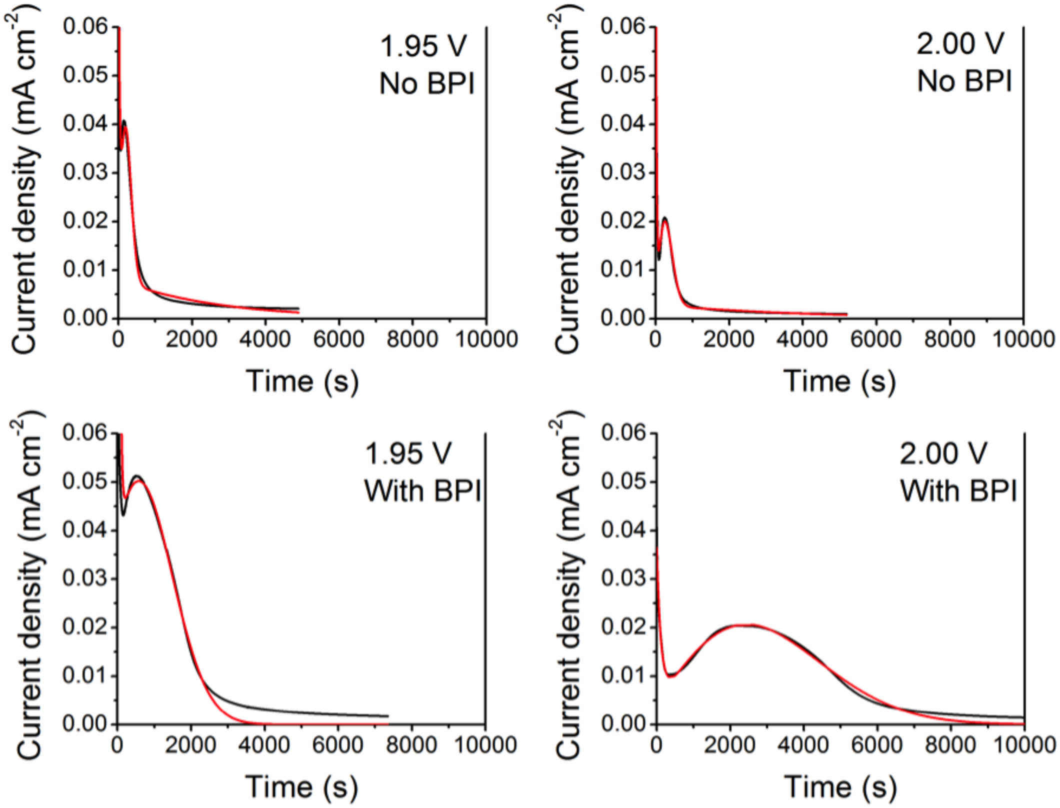

Figure 5-5: Overlayed experimental data (black) and model fits (red).

$$t_m = (2\pi N_0 k^2)^{-1/2} \tag{5.6}$$

where N_0 is the areal density of nuclei. The term N_0k^2 can be compared as an effective rate constant for coverage of the C cloth surface by Li_2S. Without redox mediator, $N_0k^2 = 4.21$ x 10^{-6} s^{-2} and 2.52 x 10^{-6} s^{-2}, at 1.95 and 2.00 V, respectively,and with redox mediator, $N_0k^2 = 1.51$ x 10^{-7} s^{-2} and 2.35 x 10^{-8} s^{-2}, at 1.95 and 2.00 V, respectively. Addition of BPI resulted in a 28-fold reduction in the coverage rate at 1.95 V and a 107-fold reduction at 2.00 V. In both cases, having the soluble redox mediator slows the coverage of C cloth surface by allowing deposition of Li_2S onto previously formed Li_2S and not just at the carbon surface. The coverage of the C surface is likely slowed by (1) direct competition between BPI and polysulfides for reduction at the carbon surface and (2) $BPI^{\bullet -}$ intercepting incoming soluble polysulfides and reducing them to Li_2S away from the C cloth surface, effectively lowering the local concentration of polysulfide at the carbon surface.

5.4 Conclusions

In conclusion, with a redox mediator that is tuned to the potential of Li_2S electrodeposition, we are able to mitigate the limitations imposed by the surface area required for nucleation and growth of Li_2S by providing a new mechanism for Li_2S deposition. Both the potentiostatic and galvanostatic discharge experiments confirm that the addition of 3% (w/w) BPI redox mediator increases the amount of Li_2S produced 6-fold. By adding an equivalent mass of C cloth, only an additional 24 mAh/g S could be added to the capacity, based on the additional surface area available for 2D deposition of Li_2S. Without BPI, polysulfides are reduced at the C cloth surface to form an insulating, conformal coating of Li_2S, but with a redox mediator, BPI reduces polysulfides to Li_2S away from the surface, allowing deposition of Li_2S not only on the C cloth surface, but on previously deposited Li_2S. This forms porous, three-dimensional structures of Li_2S and delays coverage of the electroactive C cloth with an insulating Li_2S layer that ends discharge. This implies that, for a given amount of Li_2S formed during cycling, less conductive carbon additive should be required, allowing for a greater percentage of the battery to be dedicated to active material. With an understanding of the mechanism by which BPI redox mediator extends sulfur utilization, rapid development of Li-S cells with an increased energy density is underway through the integration of BPI with high surface area current collectors at high sulfur loadings.

Chapter 6

Effects of Electrolyte/Sulfur Ratio and Conductive Surface on Electrodeposition Kinetics

6.1 Introduction

Fast kinetics for electrodeposition of Li_2S are essential for high capacity and rate capability in Li-S batteries.

Low electrolyte/sulfur (E/S) ratios are essential for high energy density and low cost. Because of the high solubility ($\sim$8 mol S/l) of polysulfide intermediates electrolytes undergo significant changes in composition during each cycle, and the E/S ratio sets an upper bound on the concentration of polysulfides(Fig. 3-1). High polysulfide concentration has been shown in Chapter 3 to reduce electrolyte conductivity and solution-regime reaction rates.

In this chapter, we investigate the effects of polysulfide concentration on the kinetics of the electrodeposition process. Although previous studies have shown decreased cycle life and rate capability as a result of low E/S ratio, this is the first one to quantify the effects of E/S ratio on the kinetics of the Li_2S electrodeposition process, which is responsible for the majority of the capacity in Li_2S batteries [136, 29]. We find that

Li_2S deposition becomes remarkably sluggish at the high polysulfide concentrations found in Li-S batteries with low electrolyte content. The slower electrodeposition kinetics are correlated with significantly higher polarization and lower capacity and rate capability in Li-S cells with reduced electrolyte.

In addition, the influence of the conductive support material on electrodeposition kinetics has been investigated. Various materials have recently been evaluated as a substitute for carbon as conductive nucleation promoters, including metal oxides [17, 16, 110, 19], metal sulfides [18, 90], and conductive polymers[91]. Ionic compounds (that are also electronic conductors) in particular have been found to promote nucleation, which is attributed to their greater affinity for lithium sulfide. We compare the performance of bare carbon fiber electrodes to those coated with indium tin oxide (ITO) and aluminum-doped zinc oxide (AZO), and show that both oxides improve electrodeposition performance significantly. AZO, in particular, led to a greater improvement and is appealing because of the low cost of zinc. The addition of AZO to sulfur/carbon composite cathodes was shown to increase capacity and reduce polarization during galvanostatic discharge.

6.2 Methods

Potentiostatic testing of electrodeposition kinetics

Polysulfide solution (Li_2S_6) was prepared by combining stoichiometric amounts of sulfur and Li_2S (Alfa Aesar) in a 1:1 by volume mixture of 1,2 dioxolane (DOL) and 1,3 dimethoxyethane (DME) (Sigma-Aldrich, used as received) and stirring for 24h at 60°C. $LiNO_3$ (Sigma-Aldrich) and lithium bis(trifluoromethane) sulfonamide ("LiTFSI," BASF) were mixed into the polysulfide solution. Solid reagents were dried under vacuum overnight.

Testing was performed in 2-electrode Swagelok cells with a Li foil (Alfa Aesar) counter electrode. The Li was placed in electrolyte (0.5M LiTFSI, 0.15M $LiNO_3$, no polysulfide, in DOL/DME 1:1) for at least 1h and then dried off prior to use. A porous polymer separator (Tonen Chemical Corporation, Tokyo, Japan) wetted with 6 ml of electrolyte was used to separate the two electrodes. The working electrode current collector was a Au-coated stainless steel rod with a 0.5 mm deep and 6.4 mm diameter well, into which a disk of carbon cloth (Avcarb 1071 HCB) were placed. ∼22 mg of polysulfide solution was added to the carbon cloth. Cells were first held at 2.19V for 2h to reduce higher order polysulfides to Li_2S_4. They were then held at a potential of 2.05 V or 2.07 V to induce nucleation and growth of Li_2S, or an overpotential of 140 mV and 120 mV respectively. These potentials were chosen as they are close to the minimum observed at the beginning of the lower voltage plateau during a typical discharge. Potentiostatic intermittent titration technique (PITT) testing was performed in similar cells, using 5 mV potential steps and a current cutoff of C/400. Some PITT experiments used suspensions of carbon black (Ketjenblack EC-600JD) or AZO (∼40 m^2/g, Nanoscale and Amorphous Materials, Inc.). Either 2.5 vol% carbon black or 25 vol% AZO (volume fractions chosen to maintain a consistent surface area) was suspended in 1 mol S/l polysulfide solution. Suspensions were first stirred manually, then sonicated for 30 min.

Cast electrode fabrication

Sulfur powder (99.5%, Alfa Aesar), deionized water, carboxymethyl cellulose (CMC) binder, and Super-P carbon (Alfa Aesar) were mixed together for 30 min in a SPEX high-energy ball mill using polycarbonate milling media and container. The CMC was first dissolved in the water at a concentration of 16 mg/ml, and then mixed with the solid components to a target composition of 50% S, 44% Super-P, and 6% CMC by mass. For some electrodes, 10%, 50%, or 100% of the Super-P was replaced with an equivalent volume of AZO nanoparticles (20-40nm, NanoAmor). The slurry was cast onto aluminum foil to a thickness of 0.25 mm, or a S loading of approximately 2 mg/cm^2. The slurry was allowed to dry under ambient conditions, and then further dried under vacuum. Swagelok® cells were assembled using Li metal negative electrodes and carefully measured amounts of electrolyte to reach the target E/S ratios.

Oxide-coated carbon fiber cloth

Indium tin oxide coated carbon fiber cloth: Carbon fiber cloth was heated in air at 700°C for 10 min, then coated using a sol-gel process. The sol was prepared as described in Ref.[137] Tin (IV) acetate and indium (III) nitrate trihydrate (Alfa Aesar) were separately dissolved in ethylene glycol (Sigma Aldrich), the former at 80°C and the latter at ambient temperature. The two solutions were combined in a In^{3+}:Sn^{4+} molar ratio of 90:10 and stirred for 2h at ambient temperature. The total concentration of cations was 0.5M. Triethanolamine (Sigma-Aldrich) was added dropwise to a concentration of 0.25M. The sol was diluted to a cation concentration of 0.2M, coated on the carbon fiber cloth, then heat treated for 10 min at 400°C. These steps were repeated to increase the thickness, and the material was finally annealed in air for 1h at 400°C. The target thickness was 150 nm.

Aluminum-doped zinc oxide coated carbon fiber cloth: The same carbon fiber cloth was used as for the ITO coatings, without initial heat treatment. Zinc oxide was prepared according to a previously published method[138]. Zinc(II) acetate dihydrate and aluminum nitrate nonahydrate (Alfa Aesar) were dissolved in ethanol to a Zn:Al molar ratio of 98:2 and a Zn^{2+} concentration of 0.4M. Diethanolamine was added dropwise to reach a concentration of 0.4 M. This solution was stirred for 24h and diluted to 0.1 M. The carbon cloth was coated with the liquid precursor solution, following which the cloth was dried at 300°C for 6 min. The coating and drying steps were repeated to increase the coating thickness. The films were then annealed at 400°C in air for 1h. The target thickness was 150 nm. Resistivity for sol-gel AZO films is typically less than 10^{-3} Ωcm, corresponding to an area-specific resistance of less than 1.5×10^{-6} Ω cm^2 at this thickness[139]. Since typical current densities in our experiments are less than 0.1 mA cm^{-2}, we expect a negligible contribution to Ohmic resistance from these films.

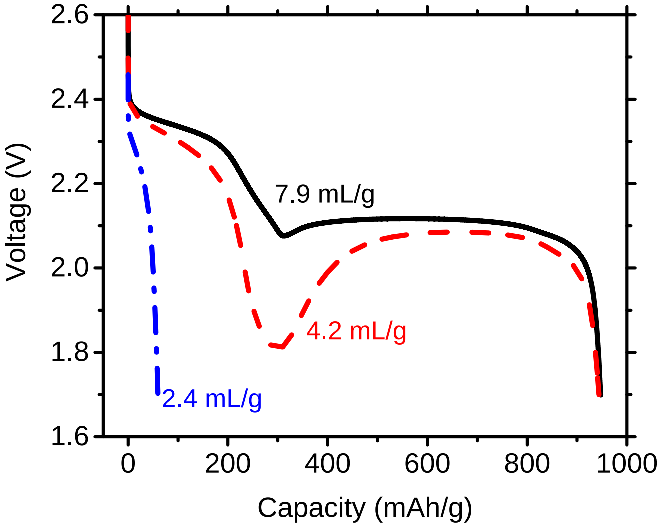

Figure 6-1: Galvanostatic (C/4) discharge curves for Li-S cells with sulfur-carbon composite cathodes at three different electrolyte/sulfur ratios. As the electrolyte/sulfur ratio decreases from 7.9 ml E/g S, the voltage drop at 300 mAh/g, which corresponds to the onset of Li_2S nucleation and growth, increases dramatically in size before disappearing altogether. Electrolyte: DOL:DME 1:1, 0.5M LiTFSI, 0.15M $LiNO_3$.

Scanning electron microscope characterization

Samples were imaged in a Zeiss Merlin high-resolution SEM, with in-lens secondary electron detector and operating at 3 kV accelerating voltage. Energy-dispersive X-ray spectroscopy (EDX) analysis was performed in the same SEM, typically using a 10 kV accelerating voltage.

6.3 Results and Discussion

Swagelok® cells containing sulfur/carbon composite positive electrodes and lithium metal negative electrodes with E/S ratios of 7.9, 4.2 and 2.4 ml/g S were galvanostatically discharged at a rate of C/4 between the voltage limits of 2.6-1.7 V. As shown in Fig. 6-1, at the highest E/S ratio of 7.9 ml/g, which corresponds to the lowest dissolved sulfur concentration in the electrolyte of 3.9 M (assuming the sulfur is fully dissolved), the initial discharge capacity is 947 mAh/g. The discharge curve shows features typical of Li-S including a high voltage plateau and a regime of rapidly decreasing voltage corresponding respectively to the dissolution of sulfur and the reduction of higher order polysulfides, followed by a voltage "dip" centered at about 400 mAh/g, followed by a voltage plateau corresponding to the co-existence of Li_2S_4 and solid Li_2S. As described in our previous work, the dip corresponds to the overpotential required for nucleation and initial growth of Li_2S[46]. The capacity is typical of a standard sulfur electrode, and the polarization on the plateau is 100 mV below the equilibrium voltage of 2.19 V.

At a lower E/S ratio of 4.2 ml/g, which corresponds to 7.4 M S, and is approximately the solubility limit of polysulfide at room temperature, the discharge capacity is nearly identical, but there is a significant increase in polarization. The increase in polarization is especially dramatic for the feature associated with nucleation and growth, where the minimum voltage now reaches 1.81 V as opposed to 2.08 V for E/S ratio of 7.9 ml/g S. Taken relative to the equilibrium voltage for the Li_2S plateau of 2.19 V, these voltage minima correspond to overpotentials of 380 mV and 110 mV for E/S of 4.2 and 7.0 ml/g S, respectively[80, 72, 71, 89]. The nucleation and growth process clearly become much more sluggish as electrolyte volume decreases and maximum polysulfide concentration increases, as is further quantified below.

At a ratio of 2.4 ml/g (13 M S), the feature associated with nucleation and growth disappears altogether and the lower voltage plateau is not observed at all. The total capacity (<60 mAh/g) is much less than that which would be expected from the reduction of S_8 to Li_2S_4 (∼418 mAh/g), which typically occurs between 2.5V and 2.15V. This may be because there was not enough electrolyte to dissolve the sulfur fully, given that the solubility is about 8 M S. Indeed, some studies have demonstrated that solid sulfur can exist throughout the discharge process without being fully dissolved[21, 140]. This sulfur may limit access of the polysulfide to the carbon, limiting the effective surface area of the conductive carbon and increasing impedance due to sluggish reaction kinetics.

Potentiostatic electrodeposition experiments were performed at 2.07 V and 2.05 V vs. Li/Li^+ (corresponding to the lower voltage plateau) on carbon cloth working electrodes using polysulfide solutions ranging from 1M to 7M (sulfur basis). The resulting current density vs. time curves are shown in Fig. 6-2b and 6-2c, respectively.

The shape of these curves has been described in our previous work, in which we determined that electrodeposition occurs by a nucleation and 2D growth process on the carbon surface[80, 45]. The current drops initially due to nonfaradaic double-layer charging and the reduction of remaining higher-order polysulfides. It then rises as nuclei of Li_2S are formed and grow larger, the current reaching a peak after which it decays due to impingement of nuclei and passivation of the surface by electronically insulating sulfide, which inhibits charge transfer. We determined that the current decay is not due to a diffusion limitation, as the decreasing portion of the current-time curve cannot be fitted using the Cottrell equation[80, 41, 135]. Under potentiostatic conditions (i.e. with a constant thermodynamic driving force) the process is well described by the Avrami equation (Equation 6.1), where Y is the fraction of total Li_2S that has been formed:

$$Y(t) = 1 - exp\left[-N_0\pi(kt)^2\right] \tag{6.1}$$

In this particular system, the process can be modeled by a 2-dimensional island growth process with instantaneous nucleation. N_0 is the density of nuclei per unit area, and k is the lateral growth rate of islands[39]. The associated current vs. time curve can thus be modeled using Equation 6.2, where J_m is the maximum current density and $\mathrm{t_m}$ is the time at which the maximum current occurs, and the current is proportional to the time derivative of Equation 6.1:

$$\frac{J(t)}{J_m} = \frac{t}{t_m} exp\Big[-\frac{1}{2}\Big(\frac{t^2}{t_m^2} - 1\Big)\Big] \tag{6.2}$$

Significantly, the nucleation density and growth rate (as a combined rate constant $\mathrm{N_0k^2}$) can be determined using the time at which the current peak occurs, using Equation 6.3 (more nuclei and faster growth result in faster passivation of the surface, and an earlier onset of current decay):

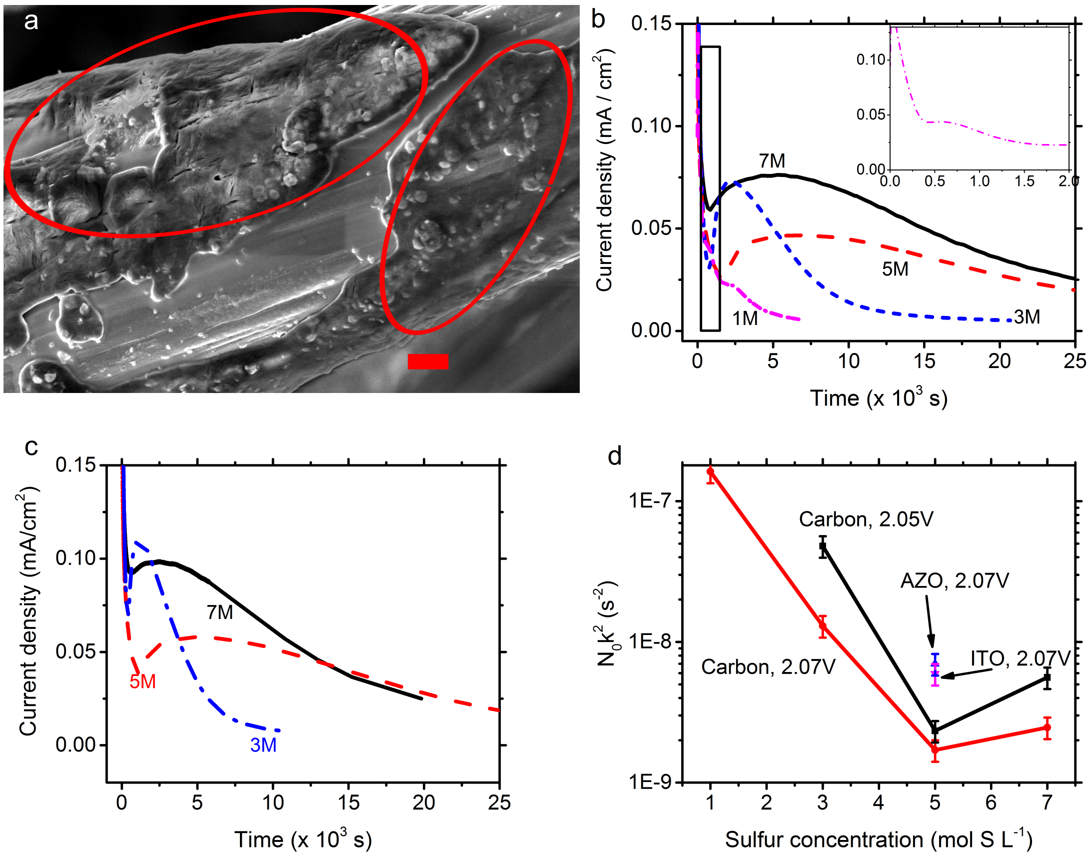

Figure 6-2: Effect of sulfur concentration on potentiostatic deposition. (a) Scanning electron microscope image of untreated carbon fiber after electrodeposition of Li_2S (2h, 2.07 V, 3 mol S/l). Areas covered by sulfide are indicated in red. Scale bar: 1 μm (b) Current density vs time curves for electrodeposition on carbon at 2.07 V from polysulfide solutions of various concentrations. 1 M curve is enlarged in the inset. (c) Current density vs. time curves for electrodeposition on carbon at 2.05 V (d) Values of N_0k^2 rate constant measured at various sulfur concentrations, on carbon at 2.05V and 2.07V, and on AZO and ITO at 2.07 V.

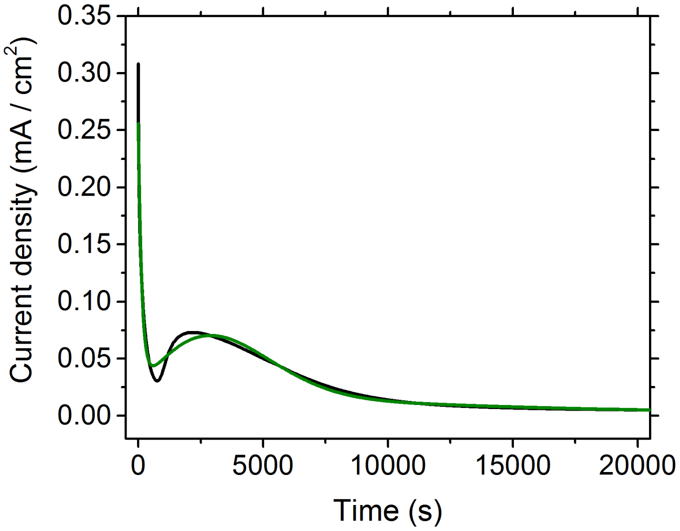

Figure 6-3: Experimentally measured (black) and fitted (green) data for Li_2S electrodeposition from 3M sulfur solution, onto untreated carbon cloth, at 2.07V.

$$t_m = (2\pi N_0 k^2)^{-1/2} \tag{6.3}$$

The value of t_m is independent of the surface area of the electrode, since both the spacing and growth rates of nuclei are fixed and the same amount of time passes before impingement occurs. The current minimum before the peak arises from the same phenomenon as the voltage minimum observed in galvanostatic discharge curves, i.e. the slow rate of transformation at the beginning of the phase change process. The background current resulting from double-layer capacitance and the reduction of higher-order polysulfides was fitted as the sum of two exponential decay functions (Fig. 6-3).

For electrodeposition on carbon at 2.07V (Fig. 6-2a), considerable variation in N_0k^2 occurred as sulfur concentration was changed. For a 1M solution, the peak corresponding to electrodeposition occurred almost immediately after the initial double-layer current, with a t_m value of only 990s. Increasing the concentration increases t_m to 3500s at 3M, 9663s at 5M and 8027s at 7M. A similar pattern for t_m vs. concentration was observed at 2.05V (Fig. 6-2b). To estimate the error involved in this

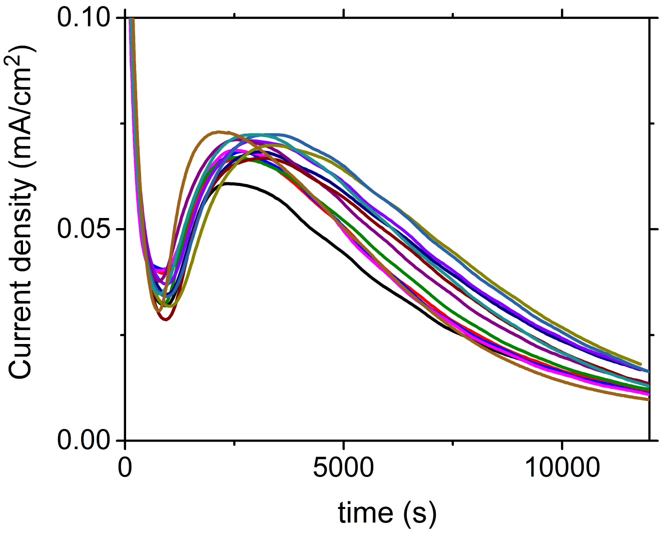

Figure 6-4: Current vs. time plots for Li_2S electrodeposition from 3M sulfur solutions, onto untreated carbon cloth, at 2.07V. Standard deviation for the time of current peak was 354s.

type of measurement, the 3M (2.07V) experiment was performed 13 times (Figure 6-4), and a standard deviation of 354s for t_m was obtained. We assumed a similar error of 10.1% of t_m would be present in measurements at other concentrations. The capacities obtained from Li_2S electrodeposition were approximately 270 mAh/g at 1M, 250 mAh/g at 3M, and 440 mAh/g at both 5M and 7M. This is considerably less than the theoretical capacity of 1250 mAh/g that would result from full conversion of polysulfides to Li_2S. That is, the current decay is due to passivation of the carbon surface and not depletion of sulfur. The N_0k^2 rate constants calculated from these values are plotted vs. sulfur concentration in Fig. 6-2d. The value of N_0 at 7M is almost two orders of magnitude lower than that at 1M. If both nucleation and growth are inhibited by the same factor, then N_0k^2 and k at 7M are only 25% of their values at 1M. Because of the very high concentration of polysulfide ions, ion pairing and formation of polysulfide clusters may inhibit redox reactions involving polysulfides[141]. Reductions in reaction rate constants at high polysulfide concentrations have been observed previously[70]. Also, as expected, N_0k^2 was higher at 2.05V than 2.07V, i.e. at a greater overpotential. A small increase in N_0k^2 was observed from 5M to 7M.

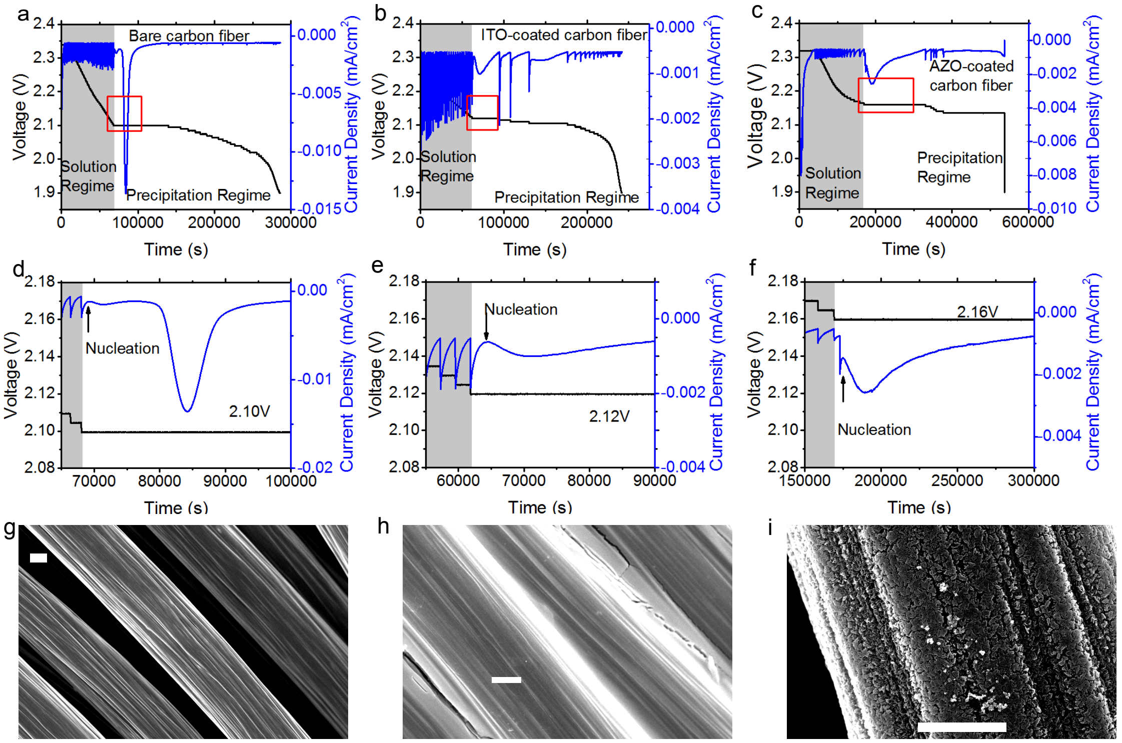

Figure 6-5: (a-f) Current and voltage vs. time plots for PITT experiments for reduction of polysulfide solutions on bare carbon fiber (a,d), ITO-coated carbon (b,e), and AZO-coated carbon (c,f). d-f represent the portions in a-c that are highlighted in red. The large current peak in each plot represents the nucleation and growth of Li_2S. (g-i) Scanning electron microscope images of bare (g), ITO-coated (h), and AZO-coated (i) carbon fiber. All scale bars are 2 μm

This may be because 7M is near the solubility limit of polysulfides, and that some sulfide may have precipitated chemically (rather than electrochemically), forming nuclei for electrodeposition.

The potentiostatic intermittent titration technique (PITT) was used to determine the critical overpotential needed to initiate nucleation of Li_2S on a given surface, with the results shown in Figs. 6-5 and 6-7. In Fig. 6-5, results are shown for carbon fiber cloth as the working electrode, either as-received (a,d,g) or coated with ITO (b,e,h) or AZO (c,f,i) via a sol-gel process, used with 1M polysulfide solution. The uncoated carbon fiber cloth consists of relatively smooth fibers, as does the ITO-coated carbon. The AZO coating is rougher and consists of <100 nm nanoparticles. SEM images of all three are shown in Fig. 6-5. Lower-magnification images are provided in Fig.

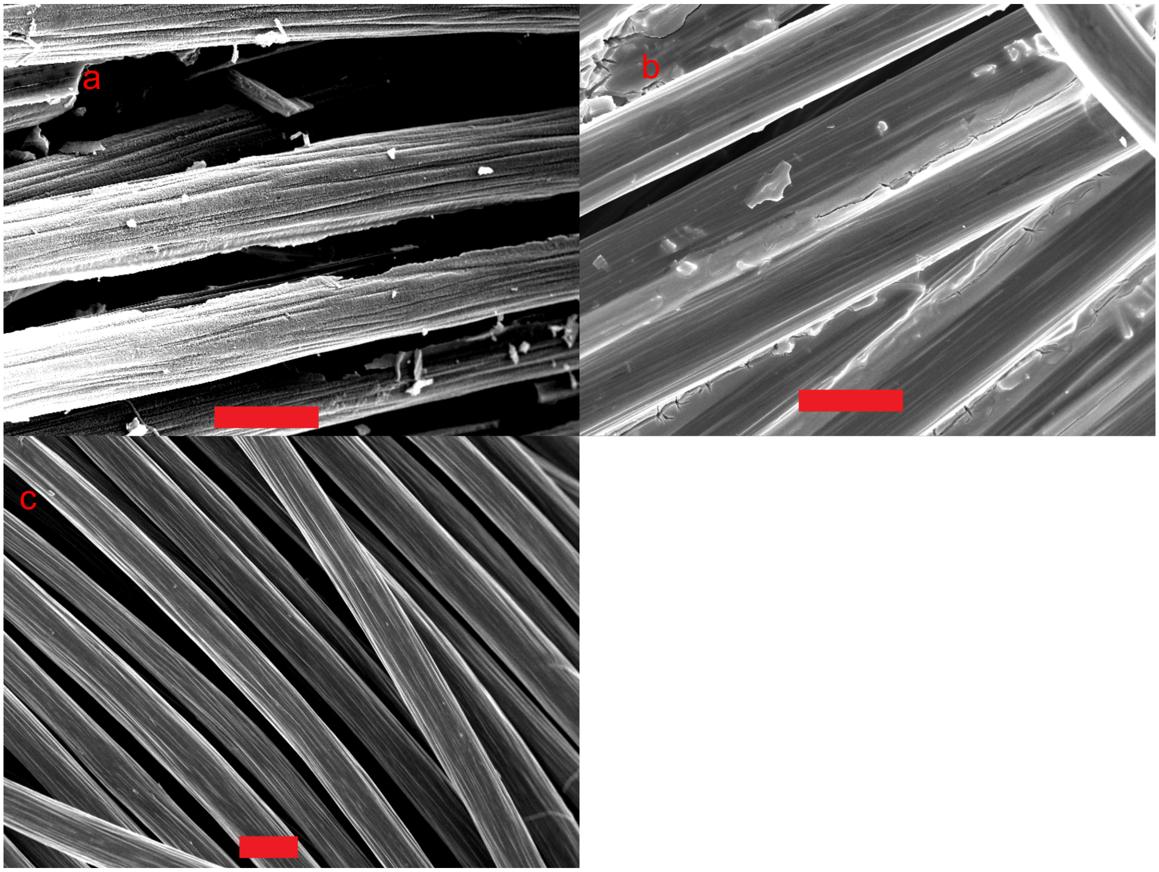

Figure 6-6: SEM images of AZO-coated fiber (upper left), ITO-coated fiber (upper right), and as-received carbon fiber cloth (bottom). All scale bars are 10 μm.

S3. ITO and AZO are conductive oxides which are commonly used as transparent electrodes in optoelectronic devices, and which have more recently been proposed as conductive additives for Li-S batteries[17, 19]. Previous studies have found polar hosts, such as metal oxide, to bind more strongly to lithium sulfide than does non-polar carbon. Therefore, ITO and AZO would be expected to have lower energy barriers and smaller overpotentials for nucleation. From the open circuit potential, the working electrode potential was lowered in 5mV steps, with the potential being stepped each time the current fell below a cutoff corresponding to C/400 rate. In the solution regime (between 2.3 V and 2.16 V, corresponding to the shaded regions in Fig. 6-5), current decreased monotonically during each step, which is expected from a process with no phase change, i.e. the reduction of soluble polysulfides to lower-order soluble polysulfides. The first potential step in which a current maximum indicating nucleation and growth appears corresponds to the minimum overpotential that can initiate nucleation, and the beginning of the precipitation regime. Carbon required the greatest overpotential (90 mV) followed by ITO (70 mV) and AZO (30 mV).

Based on these results alone, it is not clear whether the lower overpotential for the AZO-coated carbon is due to its higher surface area compared to the bare carbon fiber, or to the presence of AZO. Therefore, PITT experiments were also conducted on suspension-based polysulfide electrodes with identical surface areas of carbon black and AZO nanoparticles. The suspension electrode approach, first shown in Ref.[46], uses a continuously percolating network of conductive particles to create a "current collector" of high surface area and extending throughout the volume of the polysulfide solution. Using the same carbon and AZO surface area, and the same current cutoff of C/400, a lower overpotential was again observed for AZO (20 mV) than for carbon black (55mV), as shown in Fig. 6-7. This comparison shows that it is the AZO that reduces the overpotential. Note that lower overpotentials were observed for both suspensions compared to their carbon fiber counterparts (uncoated and AZO coated). This is attributed to the fact that both nanoparticle suspensions have much greater surface area, by a factor of 200, than the carbon cloth. Therefore, the actual current density per area of solid conductor at the PITT cutoff current density is

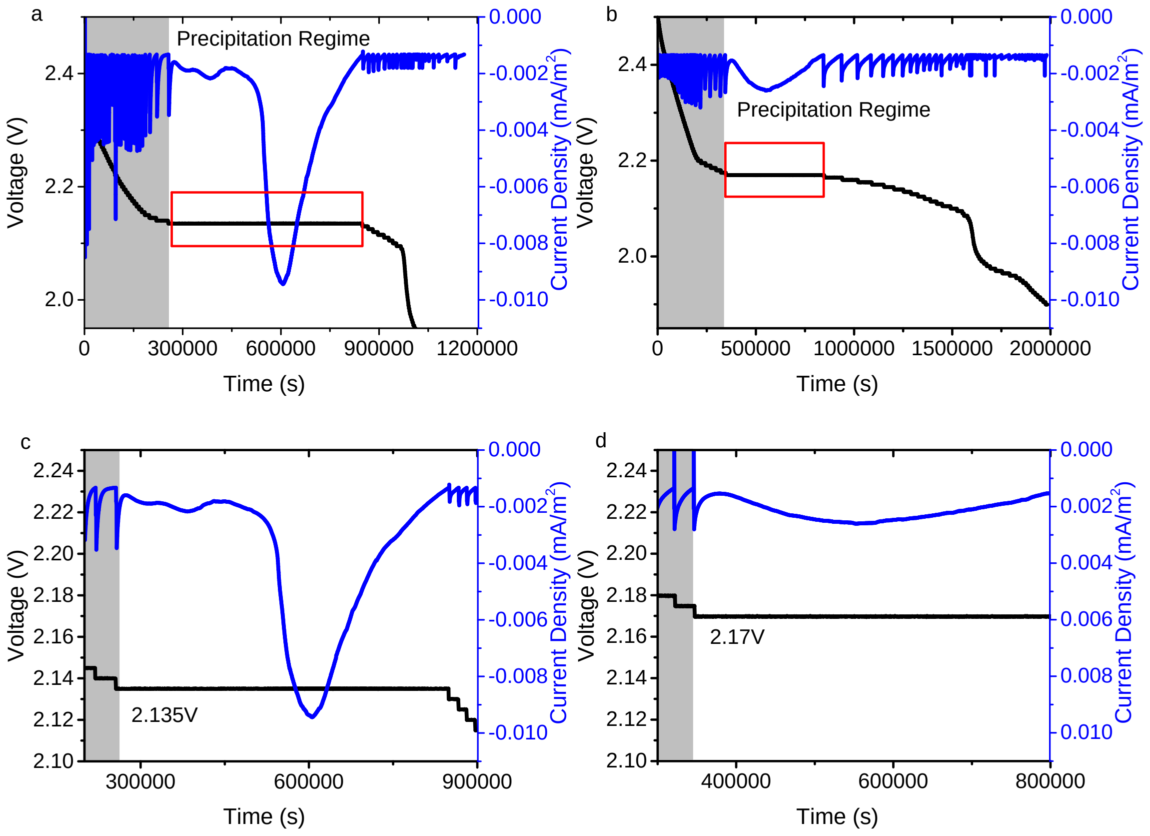

Figure 6-7: Current and voltage vs. time plots for PITT experiments for reduction of 1 mol S/l polysulfide solution on suspended carbon black (a,c) and AZO nanoparticles (b,d).

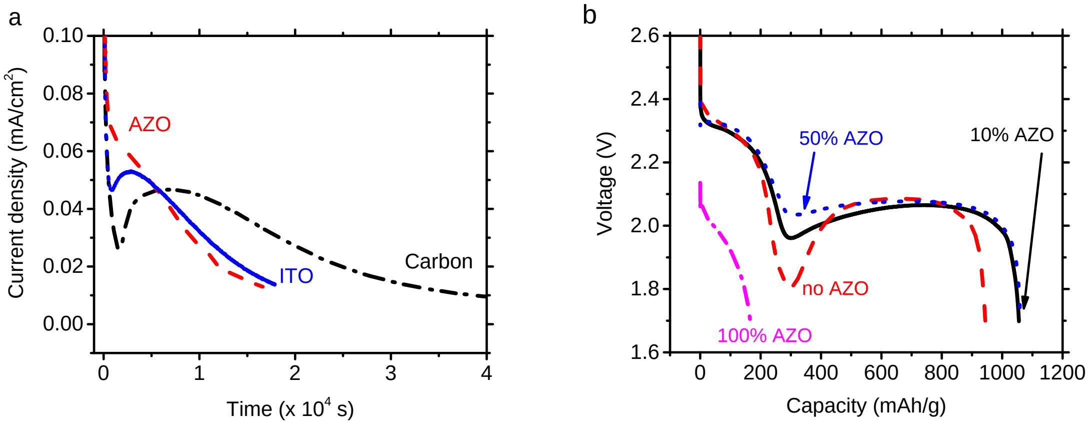

Figure 6-8: (a) Potentiostatic (2.07 V) current density vs. time data for electrodeposition of Li_2S from 5M polysulfide solution onto carbon and AZO and ITO coated carbon. (b) Galvanostatic discharge curves for Li-S cells with a S/C cathode and a S/C/AZO cathode (solid, black). The latter exhibits a significantly lower nucleation overpotential, observed at 300 mAh/g capacity, as well as higher total capacity.

also lower by about the same factor of 200. This experiment confirms that using a conductive nanoparticle suspension instead of carbon fiber as the electrode increases the electrochemically active surface area and reduces polarization, a result we first showed in a previous paper[46].

To quantify the effects of oxide coating on the reaction rate constant, N_0k^2, under electrolyte-lean conditions, potentiostatic electrodeposition experiments were then performed at 2.07V using 5M polysulfide solutions and the coated carbon fiber electrodes (Fig. 6-5a). Both coated electrodes yielded faster kinetics than the uncoated one, the increase in N_0k^2 being about a factor of 3.1 and 2.5 for AZO and ITO, respectively (Fig. 6-2d). In fact, the current minimum that is characteristic of a nucleation barrier disappeared entirely for the AZO-coated electrode. We attribute the faster kinetics of electrodeposition on AZO compared to ITO, as well as the lower overpotential required for nucleation, to stronger binding between AZO and Li_2S.

Further investigating the effects of AZO as a nucleation promoter, experiments were conducted under galvanostatic discharge conditions. Cathodes were prepared which were similar to the S/C composite cathodes tested above, but with 10%, 50%, or 100% of the Super-P carbon being replaced with the same volume of AZO nanoparticles. Cells containing such cathodes were discharged under identical conditions to those in Fig. 6-1, and at the same 4.2 ml/g E/S ratio (cf. middle curve in Fig. 6-1). The resulting discharge curves, along with the one for the original cathode without AZO, are shown in Figure 6b. Nucleation overpotentials of 230 mV and 155 mV were respectively observed for the 10% and 50% samples, compared to 380 mV in the original discharge curve. Moreover, specific capacity increased from to 945 mAh/g to 1055 mAh/g and 1060 mAh/g respectively. The lower initial overpotential for the AZO/C composite cathodes likely causes Li_2S to deposit preferentially on isolated AZO particles while reducing the number of nuclei forming on carbon, resulting in electrodeposition which is dominated by growth from AZO sites rather than nucleation of Li_2S islands on carbon. A reduced nuclei density has been shown in our previous work to be associated with delayed passivation and fewer, larger Li_2S particles and more Li_2S deposited on a given electrode surface area[80]. Figure 6b shows that replacement of all carbon with AZO, on the other hand, leads to a very large overpotential (over 250 mV greater than carbon-containing electrodes) during the sulfur dissolution step. Moreover, capacity decreased to less than 200 mAh/g, even less than the capacity expected from sulfur dissolution. We believe that excessively strong binding between substrate and polysulfide may have negative effects in this instance, namely the difficulty of desorbing polysulfide reaction products from the surface during the S_8 dissolution step. Thus a hybrid cathode containing both carbon and oxide can offer lower polarization than one containing carbon or oxide alone.

Cycle life data for both S/C and S/C/AZO composite cathodes is shown in Fig. 6-9. A slight improvement in cycle life was observed for AZO-containing electrodes, although cycle life for both types of electrode was quite poor, with most of the initial capacity lost within 20 cycles. However, these electrodes were not designed for maximizing cycle life, but only to demonstrate the effects of different surfaces on polarization. Hence, standard methods for improving cycle life via polysulfide encapsulation were not used, and cells suffered from degradation via typical mechanisms such as polysulfide shuttling.

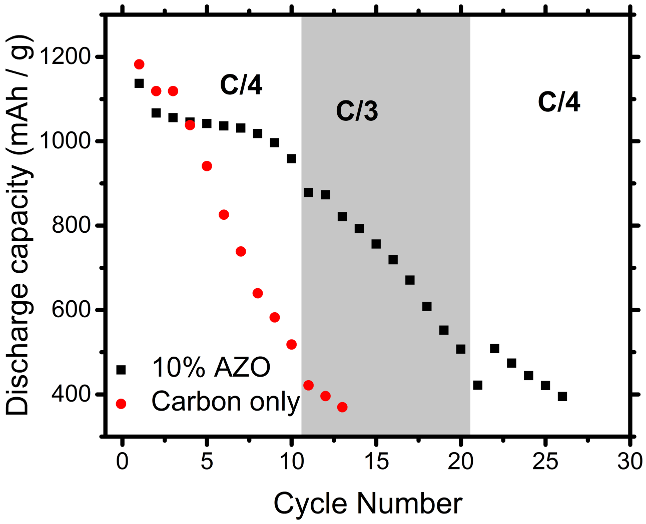

Figure 6-9: Discharge capacity vs. cycle number for Li-S batteries with S/C and S/C/AZO cathodes. All cycles are performed at C/4, except for cycles 11-20, which are at C/3.

6.4 Conclusions

The kinetics of lithium sulfide electrodeposition on carbon and metal oxide surfaces from polysulfide solutions of various concentrations were measured using chronoamperometric tests and a variety of electrode configurations. Electrodeposition was found to be significantly slower at high polysulfide concentrations for a given deposition substrate. Because electrolyte/sulfur ratio affects the polysulfide concentration reached in the electrolyte during use, we believe that the dependence of precipitation kinetics on dissolved sulfur concentration is responsible for sluggish Li_2S electrodeposition during cycling of Li-S batteries. Indeed, we observed significantly larger nucleation barriers in our model Li-S cells when cycling them under electrolyte-lean conditions. Promoting the electrodeposition of Li_2S is therefore an important consideration when designing electrolyte-lean Li-S batteries. ITO and AZO surfaces were found to improve nucleation and growth performance at high polysulfide concentrations; AZO may be preferred due to its lower cost. The addition of AZO to sulfur/carbon composite cathodes was found to reduce polarization and increase capacity under galvanostatic cycling conditions. These improvements were observed both for stationary carbon fiber current collectors and for conductive suspensions in which a percolating network of carbon forms a spatially-extended current collector.

Chapter 7

Conclusions

The lithium-sulfur system is of great interest because of its potential to offer significant improvements over existing batteries in terms of both energy density and cost and thereby enable the adoption of electric vehicles, as well as large-scale energy storage for grid applications. However, rate capability remains a major challenge to the commercial viability of Li-S batteries. In the preceding chapters, we used solutions of lithium polysulfide intermediates to study rate limitations in Li-S batteries in order to inform rational design of high-performance lithium-sulfur batteries.

In Chapter 2, we demonstrated, for the first time, a flow battery based on Li-S chemistry which achieved high energy density and which used low-cost active materials. High capacity and efficient cycling required a novel architecture based on a percolating network of high-surface area carbon nanoparticles, rather than the more conventional approach of using a low-surface area carbon fiber current collector. This demonstrated the need for high exchange current density, the challenges of the precipitation of insulating Li_2S, and difficulties of obtaining high performance at high polysulfide concentrations, all of which were investigated in later chapters.

In Chapter 3, we conducted a systematic study of the rate limiting mechanisms in the solution regime—the ionic conductivity of polysulfide solutions and exchange current density of redox within the solution regime. Exchange current density exhibited a similar solvent dependence, which was attributed to stronger binding between Li^+ ions and solvent molecules, a conclusion supported by ab initio molecular dynamics calculations performed by our collaborators. Ionic conductivity decreased sharply with size of glyme solvent molecule and with polysulfide concentration, both of which increase solution viscosity. Exchange current density was Ionic conductivity was found to be rate limiting in the solution regime for at least one cell architecture.

In Chapter 4, we developed a method to quantify using potentiostatic methods the kinetics of electrodeposition of Li_2S from polysulfide solutions, a crucial step which is both slow and responsible for the vast majority of the theoretical capacity of the Li-S battery. Electrodeposition of the insulating material was found to proceed by a nucleation and 2-dimensional island growth process which can be well modeled using the theory of Bewick, Fleischmann, and Thirsk, itself derived from the Johnson-Mehl-Avrami-Kolmogoroff model of nucleation and growth. Kinetics were found to vary with electrolyte solvent in a trend and magnitude similar to that found in chapter 3 for exchange current density, suggesting that the cause may be of a similar nature. The growth of existing particles was found to require a lower overpotential than nucleation of new ones, a finding which may explain differences in Li_2S morphology at different discharge rates.

In Chapter 5, we developed a model to describe electrodeposition of Li_2S in the presence of a redox mediator. The redox mediator provides a separate parallel path for reduction of polysulfide far from the conductive substrate, allowing 3-dimensional growth of the precipitate while delaying passivation of the substrate surface.

In Chapter 6, we further extend our work on Li_2S electrodeposition by examining the effects of polysulfide concentration and deposition substrate. Nucleation and growth of Li_2S become substantially slower at high polysulfide concentrations, which correspond to low electrolyte/sulfur (E/S) ratios. This helps to explain the poor cycling performance and high polarization that is observed under the electrolyte-lean conditions necessary for high energy density at the system level. Two metal oxides, indium tin oxide and aluminum-doped zinc oxide, were found to lower substantially the overpotential needed to initiate nucleation. Aluminum-doped zinc oxide in particular was found to reduce polarization and improve performance when used to replace a portion of the carbon in a typical sulfur-carbon composite cathode.

Hence, we have gained a number of insights into rate limitations in Li-S batteries. These conclusions can be used to establish design rules for high-capacity, high-rate capability Li-S batteries via the tuning of electrolyte formulations and conductive additives.

7.1 Future Work

Solution resistivity is a significant contributor to polarization in Chapter 3 and will likely be one in the thick, high areal density (i.e. high mass of sulfur per unit electrode area) cathodes which are necessary for high system-level energy density[3]. Aside from developing new electrolyte formulations with high conductivity, the effective electrolyte resistivity can be reduced by reducing the tortuosity of the porous cathode, a technique which has been successfully used for Li-ion batteries[33].

At a smaller length scale, the arrangement of sulfur on the carbon surface may have significant effects on performance. At low electrolyte/sulfur ratios, we expect that a portion of the sulfur remains solid at all times. Because reaction kinetics, especially for electrodeposition, tend to be quite sluggish, as much carbon surface area as possible must be kept free. To maximize this surface area, it may be useful to manipulate the initial sulfur morphology into discrete particles, rather than a film-like morphology that coats all of the carbon. The latter is a typical morphology, since cathodes are usually made via melt-diffusion which causes the sulfur to wet the carbon.

Bibliography

[1] B Dunn, H Kamath, and J M Tarascon. Electrical Energy Storage for the Grid: A Battery of Choices. *Science (80-.).*, 334(6058):928–935, 2011.

[2] Z. Yang, J. Zhang, M. C. W. Kintner-Meyer, X. Lu, D. Choi, J. P. Lemmon, and J. Liu. Electrochemical energy storage for green grid. *Chem. Rev.*, 111(5):3577–613, 2011.

[3] D. Eroglu, K. R. Zavadil, and K. G. Gallagher. Critical Link between Materials Chemistry and Cell-Level Design for High Energy Density and Low Cost Lithium-Sulfur Transportation Battery. *J. Electrochem. Soc.*, 162(6):A982–A990, 2015.

[4] Björn Nykvist and Måns Nilsson. Rapidly falling costs of battery packs for electric vehicles. *Nat. Clim. Chang.*, 5(4):329–332, 2015.

[5] David T. Danielson. EV everywhere GRAND CHALLENGE road to success, 2014.

[6] Uday Kasavajjula, Chunsheng Wang, and A. John Appleby. Nano- and bulk-silicon-based insertion anodes for lithium-ion secondary cells. *J. Power Sources*, 163(2):1003–1039, 2007.

[7] Wu Xu, Jiulin Wang, Fei Ding, Xilin Chen, Eduard Nasybulin, Yaohui Zhang, and Ji-Guang Zhang. Lithium metal anodes for rechargeable batteries. *Energy Environ. Sci.*, 7(2):513–537, 2014.

[8] Huilin Pan, Yong-Sheng Hu, and Liquan Chen. Room-temperature stationary sodium-ion batteries for large-scale electric energy storage. *Energy Environ. Sci.*, 6(8):2338, 2013.

[9] Michael D. Slater, Donghan Kim, Eungje Lee, and Christopher S. Johnson. Sodium-ion batteries. *Adv. Funct. Mater.*, 23(8):947–958, 2013.

[10] Partha Saha, Moni Kanchan Datta, Oleg I. Velikokhatnyi, Ayyakkannu Manivannan, David Alman, and Prashant N. Kumta. Rechargeable magnesium battery: Current status and key challenges for the future. *Prog. Mater. Sci.*, 66:1–86, 2014.

[11] Peter G. Bruce, Stefan A. Freunberger, Laurence J. Hardwick, and Jean-Marie Tarascon. Li-O2 and Li-S batteries with high energy storage. *Nat. Mater.*, 11(December 2011):19–30, 2012.

[12] Scott Evers and Linda F Nazar. New approaches for high energy density lithium–sulfur battery cathodes. *Acc. Chem. Res.*, 46(5):1135–1143, 2013.

[13] Arumugam Manthiram, Yongzhu Fu, and Yu-Sheng Su. Challenges and prospects of lithium–sulfur batteries. *Acc. Chem. Res.*, 46(5):1125–1134, 2013.

[14] Joyce A Ober. Mineral commodity summaries 2017. Technical report, US Geological Survey, 2017.

[15] Jan Brückner, Sören Thieme, Falko Böttger-Hiller, Ingolf Bauer, Hannah Tamara Grossmann, Patrick Strubel, Holger Althues, Stefan Spange, and Stefan Kaskel. Carbon-Based Anodes for Lithium Sulfur Full Cells with High Cycle Stability. *Adv. Funct. Mater.*, 24(9):1616–3028, 2014.

[16] Quan Pang, Dipan Kundu, Marine Cuisinier, and L F Nazar. Surface-enhanced redox chemistry of polysulphides on a metallic and polar host for lithium-sulphur batteries. *Nat. Commun.*, 5:4759, 2014.

[17] Hongbin Yao, Guangyuan Zheng, Po-Chun Hsu, Desheng Kong, Judy J Cha, Weiyang Li, Zhi Wei Seh, Matthew T McDowell, Kai Yan, Zheng Liang, Vijay Kris Narasimhan, and Yi Cui. Improving lithium-sulphur batteries through spatial control of sulphur species deposition on a hybrid electrode surface. *Nat. Commun.*, 5:3943, 2014.

[18] Zhe Yuan, Hong Jie Peng, Ting Zheng Hou, Jia Qi Huang, Cheng Meng Chen, Dai Wei Wang, Xin Bing Cheng, Fei Wei, and Qiang Zhang. Powering Lithium-Sulfur Battery Performance by Propelling Polysulfide Redox at Sulfiphilic Hosts. *Nano Lett.*, 16(1):519–527, 2016.

[19] Xingxing Gu, Chuan-jia Tong, Bo Wen, Li-min Liu, Chao Lai, and Shanqing Zhang. Ball-milling synthesis of ZnO@sulphur/carbon nanotubes and Ni(OH)2@sulphur/carbon nanotubes composites for high-performance lithium-sulphur batteries. *Electrochim. Acta*, 196:369–376, 2016.

[20] Rui Xu, Jun Lu, and Khalil Amine. Progress in Mechanistic Understanding and Characterization Techniques of Li-S Batteries. *Adv. Energy Mater.*, 2015.

[21] Marine Cuisinier, Pierre-Etienne Cabelguen, Scott Evers, Guang He, Mason Kolbeck, Arnd Garsuch, Trudy Bolin, Mahalingam Balasubramanian, and Linda F. Nazar. Sulfur Speciation in Li-S Batteries Determined by Operando X-ray Absorption Spectroscopy. *J. Phys. Chem. Lett.*, 4(19):3227–3232, 2013.

[22] Xiulei Ji, Kyu Tae Lee, and Linda F Nazar. A highly ordered nanostructured carbon–sulphur cathode for lithium–sulphur batteries. *Nat. Mater.*, 8(6):500–506, 2009.

[23] K Zhang, Z Hu, and J Chen. Functional porous carbon-based composite electrode materials for lithium secondary batteries. *J. Energy Chem.*, 22:214–225, 2013.

[24] X Liang, A Garsuch, and L F Nazar. Sulfur Cathodes Based on Conductive MXene Nanosheets for High-Performance Lithium-Sulfur Batteries. *Angew. Chem., Int. Ed.*, 54:3907–3911, 2015.

[25] J Wang, J Yang, C Wan, K Du, J Xie, and N Xu. Sulfur Composite Cathode Materials for Rechargeable Lithium Batteries. *Adv. Funct. Mater.*, 13:487–492, 2003.

[26] I. Bauer, S. Thieme, J. Brückner, H. Althues, and S. Kaskel. Reduced polysulfide shuttle in lithiumâĂŞsulfur batteries using Nafion-based separators. *J. Power Sources*, 251:417–422, apr 2014.

[27] Changyi Li, Ashleigh L. Ward, Sean E. Doris, Tod A. Pascal, David Prendergast, and Brett A. Helms. Polysulfide-Blocking Microporous Polymer Membrane Tailored for Hybrid Li-Sulfur Flow Batteries. *Nano Lett.*, 15(9):5724–5729, 2015.

[28] Doron Aurbach, Elad Pollak, Ran Elazari, Gregory Salitra, C. Scordilis Kelley, and John Affinito. On the Surface Chemical Aspects of Very High Energy Density, Rechargeable Li-Sulfur Batteries. *J. Electrochem. Soc.*, 156(8):A694–A702, 2009.

[29] J. Zheng, D. Lv, M. Gu, C. Wang, J.-G. Zhang, J. Liu, and J. Xiao. How to Obtain Reproducible Results for Lithium Sulfur Batteries? *J. Electrochem. Soc.*, 160(11):A2288–A2292, 2013.

[30] Long Qie and Arumugam Manthiram. A Facile Layer-by-Layer Approach for High-Areal-Capacity Sulfur Cathodes. *Adv. Mater.*, 27(10):1694–700, 2015.

[31] Fei Ding, Wu Xu, Xilin Chen, Jian Zhang, Yuyan Shao, Mark H. Engelhard, Yaohui Zhang, Thomas A. Blake, Gordon L. Graff, Xingjiang Liu, and Ji Guang Zhang. Effects of cesium cations in lithium deposition via self-healing electrostatic shield mechanism. *J. Phys. Chem. C*, 118(8):4043–4049, 2014.

[32] Xiaogang Han, Yunhui Gong, Kun (Kelvin) Fu, Xingfeng He, Gregory T. Hitz, Jiaqi Dai, Alex Pearse, Boyang Liu, Howard Wang, Gary Rubloff, Yifei Mo, Venkataraman Thangadurai, Eric D. Wachsman, and Liangbing Hu. Negating interfacial impedance in garnet-based solid-state Li metal batteries. *Nat. Mater.*, 16(May), 2016.

[33] Jonathan Sander, Randall M Erb, Linsen Li, Anvesh Gurijala, and Yet-Ming Chiang. High-performance battery electrodes via magnetic templating. *Nat. Energy*, 1:16099, 2016.

[34] Martin Ebner, Ding-Wen Chung, R Edwin Garc\'\ia, and Vanessa Wood. Tortuosity Anisotropy in Lithium-Ion Battery Electrodes. *Adv. Energy Mater.*, 4(5), 2014.

[35] Betar M. Gallant, David G. Kwabi, Robert R. Mitchell, Jigang Zhou, Carl V. Thompson, and Yang Shao-Horn. Influence of Li2O2 morphology on oxygen reduction and evolution kinetics in Li-O2 batteries. *Energy Environ. Sci.*, 6(8):2518, 2013.

[36] Robert R Mitchell, Betar M Gallant, Yang Shao-horn, and Carl V Thompson. Mechanisms of Morphological Evolution of Li 2 O 2 Particles during Electrochemical Growth. *J. Phys. Chem. Lett.*, 4(7):1060–1064, 2013.

[37] Lee Johnson, Chunmei Li, Zheng Liu, Yuhui Chen, Stefan a Freunberger, Praveen C Ashok, Bavishna B Praveen, Kishan Dholakia, Jean-Marie Tarascon, and Peter G Bruce. The role of LiO2 solubility in O2 reduction in aprotic solvents and its consequences for Li-O2 batteries. *Nat. Chem.*, 6(12):1091–9, 2014.

[38] Sampson Lau and Lynden A Archer. Nucleation and Growth of Lithium Peroxide in the Li-O2 Battery. *Nano Lett.*, 15(9):5995–6002, 2015.

[39] Melvin Avrami. Kinetics of Phase Change. I General Theory. *J. Chem. Phys.*, 7(12):1103, 1939.

[40] Melvin Avrami. Kinetics of Phase Change. II Transformation-Time Relations for Random Distribution of Nuclei. *J. Chem. Phys.*, 8(2):212, 1940.

[41] Gamini Gunawardena, Graham Hills, Irene Montenegro, and Benjamin Scharifker. Electrochemical nucleation. *J. Electroanal. Chem.*, 138(2):225–239, 1982.

[42] Benjamin Scharifker and Graham Hills. Theoretical and Experimental Studies of Multiple Nucleation. *Electrochim. Acta*, 28(7):879–889, 1983.

[43] Luc Heerman and Anthony Tarallo. Theory of the chronoamperometric transient for electrochemical nucleation with diffusion-controlled growth. *J. Electroanal. Chem.*, 470(1):70–76, 1999.

[44] R.D. Armstrong, M. Fleischmann, and H. R. Thirsk. The Anodic Behaviour of Mercury in Hydroxide Ion Solutions. *J. Electroanal. Chem.*, 11:208–223, 1966.

[45] A. Bewick, M. Fleischmann, and H. R. Thirsk. Kinetics of the electrocrystallization of thin films of calomel. *Trans. Faraday Soc.*, 58:2200, 1962.

[46] Frank Y Fan, William H Woodford, Zheng Li, Nir Baram, Kyle C Smith, Ahmed Helal, Gareth H Mckinley, W Craig Carter, and Yet-ming Chiang. Polysulfide Flow Batteries Enabled by Percolating Nanoscale Conductor Networks. *Nano Lett.*, 14:2210–2218, 2014.

[47] Adam Z. Weber, Matthew M. Mench, Jeremy P. Meyers, Philip N. Ross, Jeffrey T. Gostick, and Qinghua Liu. Redox flow batteries: a review. *J. Appl. Electrochem.*, 41(10):1137–1164, 2011.

[48] Liyu Li, Soowhan Kim, Wei Wang, M. Vijayakumar, Zimin Nie, Baowei Chen, Jianlu Zhang, Guanguang Xia, Jianzhi Hu, Gordon Graff, Jun Liu, and Zhenguo Yang. A Stable Vanadium Redox-Flow Battery with High Energy Density for Large-Scale Energy Storage. *Adv. Energy Mater.*, 1(3):394–400, 2011.

[49] M. Skyllas-Kazacos, G. Kazacos, G. Poon, and H. Verseema. Recent advances with UNSW vanadium-based redox flow batteries. *Int. J. Energy Res.*, 34(2):182–189, 2010.

[50] Mihai Duduta, Bryan Ho, Vanessa C. Wood, Pimpa Limthongkul, Victor E. Brunini, W. Craig Carter, and Yet-Ming Chiang. Semi-Solid Lithium Rechargeable Flow Battery. *Adv. Energy Mater.*, 1(4):511–516, 2011.

[51] S Hamelet, T Tzedakis, J B Leriche, S Sailler, D Larcher, P L Taberna, P Simon, and J M Tarascon. Non-Aqueous Li-Based Redox Flow Batteries. *J Electrochem Soc*, 159(8):A1360—-A1367, 2012.

[52] Zheng Li, Kyle C Smith, Yajie Dong, Nir Baram, Frank Y Fan, Jing Xie, Pimpa Limthongkul, W Craig Carter, and Yet-Ming Chiang. Aqueous semi-solid flow cell: demonstration and analysis. *Phys. Chem. Chem. Phys.*, 15(38):15833–9, 2013.

[53] Yuan Yang, Guangyuan Zheng, and Yi Cui. A membrane-free lithium/polysulfide semi-liquid battery for large-scale energy storage. *Energy Environ. Sci.*, 6(5):1552, 2013.

[54] Rezan Demir-Cakan, Mathieu Morcrette, Aurélie Guéguen, Rémi Dedryvère, and Jean-Marie Tarascon. Li-S batteries: simple approaches for superior performance. *Energy Environ. Sci.*, 6(1):176, 2013.

[55] Fikile R. Brushett, John T. Vaughey, and Andrew N. Jansen. An all-organic non-aqueous lithium-ion redox flow battery. *Adv. Energy Mater.*, 2(11):1390–1396, 2012.

[56] Harry D Pratt III, Alyssa J Rose, Chad L Staiger, David Ingersoll, and Travis M Anderson. Synthesis and characterization of ionic liquids containing copper, manganese, or zinc coordination cations. *Dalt. Trans.*, 40(43):11396, 2011.

[57] Richard Van Noorden. Sulphur back in vogue for batteries. *Nature*, 498:416–417, 2013.

[58] Yuriy V. Mikhaylik and James R. Akridge. Polysulfide shuttle study in the Li/S battery system. *J. Electrochem. Soc.*, 151(11):A1969, 2004.

[59] Y.V. Mikhaylik. Electrolytes for lithium sulfur cells. U.S. Patent 7,352,680, 2008.

[60] G Ovarlez, S Cohen-Addad, K Krishan, J Goyon, and P Coussot. On the existence of a simple yield stress fluid behavior. *J. Nonnewton. Fluid Mech.*, 193:68–79, 2013.

[61] A N N Yoshimura and Robert K Prud'Homme. Wall Slip Corrections for Couette Disk Viscometers and Parallel. *J. Nonnewton. Fluid Mech.*, 32(l):53–67, 1988.

[62] Chinedum O. Osuji, Chanjoong Kim, and David a. Weitz. Shear thickening and scaling of the elastic modulus in a fractal colloidal system with attractive interactions. *Phys. Rev. E*, 77(6):060402, 2008.

[63] V. Trappe and D. Weitz. Scaling of the viscoelasticity of weakly attractive particles. *Phys. Rev. Lett.*, 85(2):449–52, 2000.

[64] R.B Bird, G.C. Dal, and B.J. Yarusso. The rheology and flow of viscoplastic materials. *Rev. Chem. Eng*, 1(1):1–70, 1982.

[65] Dominic Bresser, Stefano Passerini, and Bruno Scrosati. Recent progress and remaining challenges in sulfur-based lithium secondary batteries–a review. *Chem. Commun. (Camb).*, 49(90):10545–62, 2013.

[66] B. Zhang, X. Qin, G. R. Li, and X. P. Gao. Enhancement of long stability of sulfur cathode by encapsulating sulfur into micropores of carbon spheres. *Energy Environ. Sci.*, 3(10):1531, 2010.

[67] Karthikeyan Kumaresan, Yuriy Mikhaylik, and Ralph E White. A mathematical model for a lithium-sulfur cell. *J. Electrochem. Soc.*, 155(8):A576–A582, 2008.

[68] Victor E. Brunini, Yet-Ming Chiang, and W. Craig Carter. Modeling the hydrodynamic and electrochemical efficiency of semi-solid flow batteries. *Electrochim. Acta*, 69:301–307, 2012.

[69] K. C. Smith, Y.-M. Chiang, and W. Craig Carter. Maximizing Energetic Efficiency in Flow Batteries Utilizing Non-Newtonian Fluids. *J. Electrochem. Soc.*, 161(4):A486–A496, 2014.

[70] Frank Y. Fan, Menghsuan Sam Pan, Kah Chun Lau, Rajeev S Assary, William H. Woodford, Larry A Curtiss, W. Craig Carter, and Yet-Ming Chiang. Solvent Effects on Polysulfide Redox Kinetics and Ionic Conductivity in Lithium-Sulfur Batteries. *J. Electrochem. Soc.*, 2016.

[71] Monica Marinescu, Teng Zhang, and Gregory J. Offer. A zero dimensional model of lithium-sulfur batteries during charge and discharge. *Phys. Chem. Chem. Phys.*, 2015.

[72] David N. Fronczek and Wolfgang G. Bessler. Insight into lithium-sulfur batteries: Elementary kinetic modeling and impedance simulation. *J. Power Sources*, 244:183–188, 2013.

[73] J. P. Neidhardt, D. N. Fronczek, T. Jahnke, T. Danner, B. Horstmann, and W. G. Bessler. A flexible framework for modeling multiple solid, liquid and gaseous phases in batteries and fuel cells. *J. Electrochem. Soc.*, 159(9):A1528–A1542, 2012.

[74] Ing-feng Hu, Dale H. Karweik, and Theodore Kuwana. Activation and deactivation of glassey carbon electrodes. *J. Electroanal. Chem.*, 188:59–72, 1985.

[75] G Kresse and D Joubert. From ultrasoft pseudopotentials to the projector augmented-wave method. *Phys. Rev. B*, 59(3):1758–1775, jan 1999.

[76] G. Kresse and J. Furthmüller. Efficiency of ab-initio total energy calculations for metals and semiconductors using a plane-wave basis set. *Comput. Mater. Sci.*, 6(1):15–50, 1996.

[77] John P Perdew, Kieron Burke, and Matthias Ernzerhof. Generalized Gradient Approximation Made Simple. *Phys. Rev. Lett.*, 77(18):3865–3868, oct 1996.

[78] P E Blöchl. Projector augmented-wave method. *Phys. Rev. B*, 50(24):17953–17979, dec 1994.

[79] Stefan Grimme. Semiempirical GGA-type density functional constructed with a long-range dispersion correction. *J. Comput. Chem.*, 27(15):1787–1799, 2006.

[80] Frank Y. Fan, W. Craig Carter, and Yet-Ming Chiang. Mechanism and Kinetics of Li 2 S Precipitation in Lithium-Sulfur Batteries. *Adv. Mater.*, 27(35):5203–5209, 2015.

[81] H. Yamin and E. Peled. Electrochemistry of a nonaqueous lithium/sulfur cell. *J. Power Sources*, 9(3):281–287, 1983.

[82] William Woodford, Frank Fan, Nir Baram, Ahmed Helal, W Craig Carter, Yet-Ming Chiang, and Gareth McKinley. Charge Transfer and Transport Properties of Lithium Polysfulfide Solutions. In *Meet. Abstr.*, number 3, page 573. The Electrochemical Society, The Electrochemical Society, 2014.

[83] Xinwei Chen, Brandon J Hopkins, Ahmed Helal, Frank Y Fan, Kyle C Smith, Zheng Li, Alexander H Slocum, Gareth H Mckinley, W Craig Carter, and Yet-Ming Chiang. A low-dissipation, pumpless, gravity-induced flow battery. *Energy Environ. Sci.*, 9:1–11, 2016.

[84] Céline Barchasz, Jean-Claude Leprêtre, Sébastien Patoux, and Fannie Alloin. Electrochemical properties of ether-based electrolytes for lithium/sulfur rechargeable batteries. *Electrochim. Acta*, 89:737–743, 2013.

[85] Heng Liang Wu, Laura A. Huff, and Andrew A. Gewirth. In situ raman spectroscopy of sulfur speciation in lithium-sulfur batteries. *ACS Appl. Mater. Interfaces*, 7(3):1709–1719, 2015.

[86] Robert W. Balluffi, Samuel M. Allen, and W. Craig Carter. *Kinetics of Materials*. John Wiley {&} Sons, Hoboken, NJ, 2005.

[87] Lian Guo, Gerko Oskam, Aleksandar Radisic, Peter M Hoffmann, and Peter C Searson. Island growth in electrodeposition. *J. Phys. D. Appl. Phys.*, 44(44):443001, 2011.

[88] Yuan Yang, Guangyuan Zheng, and Yi Cui. Nanostructured sulfur cathodes. *Chem. Soc. Rev.*, 42:3018–3022, 2013.

[89] D Marmorstein, T.H Yu, K.a Striebel, F.R McLarnon, J Hou, and E.J Cairns. Electrochemical performance of lithium/sulfur cells with three different polymer electrolytes. *J. Power Sources*, 89(2):219–226, 2000.

[90] Quan Pang, Dipan Kundu, and Linda F. Nazar. A graphene-like metallic cathode host for long-life and high-loading lithiumâĂŞsulfur batteries. *Mater. Horiz.*, 3:130–136, 2016.

[91] Guangyuan Zheng, Qianfan Zhang, Judy J Cha, Yuan Yang, Weiyang Li, Zhi Wei Seh, and Yi Cui. Amphiphilic Surface Modification of Hollow Carbon Nanofibers for Improved Cycle Life of Lithium Sulfur Batteries. *Nano Lett.*, 13(3):1265–1270, 2013.

[92] Laura C. H. Gerber, Peter D. Frischmann, Frank Y. Fan, Sean E. Doris, Xiaohui Qu, Angelique M. Scheuermann, Kristin Persson, Yet-Ming Chiang, and Brett A. Helms. Three-Dimensional Growth of Li 2 S in Lithium-Sulfur Batteries Promoted by a Redox Mediator. *Nano Lett.*, page acs.nanolett.5b04189, 2015.

[93] A Manthiram, Y Fu, S.-H. Chung, C Zu, and Y.-S. Su. Rechargeable Lithium-Sulfur Batteries. *Chem. Rev.*, 114:11751–11787, 2014.

[94] Y.-X. Yin, S Xin, Y.-G. Guo, and L.-J. Wan. Lithium-sulfur batteries: electrochemistry, materials, and prospects. *Angew. Chem., Int. Ed.*, 52:13186–13200, 2013.

[95] R Black, B Adams, and L F Nazar. Non-Aqueous and Hybrid Li-O2 Batteries. *Adv. Energy Mater.*, 2:801–815, 2012.

[96] G Girishkumar, B McCloskey, A C Luntz, S Swanson, and W Wilcke. No Title. *J. Phys. Chem. Lett.*, 1:2193–2203, 2010.

[97] J Christensen, P Albertus, R S Sanchez-Carrera, T Lohmann, B Kozinsky, R Liedtke, J Ahmed, and A Kojic. No Title. *J. Electrochem. Soc.*, 159:R1–R30, 2012.

[98] K G Gallagher, S Goebel, T Greszler, M Mathias, W Oelerich, D Eroglu, and V Srinivasan. No Title. *Energy Environ. Sci.*, 7:1555–1563, 2014.

[99] R D Rauh, K M Abraham, G F Pearson, J K Surprenant, and S B Brummer. Lithium-dissolved sulfur battery with an organic electrolyte. *J Electrochem Soc*, 126(4):523–527, 1979.

[100] Yuan Yang, Guangyuan Zheng, Sumohan Misra, Johanna Nelson, Michael F Toney, and Yi Cui. High-capacity micrometer-sized Li 2S particles as cathode materials for advanced rechargeable lithium-ion batteries. *J. Am. Chem. Soc.*, 134(37):15387–15394, 2012.

[101] M D Radin and D J Siegel. Charge transport in lithium peroxide: relevance for rechargeable metal-air batteries. *Energy Environ. Sci.*, 6:2370–2379, 2013.

[102] V Viswanathan, K S Thygesen, J S Hummelshøj, J K Nørskov, G Girishkumar, B D McCloskey, and A C Luntz. Electrical conductivity in Li2O2 and its role in determining capacity limitations in non-aqueous Li-O2 batteries. *J. Chem. Phys.*, 135:214704–214710, 2011.

[103] P Albertus, G Girishkumar, B McCloskey, R S Sánchez-Carrera, B Kozinsky, J Christensen, and A C Luntz. Identifying Capacity Limitations in the Li/Oxygen Battery Using Experiments and Modeling. *J. Electrochem. Soc.*, 158:A343–351, 2011.

[104] M D Radin, C W Monroe, and D J Siegel. How Dopants Can Enhance Charge Transport in Li2O2. *Chem. Mater.*, 27:839–847, 2015.

[105] J S Hummelshøj, J Blomqvist, S Datta, T Vegge, J Rossmeisl, K S Thygesen, A C Luntz, K W Jacobsen, and J K Nørskov. No Title. *J. Chem. Phys.*, 132:71101–71104, 2010.

[106] Y.-C. Lu, B M Gallant, D G Kwabi, J R Harding, R R Mitchell, M S Whittingham, and Y Shao-Horn. Lithium-oxygen batteries: bridging mechanistic understanding and battery performance. *Energy Environ. Sci.*, 6:750–768, 2013.

[107] Sang-Eun Cheon, Ki-Seok Ko, Ji-Hoon Cho, Sun-Wook Kim, Eog-Yong Chin, and Hee-Tak Kim. Rechargeable Lithium Sulfur Battery. *J. Electrochem. Soc.*, 150(6):A800, 2003.

[108] Céline Barchasz, Jean-Claude Leprêtre, Fannie Alloin, and Sébastien Patoux. New insights into the limiting parameters of the Li/S rechargeable cell. *J. Power Sources*, 199:322–330, 2012.

[109] J Read. Characterization of the Lithium/Oxygen Organic Electrolyte Battery. *J. Electrochem. Soc.*, 149:A1190–A1195, 2002.

[110] Xinyong Tao, Jianguo Wang, Zhuogao Ying, Qiuxia Cai, Guangyuan Zheng, Yongping Gan, Hui Huang, Yang Xia, Chu Liang, Wenkui Zhang, and Yi Cui. Strong Sulfur Binding with Conducting MagneÌĄ li-Phase TinO2n-1 Nanomaterials for Improving Lithium-Sulfur Batteries. *Nano Lett.*, 14:5288–5294, 2014.

[111] Robert R. Mitchell, Betar M. Gallant, Carl V. Thompson, and Yang Shao-Horn. All-carbon-nanofiber electrodes for high-energy rechargeable LiâĂŞO2 batteries. *Energy Environ. Sci.*, 4(8):2952, 2011.

[112] K M Abraham and Z Jiang. A Polymer Electrolyte-Based Rechargeable Lithium/Oxygen Battery. *J. Electrochem. Soc.*, 143:1–5, 1996.

[113] J Xiao, D Mei, X Li, W Xu, D Wang, G L Graff, W D Bennett, Z Nie, L V Saraf, I A Aksay, J Liu, and J.-G. Zhang. Hierarchically Porous Graphene as a Lithium-Air Battery Electrode. *Nano Lett.*, 11:5071–5078, 2011.

[114] Y Wang and H Zhou. A lithium-air battery with a potential to continuously reduce O2 from air for delivering energy. *J. Power Sources*, 195:358–361, 2010.

[115] J L Wang, J Yang, J Y Xie, N X Xu, and Y Li. Sulfur-carbon nano-composite as cathode for rechargeable lithium battery based on gel electrolyte. *Electrochem. Commun.*, 4:499–502, 2002.

[116] H Chen, Q Zou, Z Liang, H Liu, Q Li, and Y.-C. Lu. Sulphur-impregnated flow cathode to enable high-energy-density lithium flow batteries. *Nat. Commun.*, 6:5877, 2015.

[117] K S Toohey, N R Sottos, J A Lewis, J S Moore, and S R White. Self-healing materials with microvascular networks. *Nat. Mater.*, 6:581–585, 2007.

[118] P D Frischmann, L C H Gerber, S E Doris, E Y Tsai, F Y Fan, X Qu, A Jain, K A Persson, Y.-M. Chiang, and B A Helms. No Title. *Chem. Mater.*, 27:6765–6770, 2015.

[119] Y Chen, S A Freunberger, Z Peng, O Fontaine, and P G Bruce. Charging a Li-O2 battery using a redox mediator. *Nat. Chem.*, 5:489–494, 2013.

[120] H.-D. Lim, H Song, J Kim, H Gwon, Y Bae, K.-Y. Park, J Hong, H Kim, T Kim, Y H Kim, X Lepró, R Ovalle-Robles, R H Baughman, and K Kang. No Title. *Angew. Chem., Int. Ed.*, 53:3926–3931, 2014.

[121] B J Bergner, A Schürmann, K Peppler, A Garsuch, and J Janek. TEMPO: A Mobile Catalyst for Rechargeable Li-O2 Batteries. *J. Am. Chem. Soc.*, 136:15054–15064, 2014.

[122] N Feng, P He, and H Zhou. Enabling Catalytic Oxidation of Li2O2 at the Liquid-Solid Interface: The Evolution of an Aprotic Li-O2 Battery. *ChemSusChem*, 8:600–602, 2015.

[123] M J Lacey, J T Frith, and J R Owen. A redox shuttle to facilitate oxygen reduction in the lithium air battery. *Electrochem. Commun.*, 26:74–76, 2013.

[124] D Sun, Y Shen, W Zhang, L Yu, Z Yi, W Yin, D Wang, Y Huang, J Wang, D Wang, and J B Goodenough. A Solution-Phase Bifunctional Catalyst for Lithium-Oxygen Batteries. *J. Am. Chem. Soc.*, 136:8941–8946, 2014.

[125] C Xia, R Black, R Fernandes, B Adams, and L F Nazar. The critical role of phase-transfer catalysis in aprotic sodium oxygen batteries. *Nat. Chem.*, 7:496–501, 2015.

[126] S S Zhang. Liquid electrolyte lithium/sulfur battery: Fundamental chemistry, problems, and solutions. *J. Power Sources*, 231:153–162, 2013.

[127] T A Pascal, K H Wujcik, J J Velasco-Velez, C Wu, A A Teran, M Kapilashrami, J Cabana, J Guo, M Salmeron, N Balsara, and D Prendergast. X-ray Absorption Spectra of Dissolved Polysulfides in Lithium-Sulfur Batteries from First-Principles. *J. Phys. Chem. Lett.*, 5:1547–1551, 2014.

[128] K H Wujcik, J Velasco-Velez, C H Wu, T A Pascal, A A Teran, M A Marcus, J Cabana, J Guo, D Prendergast, M Salmeron, and N P Balsara. Fingerprinting Lithium-Sulfur Battery Reaction Products by X-ray Absorption Spectroscopy. *J. Electrochem. Soc.*, 161:A1100–A1106, 2014.

[129] S Meini, R Elazari, A Rosenman, A Garsuch, and D Aurbach. The Use of Redox Mediators for Enhancing Utilization of Li2S Cathodes for Advanced Li-S Battery Systems. *J. Phys. Chem. Lett.*, 5:915–918, 2014.

[130] A J Bard and L R Faulkner. *Electrochemical Methods Fundamentals and Applications.* 2001.

[131] H Kojima and A J Bard. Determination of rate constants for the electroreduction of aromatic compounds and their correlation with homogeneous electron transfer rates. *J. Am. Chem. Soc.*, 97:6317–6324, 1975.

[132] R S Ruoff, K M Kadish, P Boulas, and E C M Chen. The Relationship between the Electron Affinities and Half-Wave Reduction Potentials of Fullerenes, Aromatic Hydrocarbons, and Metal Complexes. *J. Phys. Chem.*, 99:8843–8850, 1995.

[133] Z Chen, A Lohr, C R Saha-Möller, and F Würthner. Self-assembled pi-stacks of functional dyes in solution: structural and thermodynamic features. *Chem. Soc. Rev.*, 38:564, 2009.

[134] T F A De Greef, M M J Smulders, M Wolffs, A P H J Schenning, R P Sijbesma, and E W Meijer. Supramolecular Polymerization. *Chem. Rev.*, 109:5687, 2009.

[135] M. Jafarian, M.G. Mahjani, F. Gobal, and I. Danaee. Effect of potential on the early stage of nucleation and growth during aluminum electrocrystallization from molten salt (AlCl3–NaCl–KCl). *J. Electroanal. Chem.*, 588(2):190–196, 2006.

[136] Sheng Zhang. Improved Cyclability of Liquid Electrolyte Lithium/Sulfur Batteries by Optimizing Electrolyte/Sulfur Ratio. *Energies*, 5(12):5190–5197, 2012.

[137] Seon-Soon Kim, Se-Young Choi, Chan-Gyung Park, and Hyeon-Woo Jin. Transparent conductive ITO thin films through the sol-gel process using metal salts. *Thin Solid Films*, 347(1-2):155–160, 1999.

[138] Mingsong Wang, Ka Eun Lee, Sung Hong Hahn, Eui Jung Kim, Sunwook Kim, Jin Suk Chung, Eun Woo Shin, and Chinho Park. Optical and photoluminescent properties of sol-gel Al-doped ZnO thin films. *Mater. Lett.*, 61(4-5):1118–1121, 2007.

[139] W. Tang and D. C. Cameron. Aluminum-doped zinc oxide transparent conductors deposited by the sol-gel process. *Thin Solid Films*, 238(1):83–87, 1994.

[140] Ran Elazari, Gregory Salitra, Yossi Talyosef, Judith Grinblat, Charislea Scordilis-Kelley, Ang Xiao, John Affinito, and Doron Aurbach. Morphological and Structural Studies of Composite Sulfur Electrodes upon Cycling by HRTEM, AFM and Raman Spectroscopy. *J. Electrochem. Soc.*, 157(10):A1131, 2010.

[141] Bin Wang, Saeed M Alhassan, and Sokrates T Pantelides. Formation of Large Polysulfide Complexes during the Lithium-Sulfur Battery Discharge. *Phys. Rev. Appl.*, 2(3):34004, sep 2014.